

# Cell Sorting in Deterministic Lateral Displacement Devices

Inaugural-Dissertation

zur  
Erlangung des Doktorgrades  
der Mathematisch-Naturwissenschaftlichen Fakultät  
der Universität zu Köln  
vorgelegt von

Ewan Henry  
aus London, Großbritannien

Jülich  
2017





# Cell Sorting in Deterministic Lateral Displacement Devices

Inaugural-Dissertation

zur  
Erlangung des Doktorgrades  
der Mathematisch-Naturwissenschaftlichen Fakultät  
der Universität zu Köln  
vorgelegt von

Ewan Henry  
aus London, Großbritannien

Jülich  
2017

Berichtersteller:  
(Gutachter)

**Prof. Dr. Gerhard Gompper**

**Prof. Dr. Matthias Sperl**

Tag der letzten mündlichen Prüfung: 09.05.2017

## ABSTRACT

---

The ability to sort cells is extremely desirable in many fields such as diagnostics, chemical processing, and biological analyses. Label-free sorting schemes in microfluidic devices represent a promising alternative to the fluorescence and immunomagnetic activated cell sorting methods which are current industry standards; permitting reduced costs, simpler operation, and increased portability. Furthermore, passive label-free sorting schemes such as deterministic lateral displacement (DLD) devices pose further advantages; for instance, sorting cells in accordance with their physical properties with no need for the application of external fields, magnetic beads, or fluorescent labels. Many of the cells and particles which require sorting are non-spherical and deformable, however the majority of theory for predicting particle behaviour in Deterministic Lateral Displacement (DLD) devices is only applicable to the limited case of rigid spheres in circular post arrays. The concept behind the separation mechanism for rigid spheres relies upon the assumption that DLD device geometry uniquely determines the fluid flow field, which subsequently defines a critical particle size and the lateral separation of particles of different sizes. Whilst the developed theories are exceedingly successful for designing devices for separating rigid beads, they are restricted to sorting particles by size, a characteristic which is ill-defined for non-spherical deformable particles in flow. Furthermore, this design approach squanders the full potential of DLD, which could utilise alternative particle characteristics such as elasticity and dynamic behaviour as the bases for separation of non-spherical deformable particles.

This work uses a combination of mesoscale hydrodynamic simulations and microfluidics experiments to demonstrate how cells' mechanical and dynamic properties can be used as separation criteria within different DLD device geometries. Two mesoscopic particle-based methods are employed in simulations to represent fluid; the dissipative particle dynamic (DPD) technique and the smoothed dissipative particle dynamic method (SDPD). Additionally, two-dimensional(2D) mesoscopic models of rigid beads and red blood cells (RBC) are employed to investigate particle motion in DLD devices in a qualitative manner, and a three-dimensional (3D) model of Red Blood Cell (RBC)s is used to obtain a more precise quantitative picture. RBCs are chosen because they represent a ubiquitous non-spherical deformable particle, and sorting based on their mechanical properties in DLD devices would aid in diagnosis of lethal diseases such as malaria.

The 2D simulation results show that a critical particle size can be well defined for rigid spherical particles in circular post arrays depending on the inter-post spacing, the row-shift fraction, and the corresponding flow field; in quantitative agreement with current empirical findings and theory. Additional 2D simulations allow the empirical

equation for the critical size of rigid spherical particles in circular post arrays to be generalized and extended for diamond, square and triangular post arrays. In contrast, 2D simulation results demonstrate that RBCs exhibit far more complex dynamics within DLD post arrays than rigid spheres, and the particle motion cannot be predicted by a single parameter such as the critical size. Instead, the dynamic behaviour and deformation of the RBC are found to strongly influence transit behaviour through DLD devices, providing the potential for novel sorting schemes. The 2D work motivates the further study of RBC behaviour in DLD devices using 3D simulations and supplementary experiments to gain a more quantitative understanding of the underlying physical mechanisms at play. 3D simulations and microfluidic experiments achieve excellent quantitative agreement and reveal that RBCs can travel in transit modes which are inaccessible to rigid spheres due to the complex interplay between hydrodynamic interactions with posts, RBC deformations, and RBC dynamic behaviour. The dynamic behaviour of RBCs is investigated by confining cells within flow channels of different heights and by altering the ratio between the intra-cellular fluid and the suspending medium. Thin devices inhibit the dynamic behaviour of RBCs, resulting in trajectories which are more like those of rigid spheres, however deformation still plays a key distinctive role. Thick devices which allow full re-orientation of RBCs and different dynamic behaviours are observed at different viscosity contrasts: At physiological viscosity contrasts RBCs are found to move in a tumbling motion and, under conditions where the intra- and extra-cellular fluid are equal, RBCs are found to favour tank-treading behaviour. Each of these distinct dynamic behaviours result in dramatically different RBC trajectories through DLD post arrays, demonstrating how non-spherical deformable particles can be sorted according to characteristics other than size, such as membrane shear modulus, membrane bending rigidity, or internal viscosity. Finally, 3D simulations are used to demonstrate a potential DLD device design for deformability-based sorting of RBCs; achieving good lateral separation between healthy RBCs and RBCs with pathological values for their shear modulus.

## ZUSAMMENFASSUNG

---

Zellen nach ihren Eigenschaften zu sortieren ist in vielen Bereichen wie Diagnostik oder chemischen und biologischen Analysen von großem Interesse. Die Trennung in mikrofluidischen Apparaturen, für die keine Marker benötigt werden, stellt durch geringere Kosten, einfache Bedienung und erleichtertem Transport eine vielversprechende Alternative zu gegenwärtigen Industriestandards, wie die Trennung durch fluoreszenz- oder immunomagnetisch markierter Partikel, dar. Ein weiterer Vorteil von Apparaturen, die ohne Marker auskommen, z.B. deterministic lateral displacement (DLD), ist die Sortierung der Moleküle ausschließlich aufgrund ihrer physikalischen Eigenschaften, ohne die Notwendigkeit von externen Feldern oder Magnetpartikeln. Viele Zelltypen und Moleküle bei denen das Trennen nach physikalischen Eigenschaften von Interesse ist, sind nicht kugelförmig und verformbar. Jedoch sind bestehende Theorien in erster Linie ausschließlich auf Strömungsverhalten starrer Kugeln in Rundsäulen-Arrays in DLD Apparaturen anwendbar. Dem Prinzip der Trennung von starren Kugeln liegt die Annahme zugrunde, dass das Strömungsfeld der Flüssigkeit hauptsächlich durch die Geometrie der Apparatur bestimmt wird, wodurch eine kritische Partikelgröße definiert wird, die zur räumlichen Aufspaltung von Objekten verschiedener Größe führt. Die bereits bestehenden Theorien eignen sich hervorragend für den Entwurf von Apparaturen zur Trennung von starren Kugeln, jedoch sind sie auf die Trennung nach Teilchengröße beschränkt. Da sich hingegen die Partikelgröße für nicht-kugelförmige, verformbare Objekte in einer Strömung nicht klar definieren lässt, sind diese Theorien nur beschränkt auf solche Partikel anwendbar.

Im Rahmen dieses Projektes wird eine Kombination von mesoskopischen, teilchenbasierten Simulationsmethoden und mikrofluidischen Experimenten verwendet, um nachzuweisen, wie mechanische (Viskositätskontrast, Schubmodul, Membranbiegesteifigkeit) und dynamische Eigenschaften von Zellen als Trennungskriterien in DLD Apparaturen genutzt werden können. Um die Flüssigkeit zu simulieren werden zwei mesoskopische, teilchenbasierte Methoden angewendet: die dissipative particle dynamics (DPD) und die smoothed dissipative particle dynamics (SDPD) Methode. Zusätzlich werden zweidimensionale (2D), mesoskopische Modelle von starren Kugeln und roten Blutkörperchen (red blood cells – RBCs) verwendet, um Teilchenbewegung in DLD Apparaturen in einer qualitativen Weise zu erforschen und ein dreidimensionales (3D) Modell von RBCs um eine genauere quantitative Darstellung zu erhalten. RBCs werden als Modell verwendet, da sie allgegenwärtige nicht-kugelförmige, verformbare Objekte darstellen. Des Weiteren kann die Trennung von RBCs aufgrund ihrer mechanischen Eigenschaften in DLD Apparaturen die Diagnose von tödlichen Blutkrankheiten wie Malaria unterstützen. Die Ergebnisse der 2D Simulationen zeigen, dass sich die kri-

tische Partikelgröße für starre, kugelförmige Partikel im Rundsäulen-Array abhängig von dem Abstand der Säulen, der Fraktion der Zeilenverschiebung und dem korrespondierenden Strömungsfeld, gut bestimmen lässt. Dies steht im Einklang mit Theorie und empirischen Erkenntnissen. Zusätzliche 2D Simulationen verschiedener Säulen-Array Geometrien ermöglichen die Erweiterung der empirischen Gleichung für die kritische Größe starrer kugelförmiger Partikel auf Rauten-, Viereck- und Dreieck-Säulen Arrays. Dagegen zeigen 2D Simulationen, dass RBCs eine weitaus komplexere Dynamik in DLD Arrays vorweisen als starre Kugeln, da die Teilchenbewegung nicht von einem einzelnen Parameter wie der kritischen Größe abhängig gemacht werden kann. Stattdessen kann beobachtet werden, dass dynamisches Verhalten und Verformung der RBCs den Durchfluss durch die DLD Apparatur stark beeinflussen, was die Entwicklung neuer Sortiersysteme ermöglicht. Die Ergebnisse der 2D Simulationen verdeutlichen die Wichtigkeit weiterer Untersuchungen vom Strömungsverhalten von RBC in DLD Apparaturen mittels 3D Simulationen und ergänzenden Experimenten, damit ein besseres quantitatives Verständnis der zugrundeliegenden physikalischen Mechanismen aufgebaut werden kann. 3D Simulationen und mikrofluidische Experimente zeigen, dass die Trajektorien durch einen Rundsäulen-Array von RBCs deutlich von denen von starren Kugeln abweichen können. Dies ist durch das komplexe Zusammenspiel von hydrodynamischen Wechselwirkungen mit den Säulen, der Verformung der RBCs und dem dynamischem Verhalten bedingt. Dabei wird das dynamische Verhalten der RBCs für verschiedene Höhen der Durchflusskanäle und verschiedene Verhältnisse der Viskosität von intra- und extrazellulärer Flüssigkeit (Medium) untersucht. Flache Apparaturen hemmen das dynamische Verhalten der RBCs, was zu Trajektorien führt, die der starrer Kugeln ähneln, jedoch beeinflusst von der RBC Deformierung. Höhere Apparaturen erlauben eine Neuausrichtung der RBCs in allen Raumdimensionen. Dabei wurde unterschiedliches dynamisches Verhalten bei verschiedenen Viskositätsverhältnissen beobachtet: bei physiologischem Viskositätskontrast wird eine taumelnde Bewegung der RBCs beobachtet. Ist die Viskosität der intra- und interzellulären Flüssigkeit gleich, wird vermehrt das Tank-treading-Verhalten beobachtet. Zusammenfassend führen alle Szenarien zu extrem unterschiedlichem Durchflussverhalten der RBCs in DLD Säulen-Arrays, was zeigt, dass nicht-kugelförmige, verformbare Partikel nach anderen Eigenschaften als der Größe, wie Viskositätskontrast, Schermodul oder Biegesteifigkeit, sortiert werden können. Abschließend wurden 3D Simulationen eines möglichen Aufbaus einer DLD Apparatur, durch welchen RBCs anhand ihrer Verformbarkeit sortiert werden könnten, durchgeführt. Die Ergebnisse weisen auf eine ausgeprägte räumliche Aufspaltung von gesunden RBCs und RBCs mit pathologischen Werten für deren Schubmodul auf.

## ACKNOWLEDGMENTS

---

Firstly, I would like to thank Prof. Gerhard Gommper for giving me the opportunity to study in Juelich FZJ in the first place and for always finding time for valuable discussions amidst his unfathomably busy schedule.

I am also exceedingly grateful to Dr. Dmitry Fedosov, who has taught me so much about simulation techniques and their application to flow in microfluidics. Thank you, Dmitry, for your continued support and patience throughout the course of my PhD.

I have had the privilege of working with many wonderful people during this PhD. I would like to thank my colleague, Zunmin, with whom I worked closely throughout the course of this thesis and shared many insightful discussions. The experimental works which supplemented this work would not have been possible if it was not for the help of three brilliant experimentalists at Lund University; thank you Jonas, Jason and Stefan for your invaluable experimental collaboration, I look back fondly on the weeks I spent in Lund learning about microfluidics in your labs.

I would also like to thank the staff and my fellow students at ICS-2 in Jülich FZJ, who make the institute such a pleasant environment to work in and collectively donate a never-ending supply of confectionery from all corners of the globe to the institute's humble kitchen tables. I am also fortunate to have been part of the LAPASO project, and I would like to thank the LAPASO fellows who were such fun to work with and who provided me with a broader picture of why DLD devices are so important in diagnostics.

Last of all, there remain a few people for whom thanks is simply not enough. Mum and Dad, working on this thesis has been a formative experience to say the least, but I am certain I would have never have finished or potentially even begun if you had not raised me with such love and support. Craig, you are my favourite brother, and the countless enjoyable hours we spent on skype together during the evenings over the past three years gave me an anchorage to home, and for that I am incredibly grateful. Last but not least, Alessandra, of all things that have happened to me over the course of this PhD, meeting you and getting to know you is the one I treasure most. Thank you for the good times and your tireless support - I promise this is my last thesis.





## CONTENTS

---

1	INTRODUCTION	1
1.1	Motivation . . . . .	1
1.2	Biological and Medical Basis . . . . .	3
1.2.1	Blood Cells . . . . .	3
1.2.2	Diagnosis from Blood . . . . .	5
1.2.3	Malaria . . . . .	6
1.3	Microfluidic Particle Sorting . . . . .	10
1.3.1	Fluorescent Label-Based Sorting . . . . .	10
1.3.2	Active Label-Based Sorting . . . . .	12
1.3.3	Bead-Based Sorting . . . . .	13
1.3.4	Active Label-Free Sorting . . . . .	14
1.3.5	Passive Label-Free Sorting . . . . .	15
1.4	Physical and Numerical Basis . . . . .	16
1.4.1	Hydrodynamics . . . . .	16
1.4.2	Soft Matter . . . . .	18
1.4.3	Simulations . . . . .	18
1.5	Red Blood Cells in Flow . . . . .	20
1.5.1	RBC Shape and Dynamics . . . . .	21
1.5.2	Collective RBC Behaviour . . . . .	21
1.6	Thesis Structure . . . . .	23
2	NUMERIC TECHNIQUES	25
2.1	Fluid Models . . . . .	25
2.1.1	Dissipative Particle Dynamics . . . . .	25
2.1.2	Smoothed Particle Hydrodynamics . . . . .	27
2.1.3	Smoothed Dissipative Particle Dynamics . . . . .	28
2.1.4	Numerical Integration and Boundary Conditions . . . . .	30
2.2	Cell Models . . . . .	31
2.2.1	2D Rigid Bead and Red Blood Cell . . . . .	31
2.2.2	3D Red Blood Cell . . . . .	33
2.2.3	Cell-Fluid Coupling . . . . .	34
3	EXPERIMENTAL TECHNIQUES	37
3.1	Deterministic Lateral Displacement . . . . .	37
3.1.1	Flow in Row-Shifted Arrays . . . . .	37
3.1.2	Sorting by Size . . . . .	41
3.1.3	Non-spherical Deformable Particles . . . . .	42
3.2	Experimental Procedure . . . . .	47

3.2.1	Device Design . . . . .	47
3.2.2	Device Fabrication . . . . .	49
3.2.3	Data Collection and Analysis . . . . .	50
4	SORTING RIGID AND DEFORMABLE PARTICLES IN DLD: A 2D SIMULATION APPROACH	55
4.1	Introduction . . . . .	55
4.2	Simulation Setup . . . . .	56
4.3	Results . . . . .	57
4.3.1	Rigid Spheres in DLD Obstacle Arrays . . . . .	58
4.3.2	Red Blood Cells . . . . .	65
4.4	Summary . . . . .	70
5	UNDERSTANDING RBC DYNAMICS IN DLD: A 3D SIMULATION APPROACH	73
5.1	Introduction . . . . .	73
5.2	Simulation Setup . . . . .	74
5.3	Experimental Setup . . . . .	75
5.4	Results . . . . .	77
5.5	Summary . . . . .	89
6	DEFORMABILITY BASED RBC SORTING	93
6.1	Introduction . . . . .	93
6.2	Simulation Setup . . . . .	94
6.3	Results . . . . .	96
6.4	Summary . . . . .	107
7	CONCLUSION AND OUTLOOK	109
	Appendix	119
A	SIMULATION DETAILS	121
B	EXPERIMENTAL DETAIL	123
	BIBLIOGRAPHY	131

## LIST OF FIGURES

---

Figure 1.1	SEM image of blood . . . . .	4
Figure 1.2	Life Cycle of Malaria Parasite . . . . .	7
Figure 1.3	<i>P. Falciparum</i> Infected RBCs . . . . .	9
Figure 1.4	Cell Sorting Techniques. . . . .	11
Figure 1.5	Clustering and Alignment of RBCs. . . . .	22
Figure 2.1	DPD Coarse-Graining . . . . .	27
Figure 2.2	2D Bead-Spring Models . . . . .	32
Figure 2.3	3D RBC Network Model. . . . .	33
Figure 3.1	DLD Geometry. . . . .	38
Figure 3.2	Flow in Pillar Arrays . . . . .	39
Figure 3.3	Critical Radius - Theory vs. Observation . . . . .	42
Figure 3.4	Shape and Deformability Sorting . . . . .	44
Figure 3.5	Separation vs. Concentrating. . . . .	48
Figure 3.6	Chirped DLD Device. . . . .	49
Figure 3.7	Trajectory Extraction. . . . .	52
Figure 3.8	Hausdorff Distance. . . . .	54
Figure 3.9	Alignment via Hausdorff Distance . . . . .	54
Figure 4.1	Simulation Domain. . . . .	57
Figure 4.2	Rigid Spheres in Circular Post Arrays . . . . .	59
Figure 4.3	Rigid Bead Mode Diagram. . . . .	60
Figure 4.4	Post Shapes and Flow Profiles . . . . .	61
Figure 4.5	Rigid Spheres in Diamond Post Arrays . . . . .	62
Figure 4.6	Rigid Spheres in Square Post Arrays . . . . .	63
Figure 4.7	Rigid Spheres in Triangle Post Arrays . . . . .	64
Figure 4.8	Red Blood Cell Separation Index . . . . .	65
Figure 4.10	Red Blood Cell Asphericity. . . . .	67
Figure 4.9	RBC Dynamics for Post Shapes. . . . .	69
Figure 5.1	RBC Transit Modes in 3D. . . . .	74
Figure 5.2	Simulated 3D RBC in Post Array. . . . .	75
Figure 5.3	Chirped DLD Device Schematic . . . . .	76
Figure 5.4	Experimental and Simulated RBCs for $C = 5$ . . . . .	78
Figure 5.5	Aligned Experimental Trajectories of RBCs in DLD . . . . .	80
Figure 5.6	Lateral Displacement per Post in the Thick Device . . . . .	81
Figure 5.7	Lateral Displacement per Post in the Thin Device . . . . .	84
Figure 5.8	DLD Sensitivity to RBC Size . . . . .	85
Figure 5.9	Acceptance Rates of RBCs in Thin/Thick DLD Devices. . . . .	86

Figure 5.10	Viscosity Dependence of RBC Dynamics in DLD . . . . .	88
Figure 6.1	Triangular Post Details. . . . .	95
Figure 6.2	RBCs in Triangular Post Array with Pathological $k_b$ . . . . .	98
Figure 6.3	Bending Rigidity Dependence of RBC Asphericity . . . . .	98
Figure 6.4	RBC Shapes for Different $k_b$ . . . . .	99
Figure 6.5	RBCs in Triangular Post Array with Pathological $\mu_0$ . . . . .	101
Figure 6.6	Shear Modulus Dependence of RBC Asphericity . . . . .	102
Figure 6.7	RBC Shapes for Different $\mu_0$ . . . . .	102
Figure 6.8	RBCs with Pathological $\mu_0$ Separated via Dynamic Behaviour . .	104
Figure 6.9	Shear Modulus and Dynamic Behaviour Dependence of RBC Asphericity . . . . .	105
Figure 6.10	Shapes of RBCs with Different Dynamic Behaviours for Patho- logical $\mu_0$ . . . . .	106
Figure B.1	Experimental Device Schematic . . . . .	125
Figure B.2	Buffer Viscosity vs. Dextran Concentration . . . . .	126
Figure B.3	Blocked RBC Trajectory . . . . .	130

## LIST OF TABLES

Table 5.1	Trajectory Acceptance in Thick Device at $C = 5$ . . . . .	82
Table A.1	2D Particle Model Parameters. . . . .	121
Table A.2	2D DPD Fluid Parameters. . . . .	121
Table A.3	3D SDPD Fluid Parameters. . . . .	122
Table A.4	3D RBC Model Parameters. . . . .	122
Table B.1	DLD Array Row Shifts. . . . .	124
Table B.2	Traj. Acceptance in Thick Device at $C = 1$ . . . . .	128
Table B.3	Traj. Acceptance in Thick Device at $C = 0.25$ . . . . .	128
Table B.4	Traj. Acceptance in Thin Device at $C = 5$ . . . . .	129
Table B.5	Traj. Acceptance in Thin Device at $C = 2$ . . . . .	129

## ACRONYMS

DLD Deterministic Lateral Displacement

DPD Dissipative Particle Dynamics

SDPD Smoothed Dissipative Particle Dynamics

RBC Red Blood Cell

2D Two Dimensional

3D Three Dimensional

FACS Fluorescence Activated Cell Sorting

MACS Magnetic Activated Cell Sorting

DNA Deoxyribonucleic Acid

WBC White Blood Cell

WHO World Health Organization

DEP Dielectricphoresis

SAW Surface Acoustic Waves

SSAW Standing Surface Acoustic Waves

MAP Magnetophoresis

CTC Circulating Tumour Cell

NSE Navier-Stokes Equation

MD Molecular Dynamics

BD Brownian Dynamics

TF Thermal Fluctuations

HI Hydrodynamic Interactions

LB Lattice Boltzmann

MPC Multiple Particle Collision

SPH Smoothed Particle Hydrodynamics

TT Tank-Treading

TB Tumbling

PDMS Polydimethylsiloxane

## USED SYMBOLS

---

$k_B$	Boltzmann constant
$T$	Temperature
$m$	Mass
$I$	Moment of inertia
$\omega$	Rotational velocity
$\mathbf{u}$	Velocity vector
$\mathbf{r}$	Position vector
$\rho$	Density
$n$	Number density
$\eta$	Dynamic viscosity
$p$	Pressure
$\mathbf{f}, \mathbf{F}$	Force
$Re$	Reynolds number
$U$	Characteristic velocity
$L$	Characteristic length
$\alpha$	Conservative force coefficient
$\omega_D$	Dissipative weight function
$\gamma$	Dissipative (Friction) force coefficient
$k$	Weight function coefficient
$\omega^R$	Random weight function
$\xi$	Random force component
$\sigma$	Random force coefficient
$W$	SPH kernel function
$W_L$	Lucy function
$r_c$	Cut-off radius
$N_p, N_v$	Number of particles
$N_s$	Number of springs
$l$	Spring length
$l_m$	Spring extension limit
$k_p$	Spring constant
$l_p$	Persistence length
$l_0$	Equilibrium spring length
$Y$	Youngs modulus
$k_b$	Bending constant
$k_a$	Global area constraint coefficient
$k_d$	Local area constraint coefficient

$A$	Area
$A_0$	Equilibrium area
$L_0$	Contour length
$D$	Diameter
$U_{\text{bend}}$	Bending potential energy
$U_{\text{spring}}$	Spring potential energy
$U_{\text{area}}$	Area conservation potential energy
$U_{\text{vol}}$	Volume conservation potential energy
$k_v$	Volume constraint coefficient
$K$	Area compression modulus
$\mu_0$	Shear modulus
$g(r)$	Radial distribution function
$\lambda$	DLD post spacing
$\Delta\lambda$	Row shift
$\epsilon$	Row shift fraction
$N$	DLD array period
$\phi$	Fluid flux
$G$	Inter-postal gap
$G_V$	Vertical inter post gap
$G_H$	Horizontal inter-post gap
$R$	Radius
$R_c$	Critical radius
$D_c$	Critical particle size
$d$	Post diameter
$P_e$	Péclet number
$D_{\text{iff}}$	Diffusion coefficient
$d_H$	Hausdorff distance
$\kappa$	Macroscopic bending rigidity
$\tau$	Characteristic relaxation time
$D_{\text{sph}}$	Rigid bead diameter
$I_s$	Separation index
$\alpha, \beta$	Critical radius fitting parameters
$D_{\text{eff}}$	Effective particle size
$\delta$	Asphericity
$C$	Viscosity contrast
$\eta_i$	Internal viscosity
$\eta_o$	External viscosity
$l$	Average lateral displacement per post
$f$	Lane-swapping frequency
$m$	Posts per lane-swapping event





## INTRODUCTION

---

### 1.1 MOTIVATION

The ability to sort and separate microscopic particles is highly coveted in many technical fields. In diagnostics, the gold standard for diagnosis of diseases such as malaria requires direct observation using microscopy. However, this often poses difficulty as the ratio of infected-to-uninfected red blood cells in patient samples can be as low as 1 : 1000000 [1]. Consequently, mechanisms for increasing the concentration of rare pathogens in patient samples can dramatically improve the effectiveness of microscopy diagnosis.

Far removed from diagnostics, in commercial industries, sorting techniques are being used to identify organisms of monetary value. For example, the energy sector have begun to fund research which employs particle sorting to identify high-lipid-content organisms as candidates for bio-fuel production, providing a potential future alternative to fossil fuels. [2]

There are many different methods of particle sorting and each falls into one of two categories: labelled and label-free sorting. The two prominent label sorting techniques are fluorescence and immunomagnetic activated cell sorting (FACS and MACS) [3, 4], which require the particles in a sample to selectively bind to fluorescent or magnetic labels respectively. In MACS, labelled populations are separated by exposing the sample to a magnetic field, and in FACS the labelled populations are sorted by individually analysing their fluorescent response to different frequency lasers and storing them accordingly. In order to selectively label particles it is necessary to know the cell surface molecules present in the sample, as these are the sites to which labels bind.

Label-free sorting techniques require no such labelling process, instead they rely on the intrinsic properties of particles as a means for sorting. As such, characteristics like shape, size, density, rigidity and permittivity can be exploited to separate heterogeneous populations of particles. The most obvious and perhaps oldest example of label-free sorting is centrifugation, where the application of a centrifugal force to a sample causes particles of different density and size to sediment at different speeds [5].

The aforementioned sorting techniques represent the industry standards and have multiple limitations, including: The requirement for large sample volumes, high equipment costs, slow sorting rates, and the necessity for expertise in operating and maintaining complex machinery. To address these issues for the next generation of cell sorting devices, researchers are looking to microfluidic technologies. Microfluidic devices

provide cheaper, simpler, and more portable platforms for the handling and manipulation of cells. Furthermore, multiple microfluidic devices with a variety of functionality can be utilised on a single integrated platform to perform a series of procedures on cells, providing a lab-on-a-chip style device.

The spatial sorting of cells within a microdevice can be achieved by fabricating micropatterns inside flow channels. Patterns may consist of ridges, posts, or ratchets, and as cells traverse a patterned microchannel their trajectories are altered by interactions with the obstacles. Deterministic lateral displacement (DLD), pioneered by Huang *et al.* [6], is an important example of this technique. Cells in a DLD device migrate through an array of micro-pillars and are sorted according to their size. Sorting is predominantly governed by the geometry of the pillar array. The manner in which rigid spherical particles traverse DLD devices is well understood and devices can be designed to sort specific sized beads according to empirical formula [7]. In cases where the sorted particles have anisotropic profiles (e.g. rods and discocytes) or are highly deformable (e.g. RBCs and DNA) the sorting is dependant on the flow properties as well as the mechanical properties of the cell. Current DLD devices for sorting anisotropic, deformable particles use the theory for hard beads as guidelines and have been seen good success [8–10]. Often the device design aims to control the orientation of the particle in such a way that it's behaviour can be approximated to that of a sphere. For instance, RBCs in deep or shallow devices will orient differently, altering their effective size in the device [8]. However, it is not clear if these devices achieve optimal performance and, if better understood, the mechanisms which cause particles to deviate from the trajectories predicted for hard spheres may be utilized to improve sorting.

Understanding the rich interplay between particle deformation, particle orientation, device geometry and flow properties is a daunting task. Experimental investigation is highly impractical for a multitude of reasons. Firstly, identifying the optimal device geometry and flow profile for sorting one specific type of particle could require many devices to be fabricated and each would need to be tested under multiple flow conditions. Secondly, in order to gain any understanding of the mechanisms responsible for changes in sorting behaviour, a vast amount of video analysis would be necessary. Furthermore, video analysis provides a means of observing and categorising dynamic behaviour at best, and extracting mechanical stresses exerted on a cell via a 2D image analysis is non-trivial, requiring fitting with detailed theoretical models specific to the cell.

Simulation techniques provide a valuable alternative resource for understanding the complex behaviour of particles in DLD. The ability to test different device geometries without the need for fabricating new microdevices means a large number of configurations can be tested in considerably less time. Furthermore, variables can be precisely altered, meaning that changes in transit behaviour can be attributed to specific mechanical properties of particles such as shear modulus or internal viscosity. In addition to enhancing understanding, simulations can be used to design devices for separat-

ing specific types of particles or in optimising current devices. However, in order to demonstrate the potential of simulation motivated device design to experimentalists, it is first necessary to provide proof that simulations give sufficiently accurate results. Consequently it is important to realise quantitative agreement between simulations and existing experiments before serious suggestions can be made towards novel device designs or optimisations.

Experiments on polystyrene beads and RBCs in DLD devices will provide two initial benchmarks for demonstrating the relevance of simulations for DLD device development. Rigid beads are selected as an initial target as there are well established empiric rules for predicting their trajectories through DLD devices, allowing easy comparison with simulation results[7]. Comparison with RBCs is selected as a second benchmark as they represent a deformable anisotropic particle which is highly relevant in diagnostic and medical applications. Only after suitable agreement with experimentally observed RBC behaviour in DLDs is achieved will instigations begin on new sorting schemes for enhanced separation of healthy cells and unhealthy cells with altered physical properties.

## 1.2 BIOLOGICAL AND MEDICAL BASIS

Sorting cells within blood samples via DLD is the primary topic of this work. Consequently, it is helpful to give a introductory back ground on the main components of blood, with a particular focus on RBCs. Following this, malaria is taken as a case study of disease which alters the mechanical properties of RBCs; highlighting a specific medical application for sorting deformable non-spherical cells.

### 1.2.1 *Blood Cells*

Blood plays a vital role in the function of the human body, responsible for many fundamental tasks such as; supplying oxygen to tissue; transportation of nutrients, waste and hormones; regulating body temperature and Ph; and providing a basis for immunological response. In order to meet all of these requirements, blood has multiple components with varied functionality, all of which must persistently circulate the human body via an intricate network of blood vessels [11].

The majority component of blood is plasma, contributing to 54% of it's volume. Plasma is made up of 92% water and 8% serum proteins [11]. The water component acts as a solvent in which excretory matter dissolves for subsequent relocation and extraction at a relevant organ. For instance, in the case of extracting waste nitrogen, the urea dissolved in plasma carries nitrogen to the kidneys where it is removed for excretion in urine[12]. Furthermore, plasma serves as the suspending medium for transporting the remaining 45% of blood's make-up. The remaining volume fraction of blood

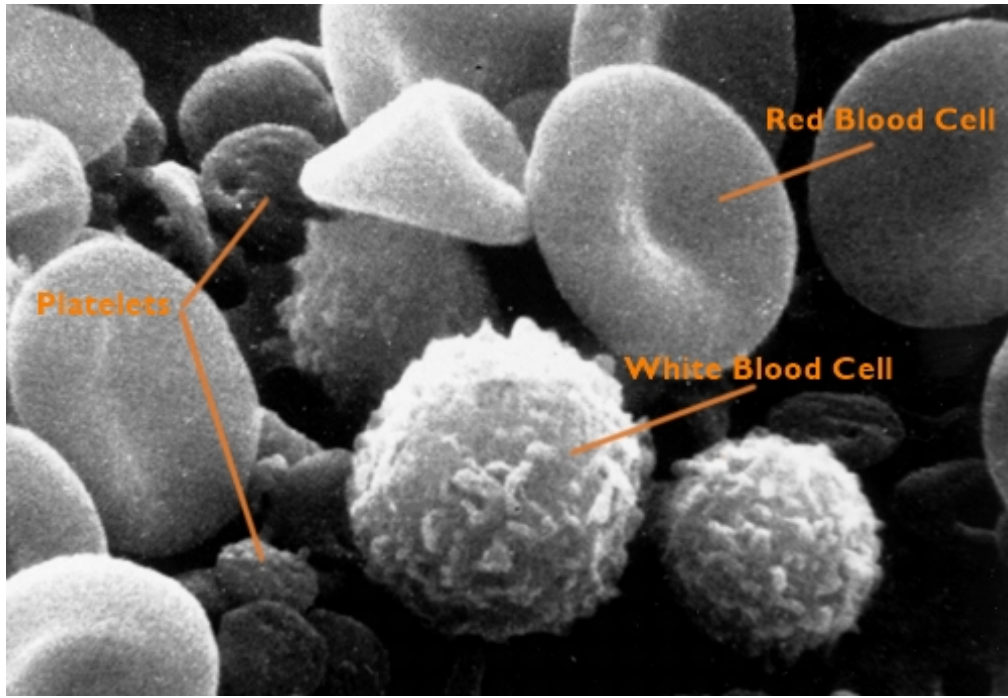


Figure 1.1: An image of whole blood captured using scanning electron microscopy. Labelled from left to right: two disc shaped platelets, a white blood cell and a red blood cell. Sourced from the [National Cancer Institute](#)

is composed of approximately 45% RBCs, 1% white blood cells (WBCs), and  $< 1\%$  platelets, with roughly  $5 \times 10^6$  RBCs,  $8 \times 10^3$  WBCs and  $350 \times 10^3$  platelets per  $1\mu\text{l}$  of blood[13]. All of these cells belong to the hematocyte family and can be seen in figure 1.1. Hematocytes start life as hematopoietic stem cells, multipotent cells located in the bone marrow. WBCs are the cells of the body's immune system, responsible for defending the body against infectious disease and foreign materials. They are roughly spherical in shape and have a diameter between  $D_{\text{WBC}} = 6 - 20\mu\text{m}$  depending on their type [14]. Platelets are much smaller disc-shaped cells, with a diameter between  $2 - 3\mu\text{m}$  and without a nucleus [15]. Their main function is to stop bleeding from damaged blood vessels, a process called hemostasis. Hemostasis is achieved by aggregation of platelets at the location around the damaged endothelium. Once large enough, the aggregate acts as a plug, blocking the puncture and initiating the repair process [11].

The most abundant type of hematocytes are RBCs. RBCs are chiefly responsible for transporting oxygen to tissue across the body; providing the fuel for aerobic respiration which is vital to cells' basic metabolic function. As RBCs travel through thinly walled capillaries surrounding the lung, oxygen is absorbed into the RBC's haemoglobin rich cytoplasm. Haemoglobin is a protein which can temporarily bind to oxygen molecules and, due to its iron content, gives blood its red colour. In addition to the transportation of oxygen, RBCs also remove roughly 20% of the waste carbon dioxide which is produced in aerobic respiration [16]. The waste carbon dioxide is expelled from the hu-

man body when the oxygen depleted red blood cells recirculate to the lungs, allowing them to return to an oxygenated state.

The morphology and mechanical characteristics of RBCs are vital to their success in delivering oxygen throughout the body. An average healthy human RBC has a width of  $D_{\text{RBC}} = 7.5\mu\text{m}$  and thickness of  $h_{\text{RBC}} = 2.0\mu\text{m}$  [17]. Capillaries in the circulatory system can be as narrow as  $5\mu\text{m}$  in diameter, therefore, RBCs are highly deformable in order to allow their passage [13]. Severe RBC deformation is made possible by several factors: Foremost, the cell membrane is composed of a lipid bilayer and spectrin cytoskeleton, affording flexibility and strong structure [18]. Secondly, unlike WBCs, the interior of RBCs contain no nuclei as they would inhibit deformation. Finally, due to the area and volume conserving properties of the lipid bilayer and cytosol respectively, deformation would not be possible if RBCs were spherical. As such, RBC deformability is in part due to their non-spherical shape, which allows alterations in shape while maintaining constant surface area and volume. The characteristic discocyte RBC shape can be seen in figure 1.1. In addition to elasticity, the aforementioned RBC properties enhances their ability to store and transfer oxygen [19]. Discocytes have a large surface area to volume ratio, enabling oxygen and carbon dioxide to readily diffuse across the RBC plasma membrane and surrounding capillary walls. Furthermore, the extra space afforded by the absence of nuclei and other organelles allows for more haemoglobin and hence increases oxygen carrying capacity.

### 1.2.2 *Diagnosis from Blood*

Given that the cardiovascular system is fundamental to healthy function in the body, it is unsurprising that many medical conditions are affected by, or indeed can affect, the properties of blood. Consequently, blood tests are the most common technique when trying to make diagnoses or monitor the effectiveness of drugs in clinical tests. For example, concentrations of various waste products or enzymes can be measured from a blood sample, indicating kidney or liver function. Additionally, elevated anti-body and WBC counts indicate that the immune system is fighting an infection or illness. In many of the tests performed, it can be useful to separate whole blood into its constituent components. This allows the individual inspection of each component and also protects the viability of other materials which might be required for other tests. The fractionation of whole blood into RBCs, WBCs and platelets has been achieved using DLD devices by discriminating against size [9]. This could be useful in so far as measuring the RBC, WBC and platelet counts in a patient. However, it is also possible to glean more information using DLD methods to analyse blood samples. For instance, deformability based separation of RBCs has been demonstrated and the enrichment of pathogenic particles (such as trypanosomes and circulating tumour cells) from blood has also been achieved [8, 10]. In each of these examples, the DLD device is tailored

specifically for the task of separating the particles of interest. With such specialised design necessary, there are many separation tasks for which there are no sorting schemes. In particular, a DLD device able to sort RBC populations based on their mechanical properties could be of significance in diagnostics as some diseases are known to alter RBC properties. One such disease is malaria, a parasitic infection whose life-cycle relies heavily on the ability to invade and multiply inside the RBCs of it's host.

### 1.2.3 Malaria

Malaria is a disease caused by the *plasmodium* family of parasites which are transmitted to humans through bites from infected mosquitoes. In 2015, nearly half the world's population were at risk from malaria and the World Health Organisation (WHO) estimates 212 million cases of malaria occurred, with 430000 of these cases resulting in death [20]. Malaria can progress rapidly to life threatening stages of the disease, this is especially true for people with low immunity, and severe infection almost always results in death if untreated. Consequently, early diagnosis is essential to ensure prompt and accurate treatment is administered. Targeted treatment is necessary because there are 5 strains of *plasmodium* parasite which affect humans, 2 of which - *P. falciparum* and *P. vivax* - are responsible for the majority of cases [21]. Furthermore, incorrect drug administration is not only ineffective, it also promotes the development of drug resistance. Diagnostic equipment needs to be easy to use, non-invasive, and inexpensive, as many of the locations in which malaria is endemic do not have access to the highly trained staff or expensive equipment available to non-rural communities [21]. Consequently, the label free sorting facilitated by micropillar arrays, and the relatively inexpensive and scalable fabrication process of microfluidic devices, makes DLD a good candidate for point-of-care malaria diagnostics.

The life-cycle of malaria parasites relies on their continual transmission between two types of host, humans and mosquitoes. This cycle involves several stages, seen in figure 1.2, and in each stage the parasite adopts a different form:

1. A malaria-infected female mosquito taking a blood meal injects sporozites into a human host.
2. The sporozites infect the liver cells, multiplying and forming schizonts which eventually rupture, releasing merozoites into the blood.
3. Merozoites in the blood stream invade RBCs and mature into schizonts. Again the schizonts rupture, bursting the RBC and releasing more merozoites into the blood stream, where some develop into male or female gametocytes. The growth of parasites during this stage and the resulting change in RBC properties can be divided into sub-stages, which will be looked at in more detail later (see figure 1.3a).

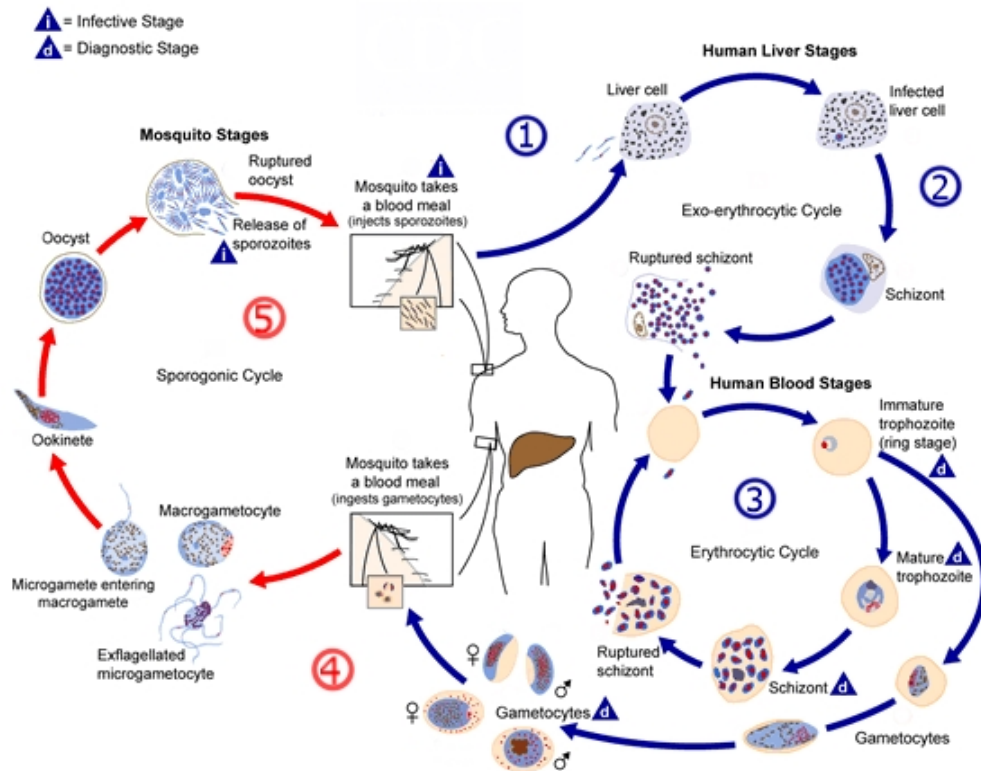


Figure 1.2: The life cycle of plasmodium parasite. The cycle can be divided into 3 main stages: (i) Exo-erythrocytic - following transmission, parasites multiply inside liver cells, rupturing into the blood stream when sufficient merozoites are formed. (ii) Erythrocytic - parasites invade the RBCs, where they multiply to form more merozoites, some of which develop into gametocytes. (iii) Sporogonic - gametocytes ingested by a mosquito multiply to eventually form sporozoites, allowing the cycle to begin again from the start. Source altered from [Centers for Disease Control and Prevention](#)

4. A mosquito ingests gametocytes whilst taking a blood meal. The male and female gametocytes conjoin, generating zygotes which develop into oocysts, harbouring many sporozoites.
5. The oocysts eventually rupture and the sporozoites relocate to the mosquito's salivary glands. After the mosquito takes another blood meal sporozoites are transferred to a new human host, perpetuating the cycle [22].

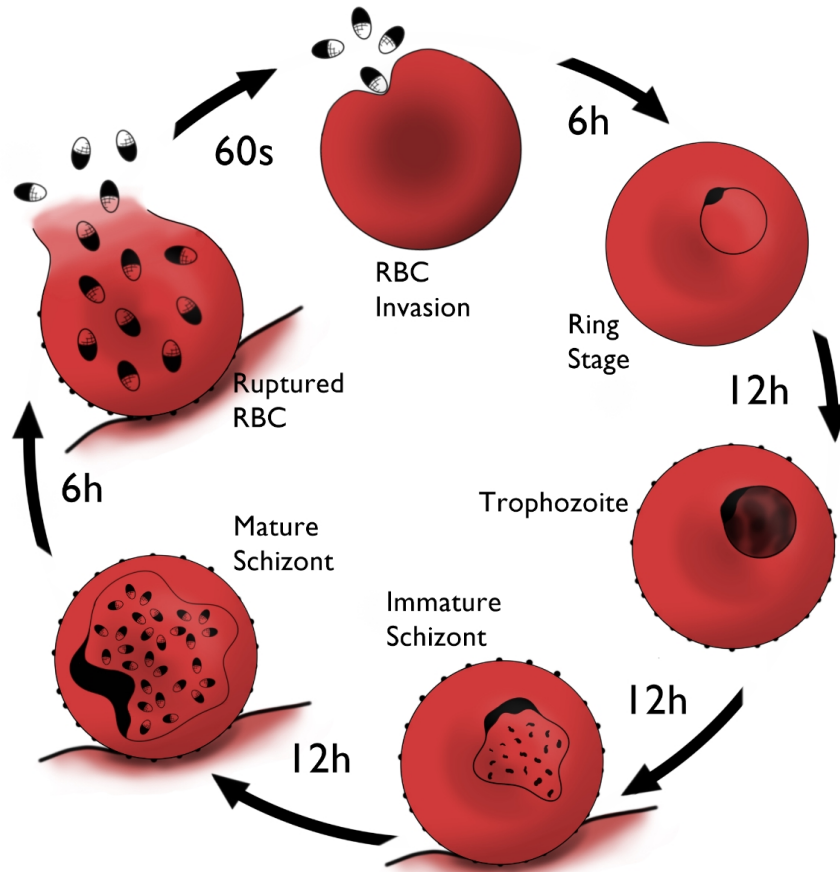
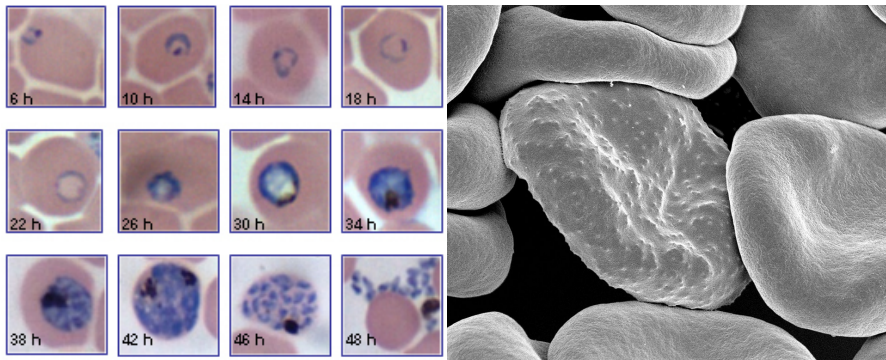
During the erythrocytic phase of the plasmodium life cycle, parasites are mostly undetected by WBCs because they spend the majority of this development stage hidden inside RBCs, see figures 1.3a and 1.3b. However, the invasion, multiplication and maturation of parasites causes multiple mechanical changes to RBCs. These changes can be identified by the spleen, which has the function of removing abnormal erythrocytes from the blood [23]. In order to avoid complete splenic removal, as *P. falciparum* parasitized RBCs mature they adhere to the endothelium walls of the cardiovascular

lar system [24]. As such there is a brief time period in which a parasitized RBCs are present in the blood stream and hence obtainable by blood sample for diagnostic purposes. The exact nature of the mechanical changes to parasitized RBCs, and the time period when they're detectable in blood samples, depends on the plasmodium species. The two dominant species of malaria parasite are plasmodium *falciparum* and plasmodium *vivax*, the former is responsible for 99% of malaria fatalities and is prolific in Africa, whilst the latter is less virulent it accounts for the majority of malaria cases in South America and Asia [20].

*P. falciparum* has been shown to increase the shear modulus of infected RBCs throughout the erythrocytic cycle [25] and the shape of RBCs change drastically in the latter stages of the cycle [26]. The exact mechanisms behind the change in rigidity is poorly understood, however, the nodules introduced in the cell membrane during the trophozoite stage of *p. falciparum* (see figure 1.3c) [27], the consumption of haemoglobin [28], and foreign mass of the parasite are all possible candidates. Furthermore, there is some experimental evidence that the internal viscosity of the RBC increases with infection [29]. *P. falciparum* avoid splenic removal by adhering to endothelium walls and *P. vivax* avoids splenic removal by increasing the elasticity of the cell membrane to prevent detection of the increase in RBC size which inevitably comes with parasite growth. These two different methods of avoiding splenic detection are responsible for the different virulences of the plasmodium species. The cytoadherence of trophozoite stage RBCs infected by *p. falciparum* can disrupt the function of major organs. In cerebral malaria, adherent trophozoites prevent oxygenation of the brain, resulting in possible loss of consciousness, neurological disorders and coma [30].

The physical alterations of RBCs which occur during the early erythrocytic stages of the plasmodium life cycle might form the premise for a label free sorting scheme to isolate the sparse infected cells and hence help in the diagnosis of specific strains of malaria infection. Seeing as DLD has already been demonstrated as a viable technique for sorting based on deformability in unoptimised devices, sensitivity to small changes in mechanical properties should be possible with refinement of device designs. Simulations methods will be a valuable tool in helping optimise device designs for very specific tasks such as the diagnosis of malaria.



(a) *P. falciparum* Erythrocytic Cycle.(b) *P. falciparum* Infection Stages.

(c) Trophozoite Nodules.

Figure 1.3: (a) The 6 main erythrocytic stages of *p. falciparum*. Note, merozoites are in the blood stream for approximately 60 seconds before they invade a new RBC and trophozoites cause RBCs to develop sticky nodules which adhere to endothelium tissue. This leaves a brief window for parasite detection using blood tests. (b) Images of the infection stages of *p falciparum* in RBCs over the course of it's 48h life cycle. Image released to public domain, originally published here [31]. (c) A scanning electron microscope image of a malaria infected RBC with nodules (center) surrounded by uninfected RBCs. Sourced from [National Institute of Allergy and Infection Diseases](#)

### 1.3 MICROFLUIDIC PARTICLE SORTING

The cell sorting techniques used within microfluidic devices can be divided into three categories based on the primary method of cell recognition: 1) fluorescent label-based, 2) bead-based, and 3) label free sorting. Each of these categories can be further subdivided into groups depending on the physical processes employed to achieve sorting.

#### 1.3.1 *Fluorescent Label-Based Sorting*

Fluorescent label-based sorting distinguishes cells by labelling different cell-types with different fluorescent probes [3]. A traditional schematic for the FACS technique is shown in figure 1.4a, the entire sorting process can be divided into three stages:

1. Serial cell interrogation: Each cell is encapsulated in an aerosol droplet. The scattering pattern produced by a laser beam incident on each droplet is recorded as they traverse the main channel in single file.
2. Real time classification: The scattering pattern is then rapidly analysed and cross-checked with the scattering signatures of the fluorescent markers in use, identifying the cell type.
3. Command driven sorting: Based on the identified cell type, the aerosol droplet is given some charge and then sorted electrostatically, where varying magnitudes of electric field strength perturb the droplet's path by different amounts.

In the case of FACS-type microfluidic devices, the first and second stages are carried over from the classic technique, however a variety of techniques are employed to sort the particles. Furthermore these techniques are not limited to use in FACS devices, and are utilised in all kinds of microfluidic devices which require the spatial manipulation of cells.

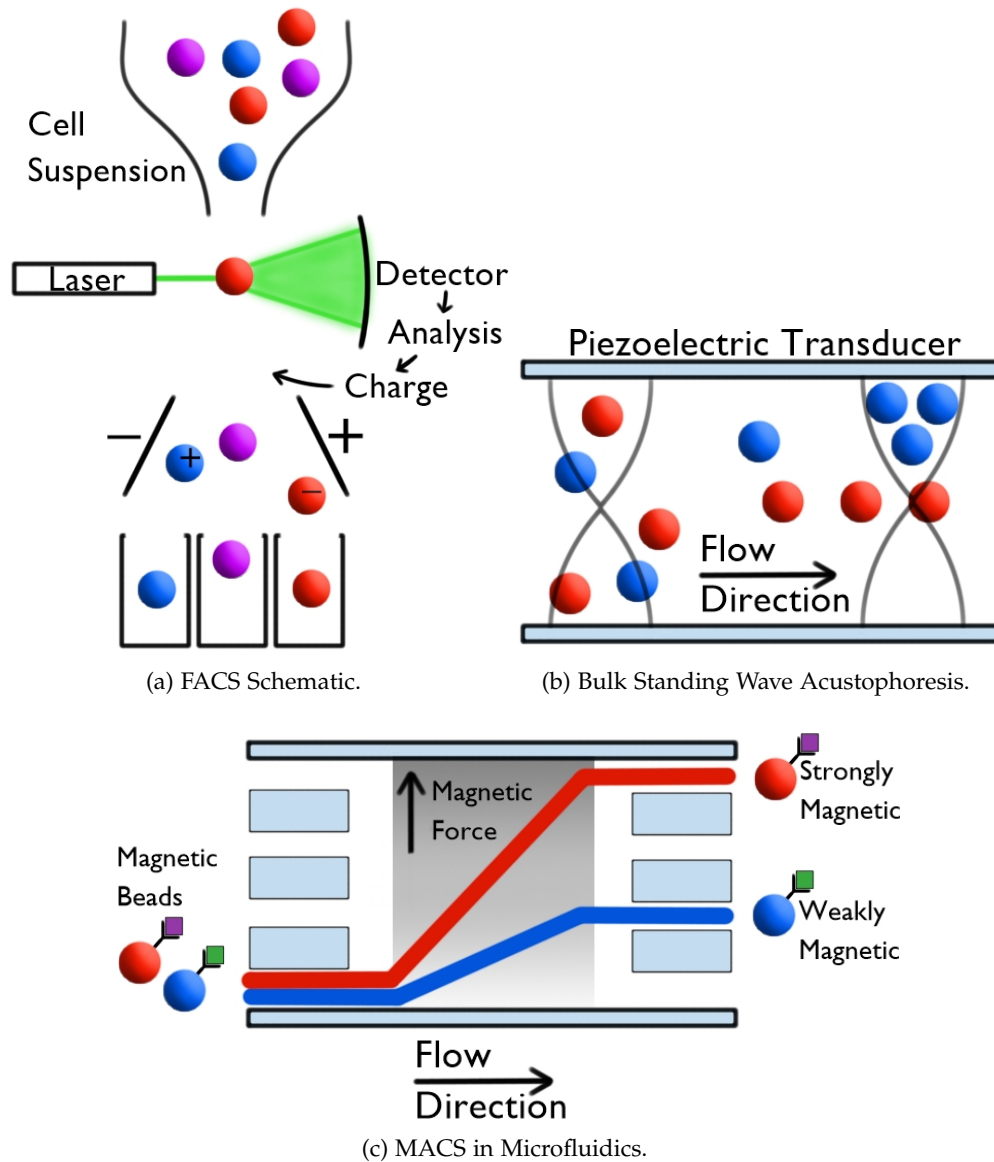


Figure 1.4: (a) A schematic of a typical FACS setup. Two specific cell types (blue and red) within a heterogeneous population of cells are marked with two types of fluorescent label. The scattering pattern detected from an incident laser on aerosol droplets containing the cells is analysed to identify if the cells are marked with one of the two fluorescent labels or unmarked. If labelled, the droplet is administered with a negative or positive charge depending on the type. Charged plates deflect the aerosol droplets according to their charge, sorting the cell population in two distinct red and blue populations, and one waste population of unmarked cells (purple). (b) A schematic of using bulk standing waves to sort two cell types with different acoustic properties. Red particles have a positive acoustic contrast factor  $+\phi$  compared to the suspending medium, meaning the focus at the standing wave's node. Blue particles are less dense than the surrounding medium with  $-\phi$  and consequently collect at the anti-nodes. (c) A schematic of MACS being used in a microfluidic channel. Two beads with different magnetic susceptibility bind to two different cell types in a sample. When exposed to a magnetic field perpendicular to the flow, the bound beads migrate at different rates, resulting in separation at the end of the channel.

### 1.3.2 *Active Label-Based Sorting*

As an alternative to the explicit application of charge to aerosol droplets used in typical FACS devices, electromagnetic forces can displace cells immersed in fluid directly by taking advantage of inherent electrostatic properties of cells or encapsulating droplets relative to the surrounding suspending medium [32, 33]. Electrophoresis uses a spatially uniform electric field driven by direct current to continuously displace cells. Depending on the chemical make up of a cell, the surface charge is often positive or negative, resulting in migration towards the anode or cathode. Electrophoresis has seen successful use in FACS style microfluidic devices, sorting cells previously identified using fluorescence labelling [34]. Furthermore, electrophoresis has achieved extremely high throughputs by sorting cells encapsulated in oil droplets immersed in water [35].

In instances where cells have neutral charge, dielectrophoresis (DEP) provides an alternative electrokinetic technique. A non-uniform field generated by an alternating or direct current induces a dipole moment across a cell depending on its electric permeability [33]. As the field is non-uniform, the pole of the cell subject to the strongest electric field will dictate the movement of the cell. The magnitude of force experienced depends on the size of the cell and its permeability relative to the suspending medium. As such, DEP is a useful technique for sorting cells based on their size and dielectric properties. In addition to direct manipulation of cells, several groups have used DEP to sort single cells contained in water-in-oil droplets, providing a valuable alternative to the often biohazardous aerosols used in FACS [36, 37]

Acoustophoresis is a method for displacing particles by application of acoustic pressure waves [38]. Acoustofluidic technologies have seen considerable interest in microfluidics for cell sorting applications, as acoustic forces are particularly well suited to cell manipulation. Cell sorting can be achieved with continuous high-throughput, with high degrees of accuracy, and without compromising the viability of the sample [39]. A variety of different acoustic wave orientated methods can be used for spatially sorting cells.

Bulk Acoustic standing waves are standing waves whose primary resonance mode's wavelength matches the spatial dimensions of the microfluidic channel. Cells travelling through the microfluidic channel experience a radiation pressure dependent on their density and compressibility relative to the suspending medium, and to their internal volume [40]. Figure 1.4b shows a schematic of sorting a cell population with positive and negative acoustic contrast factors  $\phi$  relative to the suspending medium. These types of standing wave have been used in conjunction with fluorescence labelling and detection to achieve cell sorting [41].

Surface acoustic waves (SAW) on the floor of a microfluidic channel can also be used to manipulate particle flow. Standing SAWs (SSAW) induced by transducers are transferred into the buffer fluid contained within the channel, creating well defined flow streams for suspended cells to follow [42]. Such devices are of significance in

fluorescence label-based sorting as they have the capacity to divert cells into multiple different channels, allowing for the sequential sorting of diverse populations of cells [43, 44]. While the majority of acoustofluidic devices utilize some kind of standing wave for cell manipulation, travelling acoustic waves have also been used to sort cells at rates exceeding 1000 cells/sec [45].

Finally, in addition to forces exerted via acoustics or electrokinetics, cells can be handled using highly focused optical beams [46]. Optical manipulation of cells is highly coveted as it allows precise control of objects as small as atoms in 3-dimensions and preserves cell functionality [47]. Optical trapping occurs as a result of the scattering and gradient forces produced when a laser beam crosses two regions of differing refractive index, in this case the suspending fluid and the intracellular medium. Recent developments have allowed a reduction in size of optical devices, making the suitable for microfluidic devices and optical switches have been used successfully for sorting cells in fluorescence labelling schemes [48].

### 1.3.3 Bead-Based Sorting

FACS has the disadvantage of requiring serial analysis and separation of cells. Additionally, the fluorescent labels do not actively contribute towards the mechanical sorting process itself. These disadvantages have led to the development of bead-based sorting mechanisms, where a targeted cell is labelled with beads with specific mechanical properties. The adhesion of these beads allows for the cell to experience forces from external fields that unbound cells do not feel. Consequently, whole cell populations can be exposed to an external field and all of the bound cells can be separated simultaneously, representing a significant throughput increase compared to FACS methods. The first bead-based approach was used in 1989 on a bench top sorter using magnetic beads [4], where by superparamagnetic nanoparticles target surface antigens specific to certain cell types and allow their separation following application of a magnetic field. The work by Miltenyi *et al.* represents the inception of the magnetic activated cell sorting technique (MACS) [4], which is now the second industry standard for cell sorting along side FACS.

Magnetophoresis (MAP) refers to the use of magnetic fields to manipulate cells labelled with magnetic beads or which are inherently magnetic themselves. Bead-based approaches to sorting often use nanoscopic magnetic particles to label the desirable cells. The labelling process can target rare cells for their subsequent isolation or it can be used to remove large numbers of unwanted bulk cells from a sample. An example of using two bead types with different magnetic susceptibility to separate two cell types is shown in figure 1.4c. MAP was first used in microfluidic devices to simply separate labelled and unlabelled cells in free flow [49, 50]. Since then, MAP has shown promise

in isolating extremely rare cells, such as sorting circulating tumor cells (CTCs) from blood cells at ratios as low as  $1 : 10^9$  [51].

In acoustophoresis cells exposed to standing waves tend to focus at the nodes due to their high density relative to surrounding fluid, elastomeric beads are much lower in density and, as a result, focus towards the anti-nodes [52]. Consequently, elastomeric beads show promise in cell sorting in acoustofluidic devices. Labelling cells with elastomeric beads allows continuous focusing of labelled and unlabelled cells into separate flow streams at the antinodes and nodes of the acoustic standing wave respectively [52], see figure 1.4b.

Finally, bead labelling can be employed to alter the effective size of cells and as a result, change the dielectrophoretic forces they experience when placed in a non-uniform electromagnetic field [33]. Bead labels allow cells which would otherwise be inseparable due their identical morphology to be sorted using DEP. [53].

#### 1.3.4 *Active Label-Free Sorting*

While the aforementioned label dependant sorting schemes relied on surface binding of specific markers to cells in order to achieve separation, label-free methods rely on the inherent physical properties of cells. Cell sorting is achieved by exploiting the differences in size, morphology, deformability, density, polarizability and magnetic properties. Many of the active methods of cell handling used in labelled sorting have their place in label free sorting. For example, acoustophoresis has been used for label-free sorting of cells according to their size [54, 55]. In the simplest case, a population of heterogeneously sized cells are pre-focused at streamline away from the node of an acoustic standing wave which spans a microfluidic channel. The larger cells experience a greater forces in the standing wave and hence migrate more rapidly than smaller cells towards the nodes. If the channel length is chosen appropriately, this phenomena allows for the collection on different sized cells at the end of the channel, as each will have displaced a different amount towards the standing wave nodes.

Additionally, DEP has seen use in label-free cell sorting, discriminating cells based on their dielectric properties [56]. Many schemes use arrays of insulating pillars placed across an electric potential to generate a non-uniform electric field which cells interact with differently depending on their size and electric permeability [57]. Other schemes use a method called isoelectric separation, where two suspending mediums of differing conductivity are mixed to generate a monotonic conductivity profile which in turn results in a conductivity gradient across then fluid when electrodes are placed along the sides of the channel. Due to dielectrophoretic forces, cells immersed in this fluid are driven towards a point in the conductivity profile where their net polarization vanishes. As such, populations of cells with distinguishable electrical properties arrive at different isoelectric points and are continuously sorted [58].

Although magnetophoresis is predominantly used for sorting in labelled cell schemes, there are some exceptions. Erythrocytes are rich in iron due to their haemoglobin content and consequently they can be manipulated using magnetic fields [59]. MAP has been used as in sample preparation of whole blood, removing RBCs to leave behind WBCs platelets and plasma [60]. Furthermore, ferrofluids or paramagnetic solutions can be used as a suspending medium, which when exposed to a magnetic field can be used to sort diamagnetic cells based on their size [61].

#### 1.3.5 *Passive Label-Free Sorting*

The final group of sorting methods left to discuss do not require the use of fluorescent labels or bead markers, nor do they rely upon the application of external fields to manipulate cells. The behaviour of cells in microchannel flow depends on a complicated interplay between cell properties, channel geometry and fluid dynamics. Consequently it is possible to take advantage of the rich variety in morphological and mechanical properties found in the cellular world, and use these variations as a basis for separation. This style of sorting is called passive cell sorting [62].

Under the correct flow conditions, inertial forces result in the migration of particles across the stream lines defined by the fluid flow. Two examples of these phenomena are Dean Flow and inertial focusing, both of which are used for passive cell sorting [63]. Dean flow occurs when fluid contained within a channel flows around a bend. The velocity profile enforced by the channel results in a disparity between the velocity of fluid at the channel center and walls. Hence, fluid at the channel center has a higher inertia than that at the walls, and a pressure gradient occurs in the channel bend in the radial direction, causing secondary fluid flow. The interaction strength between circulating fluid in secondary flow and suspended particles depends on the particle size, and consequently serpentine and spiral shaped fluid channels have been used for passive size-based sorting in microfluidics [64, 65].

Inertial flow focusing results from multiple competing fluid dynamic effects, which ultimately result in particles of different size, shape and compressibility being focused at different equilibrium positions along a channel cross section in a phenomena called the Segré–Silberberg effect [66]. One component of inertial focusing is called the inertial lift force, which originates at the channel wall-fluid boundary and acts to push particles towards the channel center. The lift force is counteracted as a result of gradients in shear flow which occur in nonlinear velocity flow profiles, as found in Poiseuille flow [63]. Cells and particles of different sizes have been sorted using inertial focusing by collecting them after they have reached their size-dependant equilibrium positions in the flow [67].

In addition to inertial effects, there are numerous filtration based methods which have been used to passively sort cells based on size and deformation: (i) Hydrophoretic

filtration uses pressure gradients generated by slanted arrays of obstacles along microchannel walls to focus cells according to their size or density [68]. (ii) Size exclusion filtration systems consist of a series of pillar arrays whose post-to-post spacing decrease as a function of distance along the channel. Oscillating flow generates a ratchet effect, trapping larger or less deformable cells towards the beginning of the channel and only permitting passage to increasingly smaller cells further along the channel [69]. (iii) Cross filtration methods utilise tangential flows to sort cells. The crossing flows are divided by narrowly spaced obstacles which only allow sufficiently small particles access to the tangential stream, hence dividing a cell population in two based on their sizes relative to some critical diameter defined by the post spacing [70].

Deterministic lateral displacement (DLD) is a passive cell sorting method which the body of this work focuses on, specifically the manipulation of non-spherical and deformable cells using DLD. The key sorting mechanism in DLD relies upon particle interactions with an obstacle array. A periodic array of microposts, whose successive rows of pillars are shifted by some distance, defines a critical radius  $R_C$ . Particles traversing the array whose radii are less than  $R_C$  follow the fluid flow, however particles larger than  $R_C$  are bumped across flow streamlines, causing their continuous lateral displacement [6]. DLD has been shown to reliably separate different sizes of polystyrene beads and the value of  $R_C$  in relation to post size and spacing has been well established for rigid spherical particles [7]. Using these principles, devices have been successfully developed for sorting the components of whole blood and for isolating CTCs and parasites from blood [9, 71]. Furthermore, the DLD technique is demonstrably sensitive to cell deformability [72]. However, DLD design for deformability based sorting is complicated because the concept of cell size relative to  $R_C$  becomes dubious when the cell in question is non-spherical, rotating or dynamically deforming in flow. Consequently, further steps are needed to refine the DLD method for sorting the majority of bioparticles.

#### 1.4 PHYSICAL AND NUMERICAL BASIS

Precise descriptions of fluid flow in microfluidic channels, and the resulting dynamic behaviour of bioparticles suspended in these flows, is vital to the development of effective cell sorting schemes in microfluidic devices. This section introduces the relevant physical theory and numerical techniques essential for describing complex systems such as those found in microfluidic devices.

##### 1.4.1 *Hydrodynamics*

Hydrodynamics is the study of flowing liquids and the forces experienced by bodies immersed in fluid. The three fundamental laws which underpin hydrodynamic theory



are the conservation of mass and momentum. When applied to an incompressible Newtonian fluid (i.e. an isotropic fluid whose viscosity does not depend on the stress rate or velocity of flow), these conservation laws yield the incompressible Navier-Stokes equations (NSE)

$$\begin{aligned} \rho \left( \frac{\partial \mathbf{u}}{\partial t} + (\mathbf{u} \cdot \nabla) \mathbf{u} \right) &= -\nabla p + \eta \nabla^2 \mathbf{u} + \mathbf{f}, \\ \nabla \cdot \mathbf{u} &= 0 \end{aligned} \quad (1.1)$$

with the density  $\rho$ , velocity  $\mathbf{u}(\mathbf{r}, t)$  at position  $\mathbf{r}(t)$ , dynamic viscosity  $\eta$ , pressure  $p(\mathbf{r}, t)$ , and external applied forces  $\mathbf{f}$  [73]. The NSE are used widely throughout physics and engineering, and they are often simplified depending on the system in question. Simplifications can be made based on the ratio of inertial forces and viscous forces in the system, a property characterized a dimensionless quantity called the Reynolds number

$$Re = \frac{\rho U L}{\eta} \quad (1.2)$$

where  $U$  and  $L$  are the system's characteristic velocity and length scale respectively. The numerator in equation 1.2 represents inertial contribution and the denominator represents the strength of viscous effects. Systems whose Reynolds number is  $Re \gg 1$  are said to be inviscid and viscous effects can be ignored. In this case the NSEs reduce to the Euler equations [74]. Conversely, a low Reynolds number  $Re \ll 1$  indicates that viscous effects are entirely dominant and the inertial effects can be ignored. Here the fluid can be thought of as discrete laminae which do not mix due to the fact that there is no appreciable convection in the fluid. In this instance the NSE equation for steady state flow reduces to the Stokes equation 1.3

$$\nabla p - \eta \nabla^2 \mathbf{u} = \mathbf{f} \quad (1.3)$$

This approximation is easily demonstrated by non-dimenonlizing the NSE using the dimensionless variables  $\mathbf{r}^* = \mathbf{r}/L$ ,  $\mathbf{u}^* = \mathbf{u}/U$ ,  $t^* = tL/U$  and  $p^* = pL/\eta U$  such that 1.1 becomes

$$Re \left( \frac{\partial \mathbf{u}^*}{\partial t^*} + (\mathbf{u}^* \cdot \nabla) \mathbf{u}^* \right) = -\nabla p^* + \nabla^2 \mathbf{u}^*$$

where it is clear that the l.h.s reduces to zero in the limit of  $Re \ll 1$  [73].

#### 1.4.2 *Soft Matter*

Soft matter physics is the study of materials whose key physical behaviours occur at the same energy scales as thermal energy experienced at room temperature or in the human body. Often such materials cannot be described as Newtonian fluids or conventional solids. Materials studied in soft matter include colloid suspensions, polymers solutions or melts, liquid crystals and mixtures of biomaterials such as membranes and vesicles. Furthermore, the internal structures of soft matter materials are often defined by mesoscopic length scales, making atomistic or macroscopic descriptions inadequate for describing their salient properties [75].

The sorting of bioparticles in microfluidic devices will be dependent on many of the phenomena explored in soft matter physics as cells are composed of a variety of soft materials. For instance, the human RBC is composed of multiple soft materials which define its physical properties. The outer membrane is a lipid bilayer with viscoelastic properties and the elastic cytoskeleton spectrin network is able to facilitate the extreme deformations experienced in the microvasculature system [76]. Consequently, the complex mechanical properties of bioparticles have to be taken into consideration when designing microfluidic devices which are intended to sort them.

#### 1.4.3 *Simulations*

In recent decades, there have been numerous experimental, theoretical and computational works carried out to study the physical processes which govern soft matter systems. However, due to the degree of complexity and the broad range in relevant time/length scales, it is hard to find a theoretical basis to understand the phenomena observed in soft matter systems. Experimental approaches allow invaluable insight into specific behaviour observed in such systems but they are often time consuming and expensive. Computer simulations provide an alternative approach for studying physical systems and, with the steady advancement of computing hardware, have seen increasing application for investigating the complex problems in soft matter physics.

Three main computational techniques are used for soft matter simulations: Continuum methods (NSE), molecular dynamics (MD) and mesoscopic methods. At the macroscopic level, fluid dynamics can be well described by solving the continuum NSE using numerical discretization techniques such as finite -differences, -elements, and -volumes, [77–79] or more advanced approaches such as mesh-free and the forced-coupling methods [80, 81]. However, these techniques are based upon the NSEs; theory which was developed prior to the conclusion of the debate over whether matter existed as a continuum or was composed of discrete objects (atoms). Consequently, the microscopic details of fluid dynamics captured by the NSEs are purely phenomenological, and often unsuitable for the treatment of soft matter systems. Detailed simulations of

fluid at a microscopic or even nanoscopic scale are made possible with MD techniques [82, 83], however these are limited to nano time scales and extremely small volumes of fluid. Here, the momentum and position of every atom is followed individually, allowing for accurate simulations when the continuum hypothesis breaks down. Due to the computational intensity of these simulation techniques, they are limited to simulating small numbers of atoms and the time scales relevant for hydrodynamic effects are unobtainable without large computational cost.

Mesoscale techniques attempt to cover the important characteristic time and length scales of soft matter systems by incorporating elements used in both micro and macro-scale simulations. Multiple mesoscopic simulation schemes have been devised over the years, including:

- Brownian dynamics (BD) uses stochastic forces to represent the thermal fluctuations (TF) transferred from a solvent to immersed particles [84]. Consequently, the diffusive behaviour is captured in the classical BD method but hydrodynamic interactions (HI) are omitted. The addition of an interaction tensor called the Rotne-Prager-Yamakawa tensor couples particles such that they experience the hydrodynamic forces which arise from disturbances in flow caused by neighbouring particles [85].
- The lattice Boltzmann (LB) method models fluid as particles which are constrained to a discrete lattice mesh, which they explore via successive propagation and collision steps. Given that fluid particles are modelled explicitly, LB includes the effects of HI. In the initial development of LB, TF were neglected but the method was later adapted to include stochastic motion within the fluid particles [86, 87].
- Multiple particle collision (MPC) dynamics is a particle-based simulation method which incorporates both HI and TF [88]. Unlike the LB method, particles have continuous coordinates and velocities, and the method satisfies Galilean invariance. The simulation process consists of two stages: (i) In the streaming step, particles move ballistically according to their current velocity. (ii) In the collision step, particles are organised into cells. The velocity of the particles in each cell are randomly rotated relative to the velocity of each cells center of mass. Furthermore, the continuous spatial shifting of the grid defining the cells ensures Galilean invariance.
- Dissipative particle dynamics (DPD) is a stochastic particle-based simulation technique [89]. It was initially developed to overcome the artefacts observed in lattice-based methods and to extend the time and length scales available to MD techniques. Instead of considering individual particles, as in MD, each particle represents a region of fluid. Particle-particle interactions are governed via soft

pairwise potentials which account for dissipative and conservative forces. A final random force accounts for thermal fluctuations in fluid. The initial work was further improved and given a sound basis in statistical mechanics such that the method satisfied the fluctuation-dissipation relation for the grand canonical ensemble [90, 91]. DPD has been used successfully for complex soft matter systems at mesoscopic time and length scales, such as the for the filtration of DNA and bioparticles [92, 93].

- Smoothed dissipative particle dynamics (SDPD) is a combination of the DPD technique and smoothed particle hydrodynamics (SPH) [94, 95]. It is advantageous to DPD because the inherent properties of the fluid such as viscosity and equation of state are directly obtained from the input parameters of SDPD, whereas in DPD these properties must be measured by fitting simulation results to hydrodynamic theory. SPH is a technique for discretizing the NSE and was initially developed for simulating systems in astrophysics. The physical properties of each particle can be calculated by considering all surrounding particles within a certain distance called the smoothing length. The weighting of each particle's contribution depends on its density and distance, as defined by a smoothing kernel. In large astrophysical systems, thermal fluctuations are of little importance, so they are ignored in SPH. However, in soft matter, thermal fluctuations are vital and the random forces used in DPD are included in a manner consistent with that found in DPD, to yield SDPD. Finally, further adaptations to SDPD ensure conservation of angular momentum, a quantity which was not conserved in the initial method [96].

The body of simulations used in this work use DPD and SDPD to represent solvent and also for coupling of suspended particles to fluid.

## 1.5 RED BLOOD CELLS IN FLOW

As previously mentioned, whilst successful sorting of bioparticles in DLD devices has been demonstrated [8, 10], device designs often appeal to theory for rigid spheres and considers the effective size of bioparticles. However, beyond taking the smallest dimension of the bioparticle in question, it is often complicated to predict what the effective size will be. Furthermore, in non-dilute cell suspensions, cell-cell interactions and cooperative behaviours may have an impact on cell sorting. The implications for these complex effects on cell sorting have seen limited focus but promising steps are being made [97]. However, numerous experimental and numerical studies on the cooperative and dynamic behaviour of bioparticles in more simple geometries exist. For example, the motion of RBCs in tube flow has many important implications for function in the microvasculature, motivating enormous attention [98].

### 1.5.1 RBC Shape and Dynamics

RBCs and other encapsulated fluids in shear flow have been shown to demonstrate a broad variety of interesting dynamic behaviours [99, 100]. Exact cell shape and dynamic behaviour depends on factors such as confinement, deformability, flow conditions, age and pathophysiological state [101]. Three commonly observed RBC behaviours in shear flow are tank-treading (TT), tumbling (TB) and snaking. While tank treading, an RBC's membrane migrates around the cells fixed shape in response to shear forces exerted by surrounding flow, similar to the continuous motion of tank treads around interior wheels. In TB behaviour, the RBC membrane remains fixed relative to the interior fluid, and the entire cell flips about it's center of mass. Finally, snaking behaviour is observed at very low shear rates where RBCs undergo regular oscillatory motion [102].

The exact dynamic behaviours of RBCs depend heavily on the surrounding flow profile. For example, fluid flow in tubes results in a poiseuille flow profile, and at high enough flow rates RBCs adopt a stable parachute shape [102], while in contrast RBCs in couette flow at high shear rates transition from regular TB behaviour to tumbling tri-lobe and quadra-lobes [99]. Furthermore, the shear rates at which transitions occur depend heavily on the physical properties of the RBC and surrounding fluid. Altering the ratio between the interior RBC and surrounding fluid results in preference for different RBC dynamics. Matching intra and extra-cellular fluid viscosities tends to result in TT motion [103], whilst at physiological conditions where suspending plasma is 5 times less viscous than the RBC cytosol, RBCs more commonly exhibit TB motion [99]. Additionally, the elastic properties of the RBC membrane also effect the transition between different dynamic behaviours and shapes [103].

### 1.5.2 Collective RBC Behaviour

RBCs are rarely in isolated environments and the behaviour of many-body systems are of extreme relevance in physiology. It is true that the aforementioned RBC dynamic behaviours will have an impact on the overall flow properties of RBC populations. For example, RBCs are known migrate to the low shear rate region in the center of Poiseuille flows [104], resulting in a RBC-free-layer phenomena that occurs in blood vessels [105]. Here, RBCs experience a lift force due to hydrodynamic interactions close to the vessel wall, pushing them radially inwards towards the channel center [106–108]. The absence of RBCs at the vessel walls creates a lubricating effect which reduces the resistance of blood flow. Furthermore, the focusing of RBCs towards the channel center pushes smaller particles such as platelets outwards, where they can better contribute towards hemostasis [109, 110]. however cell-cell interactions also play a major roll in collective RBC behaviour, see figure 1.5a.

A second example of collective RBC effects arises from the aggregation of RBCs into rouleaux formations [111], as seen in figure 1.5b. One hypothesis for the driving mechanism behind this phenomena is that intra-cellular interactions mediated by plasma proteins act as weak attractive potentials [112]. A second theory attributes the aggregation of RBCs to depletion forces caused by polymers in the suspending medium [113]. In actuality rouleaux formation is probably driven by a combination of multiple effects [111]. At low shear rates the RBCs are able to maintain rouleaux structures. However, as shear rates increase, shear forces overcome the weak intra-cellular interactions, resulting in increasingly smaller length rouleaux formations. This phenomena results in a shear thinning effect for whole blood, where the viscosity decreases as a function of shear force [114].

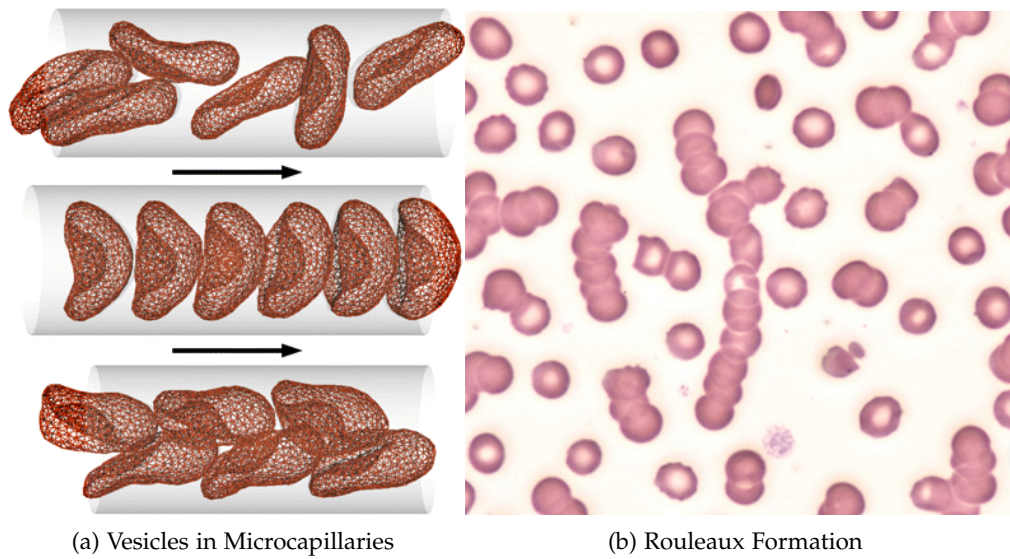


Figure 1.5: (a) Three collective behaviours observed for vesicles in microcapillary flow. (Top) Disordered discocytes are seen at a low flow speed. (Middle) An increase in flow speed results in an ordered phase of aligned parachute shapes. (Bottom) At the same flow speed as for parachutes but higher hematocrit, RBCs change to a slipper shape and organise in a zig-zag fashion. Sourced from McWirther *et al.* [115]. (b) An image of RBCs aggregated in Rouleaux formations of different lengths. Sourced from the [American Society of Hematology](#)

All of the above effects could play significant roles in the treatment of RBCs and other fluid capsule particles in microfluidic devices. Consequently, there is a clear need for further study on the sorting of cells such as RBCs. Device design based on the theory for rigid spheres will not suffice. The complex interplay between cell deformability, cell shape, flow speed, intra and extra-cellular viscosity ratio, and cell-cell interactions need to be considered.

## 1.6 THESIS STRUCTURE

The content of this thesis is organised into five additional chapters:

- i Chapter 2 introduces the numeric techniques used throughout this work to simulate particle transit in DLD devices. First, the mesoscopic particle-based fluid models DPD and SDPD, used in 2D and 3D simulations respectively, are explained. Next, the numerical integration scheme employed for time evolution of the simulated fluid and the treatment of boundary conditions are outlined. Finally, the 2D model for rigid spherical particles and the 2D and 3D variants of the RBC model are introduced, along with the fluid-cell coupling scheme to complete the simulation picture.
- ii Chapter 3 explains the rationale behind particle sorting using DLD devices and explain the experimental procedures used in this work to achieve comparisons with 3D simulations of RBCs. The first section of the chapter looks at the flow fields in DLD devices and how rigid spherical particles or non-spherical deformable particles might behave in such flow fields. In the next section, device design and fabrication are explained. This is followed by a description of the operation of the devices used in this work and the analysis applied to the recorded RBC trajectories.
- iii Chapter 4 presents the results of 2D simulations of rigid spherical particles and RBCs inside DLD devices. Initially comparisons are made with empirical predictions for rigid spheres in circular post arrays. Next, the results of simulations for rigid particles in non-circular post arrays are presented and used to form new empirical predictions for diamond, square and triangular post arrays. Following this, simulations of RBCs in the same post arrays are presented in order to demonstrate the difference in behaviour experienced by non-spherical deformable particles compared to that seen for rigid spheres.
- iv Chapter 5 demonstrates the use of 3D simulations and microfluidic experiments to rationalize the difference in behaviour of non-spherical deformable particles observed in chapter 4. Different DLD device geometries with varying height are used to control the dynamic behaviour available to RBCs and examine how it changes RBC motion in DLD devices. Further study of the effects of dynamic motion are explored by varying the viscosity contrast between intra-cellular and extra-cellular medium.
- v Chapter 6 uses the findings in chapters 4 and 5 to design a DLD device intended for deformability based sorting of RBCs. Pathological values for RBC membrane bending rigidity and shear modulus which correspond to the pathological states observed for RBCs infected by malaria parasites are investigated. 3D simulations

reveal that the dynamic behaviours associated with different values of shear modulus can be used to perform deformability based cell sorting in the DLD device and demonstrates a potential sorting scheme for diagnosis of malaria.

- vi Chapter 7 summarises the results presented in chapters 4 and 5, and discusses their implications for the broader picture of cell sorting introduced in the introductory chapter. Finally, directions for continuation of the work are identified and potential contributions from different fields are suggested.



## NUMERIC TECHNIQUES

---

### 2.1 FLUID MODELS

The simulations in this work employ two particle-based hydrodynamic methods to represent the fluid. The first method is called dissipative particle dynamics (DPD) and is used primarily in the 2D simulations and for coupling the RBC cells to the fluid in 3D simulations. The second method is called smoothed dissipative particle dynamics (SDPD), a combination of DPD with smoothed particle hydrodynamics (SPH), and is used throughout the 3D simulations. In the following section, the theory and motivation for using each method is discussed.

#### 2.1.1 Dissipative Particle Dynamics

In the DPD method fluid is represented by a collection of  $N$  particles which interact with neighbouring particles within a certain cut-off distance  $r_c$  via pairwise additive forces. Each individual interaction is composed of three forces [116]. The first force is a conservative force  $F_C$ , controlling the pressure and compressibility of the fluid. The two remaining forces act as a thermostat, providing thermal fluctuations, keeping the system at equilibrium, and the temperature constant. The dissipative force  $F_D$  accounts for energy loss due to friction between particles and the random force  $F_R$  provides a constant input of thermal energy. The total force acting on the  $i^{\text{th}}$  particle  $F_i$  due to interactions with  $M$  neighbours within a distance  $r_c$  is given by

$$\mathbf{F}_i = \sum_{j \neq i}^M \left( \mathbf{F}_{ij}^C + \mathbf{F}_{ij}^D + \mathbf{F}_{ij}^R \right). \quad (2.1)$$

The conservative force is calculated as

$$\mathbf{F}_{ij}^C = \hat{\mathbf{e}}_{ij} \begin{cases} a_{ij} \left( 1 - \frac{|\mathbf{r}_{ij}|}{r_c} \right), & \text{if } |\mathbf{r}_{ij}| \leq r_c \\ 0, & \text{if } |\mathbf{r}_{ij}| > r_c \end{cases} \quad (2.2)$$

where  $a_{ij}$  is the repulsion experienced between two particles with zero separation and the normal vector  $\hat{\mathbf{e}} = \mathbf{r}_{ij}/|\mathbf{r}_{ij}|$  ensures that the force acts in the direction of the separation vector  $\mathbf{r}_{ij} = \mathbf{r}_i - \mathbf{r}_j$ . The dissipative force is given by

$$\mathbf{F}_{ij}^D = -\gamma \omega_D(\mathbf{r}_{ij}) (\mathbf{v}_{ij} \cdot \hat{\mathbf{e}}_{ij}) \hat{\mathbf{e}}_{ij}, \quad (2.3)$$

and reduces the velocity difference between two interacting particles, dissipating energy via drag. The strength of the dissipation with respect to the particle separation depends on the weight function  $\omega_D(\mathbf{r}_{ij})$  and the dissipative force coefficient  $\gamma$ . The weight function can be chosen according to specific need, in our case and in the original work, it is given by

$$\omega^D(\mathbf{r}_{ij}) = \begin{cases} \left(1 - \frac{|\mathbf{r}_{ij}|}{r_c}\right)^k, & \text{for } |\mathbf{r}_{ij}| \leq r_c \\ 0, & \text{for } |\mathbf{r}_{ij}| > r_c \end{cases} \quad (2.4)$$

where  $k$  can be chosen to alter the viscosity of the DPD fluid. In the initial proposed DPD method the value  $k = 1$  is used and this is the value taken in this work [116]. The random force  $\mathbf{F}_R$  is given by

$$\mathbf{F}_{ij}^R = \sigma \omega_{ij}^R \xi_{ij} dt^{-\frac{1}{2}} \hat{\mathbf{e}}_{ij}, \quad (2.5)$$

where  $\omega_{ij}^R$  is a second weight function,  $\sigma$  is the force coefficient and  $dt$  is the time step. The random component of the force originates from the  $\xi_{ij}$  term and it must satisfy two conditions:  $\xi_{ij} = \xi_{ji}$  to guarantee that total momentum in the system is conserved, and a mean value of  $\langle \xi_{ij} \rangle = 0$  with unit variance. Fluctuation-dissipation theorem requires that the dissipation of kinetic energy in the system is balanced by new kinetic energy introduced to the system by the random force [90]. The following relations guarantee the satisfaction of this criterion,

$$\omega^D(\mathbf{r}_{ij}) = [\omega^R(\mathbf{r}_{ij})]^2, \quad (2.6)$$

$$\sigma = \sqrt{2k_B T \gamma}. \quad (2.7)$$

To summarise, in order to gain access to the length scales which are unavailable to microscopic simulation techniques such as molecular dynamics (MD), the system must be coarse-grained. DPD is a coarse-grained simulation method for modelling complex fluids at mesoscopic length scales. The coarse graining procedure is shown in figure 2.1 and can be conceptualised as the clustering of individual atoms (which interact individually via hard potentials) into large particles (which instead interact via soft potentials). The speed up resulting from coarse-graining is two-fold: Firstly, the number

of particle-particle interactions is drastically reduced, and secondly, the length scales over which soft potentials mediate particle interactions are shorter and hence more computationally efficient than hard Lennard-Jones potentials typically used in MD. One drawback of DPD is that important physical properties of a fluid, such as equation of state and viscosity, are not explicitly chosen when setting the model parameters and instead must be measured directly from simulations.

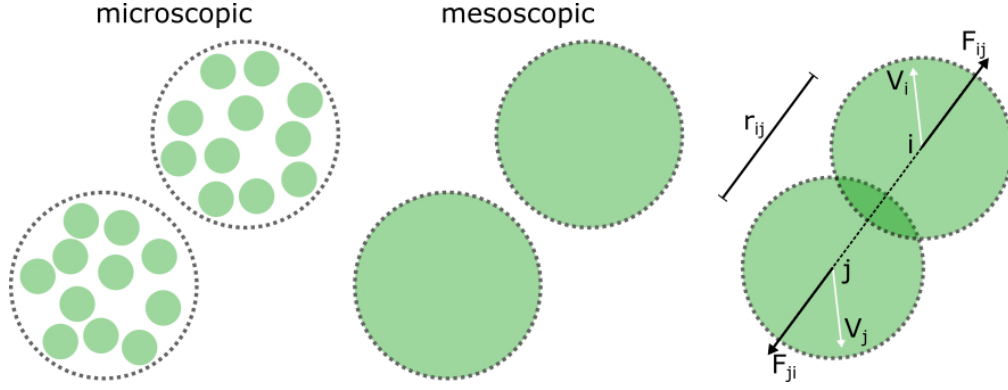


Figure 2.1: The transition from the microscopic picture to the mesoscopic picture. (left) A collection of particles which each represent a single atom. This system operates at very small length and time scales. (middle) A mesoscopic representation of the atomistic system, where clusters of atoms are represented by larger particles. (right) A schematic of two DPD particles experiencing soft interactions. Each of the three forces,  $\mathbf{F}_{ij} = \mathbf{F}_{ij}^C + \mathbf{F}_{ij}^D + \mathbf{F}_{ij}^R$  act along the separation vector  $\mathbf{r}_{ij}$ .

### 2.1.2 Smoothed Particle Hydrodynamics

Similarly to DPD, smoothed particle hydrodynamics (SPH) is a method for simulating the dynamic behaviour of a fluid by treating it as a set of particles [95]. However, in the case of SPH, each particle is used as an interpolation point from which the fluid properties are calculated. This differs from the DPD method as where each particle has fixed physical properties. In SPH the particles are points which move with the flow, however the physical properties of these points are determined by interpolation based on kernel estimations. More formally, the interpolation of some quantity  $A$  at point  $\mathbf{r}$  is given by the integral interpolant

$$A(\mathbf{r}) = \int A(\mathbf{r}') W(\mathbf{r} - \mathbf{r}', h) d\mathbf{r}', \quad (2.8)$$

where  $W$  is the kernel function which depends on the distance  $|\mathbf{r} - \mathbf{r}'|$  and the smoothing distance  $h$ , and  $d\mathbf{r}'$  is a differential volume element. Furthermore, the kernel function must tend to the delta function as  $h$  approaches 0 and the integral over  $W$  must be normalised to 1 in order to ensure that constants are interpolated exactly.

For example, a kernel estimation can be used to determine the density of particle  $a$  at point  $\mathbf{r}$  as

$$\rho_a(\mathbf{r}) = \sum_b m_b W(\mathbf{r} - \mathbf{r}_b, h), \quad (2.9)$$

where the mass of surrounding particles  $m_b$  is smoothed to produce an estimated density  $\rho(\mathbf{r})$  at the given point  $\mathbf{r}$ . Furthermore, in order to solve the NSE and continuity equations that describe the flow of Newtonian fluids it is necessary to calculate the spatial derivative of various physical quantities such as pressure and velocity. Consequently, the kernel function must also be differentiable. If the kernel functions meet these criteria, the SPH formalism allows us to rewrite the continuity equation as

$$\frac{d\rho_a}{dt} = \sum_b m_b \mathbf{v}_{ab} \cdot \nabla_a W_{ab}. \quad (2.10)$$

Similarly, the terms relating to pressure and viscosity on the r.h.s of the NSE, see equation 1.1, can be discretised and rewritten as

$$-\nabla p_a = - \sum_b m_b \frac{p_a + p_b}{2p_b} \nabla W(\mathbf{r}_a - \mathbf{r}_b, h) \quad (2.11)$$

$$\eta \nabla^2 \mathbf{v}_a = \eta \sum_b m_b \frac{\mathbf{v}_a + \mathbf{v}_b}{p_b} \nabla^2 W(\mathbf{r}_a - \mathbf{r}_b, h), \quad (2.12)$$

where the pressure and viscous interactions are written in a symmetric form such that the forces applied on particle  $a$  by particle  $b$  and vice versa are equal and opposite.

### 2.1.3 Smoothed Dissipative Particle Dynamics

As it's name suggests, the smoothed dissipative particle dynamics (SDPD) method shares features from the SPH method and the DPD method. Whilst DPD effectively includes thermal fluctuations and dissipative behaviour, giving the model fluid a well-defined thermal equilibrium state, it is hard to gain any intuition about the properties of a DPD fluid from the model parameters alone. Instead simulations and measurements must be performed in order to ascertain the fluid viscosity and equations of state which correspond to the set of DPD model parameters. In contrast to DPD, the SPH method is based on the NSE and as a result the fluid viscosity and equations of state are direct inputs in the model.

SDPD improves upon DPD by using the force scheme used in SPH. However, one failing of the original SDPD method is its violation of conservation of angular momentum caused by force components acting perpendicular to inter-particle axes. Recent simulations using MPC have demonstrated the importance of angular momentum for

correctly describing the dynamics of two fluid phases (i.e. the boundary between intra- and extra-cellular fluid at the RBC membrane)] [96, 117]. This problem has been addressed in an extension of the original work, giving particles a spin and moment of inertia, such that angular momentum can be addressed and ultimately conserved [96].

The angular momentum conserving version of SDPD describes  $N$  particles with mass  $m_i$ , moment of inertia  $I_i$ , position  $\mathbf{r}_i$ , translational velocity  $\mathbf{v}_i$ , and rotational velocity  $\boldsymbol{\omega}_i$ . In a similar process to that described for SPH, the spin inclusive version of the NSE can be discretised to arrive at a set of pairwise forces which describe the interactions between particles. The force components consist of conservative  $\mathbf{F}^C$ , dissipative  $\mathbf{F}^D$ , rotational  $\mathbf{F}^R$ , and stochastic  $\mathbf{F}^S$  elements:

$$\mathbf{F}_{ij}^C = \left( \frac{p_i}{\rho_i^2} + \frac{p_j}{\rho_j^2} \right) w_{ij} \mathbf{r}_{ij}, \quad (2.13)$$

$$\mathbf{F}_{ij}^D = -\gamma_{ij} \left( \mathbf{v}_{ij} + \frac{(\mathbf{v}_{ij} \cdot \hat{\mathbf{r}}_{ij}) \hat{\mathbf{r}}_{ij}}{3} \right) + \frac{2\gamma_{ij}}{3} (\mathbf{v}_{ij} \cdot \hat{\mathbf{r}}_{ij}) \hat{\mathbf{r}}_{ij}, \quad (2.14)$$

$$\mathbf{F}_{ij}^R = -\gamma_{ij} \frac{\mathbf{r}_{ij}}{2} \times (\boldsymbol{\omega}_i + \boldsymbol{\omega}_j), \quad (2.15)$$

$$\mathbf{F}_{ij}^S = \sigma_{ij} \left( d\bar{\mathbf{W}}_{ij}^s + \frac{1}{3} \text{tr} [d\mathbf{W}_{ij}] \mathbb{1} \right) \cdot \frac{\hat{\mathbf{r}}_{ij}}{dt}, \quad (2.16)$$

where  $p_i$  and  $p_j$  are local particle pressures,  $\rho_i$  and  $\rho_j$  are local particles densities,  $\gamma_{ij}$  is the friction coefficient, and  $\sigma_{ij}$  is the random force coefficient. The local pressures are calculated from the equation of state

$$p_i = p_0 \left( \frac{\rho_i}{\rho_0} \right)^\alpha - b, \quad (2.17)$$

and the density of particles is calculated locally as

$$\rho_i = \sum_j W_L(\mathbf{r}_{ij}), \quad (2.18)$$

where the Lucy function  $W_L(\mathbf{r}_{ij})$  is used for smoothing over a cut-off radius  $r_c$ :

$$W_L(|\mathbf{r}|) = \frac{105}{16\pi r_c^3} \left( 1 + \frac{3|\mathbf{r}|}{r_c} \right) \left( 1 - \frac{|\mathbf{r}|}{r_c} \right)^3. \quad (2.19)$$

The weight function  $w_{ij} = w(\mathbf{r}_{ij})$  used for conservative interactions in equation 2.13 is defined as  $\nabla W_L(\mathbf{r}_{ij}) = -\mathbf{r}_{ij} w(\mathbf{r}_{ij})$ , and the friction and stochastic coefficients are taken to be

$$\gamma_{ij} = \frac{20\eta_0}{7} \frac{w_{ij}}{\rho_i \rho_j}, \quad (2.20)$$

$$\sigma_{ij} = 2\sqrt{k_B T \gamma_{ij}}. \quad (2.21)$$

Finally the terms in the stochastic equation 2.16,  $\text{tr} [d\mathbf{W}_{ij}]$  and  $d\bar{\mathbf{W}}_{ij}^s$ , refer to the trace of a random matrix of independent Wiener increments  $d\mathbf{W}_{ij}$  and its traceless symmetric component [96].

### 2.1.4 Numerical Integration and Boundary Conditions

Fluid described by DPD or SDPD particles evolves over time in accordance with Newton's second law of motion. The time evolution of the  $i^{\text{th}}$  particle's position, translational velocity, and rotational velocity are given by

$$\dot{\mathbf{r}}_i = \mathbf{v}_i, \quad \dot{\mathbf{v}}_i = \frac{1}{m_i} \sum_j \mathbf{F}_{ij}, \quad \dot{\boldsymbol{\omega}}_i = \frac{1}{I_i} \sum_j \mathbf{N}_{ij}, \quad (2.22)$$

where  $\mathbf{N}_{ij} = 1/2\mathbf{r}_{ij}\mathbf{F}_{ij}$  is the torque exerted between particles  $i$  and  $j$ , and is only relevant for SDPD particles with moments of inertia. The equations in 2.22 are integrated numerically using the velocity-Verlet algorithm,

$$\mathbf{r}_i(t + dt) = \mathbf{r}_i(t) + \mathbf{v}_i(t)dt + \frac{1}{2}\mathbf{f}_i(t)dt^2, \quad (2.23)$$

$$\tilde{\mathbf{v}}_i(t + dt) = \mathbf{v}_i(t) + \frac{1}{2}\mathbf{f}_i(t)dt, \quad (2.24)$$

$$\mathbf{f}_i(t + dt) = \mathbf{f}_i(\mathbf{r}_i(t + dt), \tilde{\mathbf{v}}_i(t + dt)), \quad (2.25)$$

$$\mathbf{v}_i(t + dt) = \mathbf{v}_i(t) + \frac{1}{2}(\mathbf{f}_i(t) + \mathbf{f}_i(t + dt)), \quad (2.26)$$

and the angular momentum is integrated in an analogous manner.

Fluid-wall interactions are important for simulating fluid flow in environments like microfluidic channels. In order to prevent fluid particles from penetrating walls, checks are made during the numerical integration of equations 2.22. Specifically, if the new position of a particle  $\mathbf{r}_i(t + dt)$  during the evaluation of 2.23 is found to cross into a prohibited region, particles are subject to a bounce-back reflection at the fluid-wall interface. During a bounce-back reflection, a particle's new position and velocity are given by

$$\mathbf{r}_i(t + dt) = \mathbf{r}_i(t) + \mathbf{v}_i(t)t' + \mathbf{v}_i(t + dt), \quad (2.27)$$

$$\mathbf{v}_i(t + dt) = 2\mathbf{v}_{BC}(t) - \mathbf{v}_i(t), \quad (2.28)$$

where  $t' = |\mathbf{r}_i - \mathbf{r}_{BC}| / |\mathbf{v}_{BC} - \mathbf{v}_i|$ , and  $\mathbf{r}_{BC}$  and  $\mathbf{v}_{BC}$  are the location of particle impact and the wall velocity, respectively. Note that bounce-back interactions are used (i.e. the normal and tangential velocity of the reflected particle are reversed), as opposed to specular reflections where only the normal velocity is reversed. Bounce-back reflections are preferred over specular reflections as they achieve a better approximation of no-slip boundary conditions.

In addition to particle reflections, correct fluid-wall particle interactions are ensured by placing a layer of frozen particles behind the impermeable barrier which share the same equilibrium structure as the fluid particles. Without the presence of frozen

wall particles, artefacts could arise at boundaries due to the improper distributions of conservative forces and incorrect calculation of particle densities in equation 2.18.

Finally, to fully guarantee no-slip boundary conditions at fluid-wall interfaces, an adaptive tangential force  $f_t$  is applied to fluid particles within a distance  $r_c$ . This force acting on particles near wall is given by

$$f_t(\Delta h) = C_k(\Delta v_t) \left(1 - \frac{\Delta h}{r_c}\right)^4 \quad (2.29)$$

where  $\Delta h$  is the perpendicular distance from the particle to the wall,  $C_k$  is the adapted force iterated via  $C_{k+1} = C_k + \alpha_r \Delta v_t$  (with  $\alpha_r$  as the relaxation coefficient), and  $\Delta v_t = v_{BC} - v_{est}$  is the difference between the boundary velocity  $v_{BC}$  and the estimated fluid velocity  $v_{est}$ . After several iteration steps, the value of  $\Delta v_t$  tends towards 0 and the adaptive force  $f_t^k$  remains constant.

## 2.2 CELL MODELS

In order to simulate the transit of deformable particles through DLD devices, a cell model is required which accurately captures mechanical properties such as viscosity, elasticity, bending rigidity, and area/volume constraints. This work uses 2D simulations to demonstrate the differences between sorting rigid beads and deformable vesicles, hence we require a 2D model for rigid beads and RBCs. Subsequent to this initial analysis, 3D simulations are employed in order to gain quantitative predictions about RBC behaviour in DLD and a 3D RBC model is required. Continuum methods and network models are two typical approaches for modelling vesicles, the latter technique is employed throughout this work.

### 2.2.1 2D Rigid Bead and Red Blood Cell

Rigid circular particles and RBCs are modelled as bead-spring rings composed of  $N_p$  particles connected by  $N_s = N_p$  springs, as depicted in figure 2.2. The total potential energy of springs is calculated as

$$U_s = \sum_{j=1}^{N_s} \left[ \frac{k_B T l_m}{4 l_p} \frac{(3x_j^2 - 2x_j^3)}{(1 - x_j)} + \frac{k_p}{l_j} \right], \quad (2.30)$$

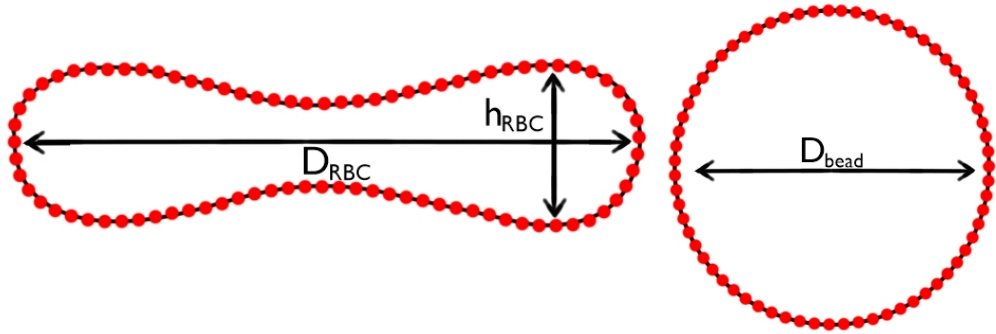
where  $l_j$  is the length of the  $j^{\text{th}}$  spring,  $l_m$  is the spring extension limit,  $x_j = l_j/l_m \in (0, 1)$ ,  $l_p$  is the persistence length, and  $k_p$  is the spring constant. The first component of equation 2.30 is an attractive potential from the worm-like chain polymer model

and the second acts as a repulsive potential. Equating the attractive and repulsive components of 2.30 relates  $l_p$  to  $k_p$  by

$$k_p = \frac{l_0}{l_p} k_B T \left( \frac{1}{4(1-x_0)^2} - \frac{1}{4} + x_0 \right), \quad (2.31)$$

with  $l_0 = x_0 l_m$  as the equilibrium spring length. Furthermore, the Young modulus of the springs is given by

$$Y = l_0 \left( \frac{\partial^2 U_s}{\partial l^2} \right) |_{l=l_0} = \frac{k_B T x_0}{l_p} \left( \frac{1}{2(1-x_0)^3} + 1 \right) + \frac{2k_p}{l_0^2}. \quad (2.32)$$



(a) 2D RBC model.

(b) 2D Rigid Sphere model.

Figure 2.2: (a) A depiction of the bead-spring model used to simulate an RBC in 2D. 2.2b a depiction of the same closed bead-spring chain model, but used to simulate a rigid spherical particle in 2D.

To model the effects of membrane bending rigidity, the bending potential is defined as

$$U_b = \sum_{j=1}^{N_p} k_b (1 - \cos(\theta_j)), \quad (2.33)$$

where  $k_b$  is the bending constant and  $\theta_j$  is the angle formed by the two adjacent springs which share the  $j^{\text{th}}$  particle. Additionally, an area constraint is imposed to represent retention and incompressibility of the cell interior:

$$U_{\text{area}} = \frac{k_a}{2} (A - A_0)^2, \quad (2.34)$$

where  $k_a$  is the area constraint coefficient,  $A$  is the instantaneous area, and  $A_0$  is the desired enclosed area. Careful tuning of the contour length  $L_0 = N_s l_0$ , bending constant  $k_b$  and equilibrium area  $A_0$  results in cells with different shapes and rigidities.



Choosing a diameter of  $D = L_0/\pi$  and a target area of  $A_0 = 1.04\pi \times (D/2)^2$  results in circular shaped non-deformable particle, and forms the basis for the 2D bead model. The non-deformability arises from high tension in the bead-spring ring as it tries to maintain the defined contour length  $L_0$  and simultaneously enclose an area 4% larger than that of a circle with circumference  $L_0$ . Alternatively, the RBC model is achieved by selecting a target area of  $A_0 = 0.46\pi \times (D/2)^2$ , which leads to a biconcave shape at equilibrium. The remaining parameters chosen for modelling beads and 2D RBCs are shown in table A.1 in appendix A.

### 2.2.2 3D Red Blood Cell

The 3D RBC membrane is modeled as a triangulated network of springs as seen in figure 2.3 [118–122]. A total of  $N_v$  particles constitute the mesh vertices and  $N_s = 3(N_v - 2)$  springs follow the edges of the mesh, reproducing the elasticity of the membrane ( $U_s$ ). A total of  $N_t = 2N_v - 4$  triangles make up the entire membrane surface and incident triangles have an associated potential energy ( $U_{\text{bend}}$ ) given by the angle between them, associated with membrane bending rigidity. Furthermore, local and global area constraints ( $U_{\text{area}}$ ) are enforced along with a global volume constraint ( $U_{\text{vol}}$ ). Formally, the total energy of a RBC membrane is given as

$$U_{\text{tot}} = U_s + U_b + U_{\text{area}} + U_{\text{vol}}. \quad (2.35)$$

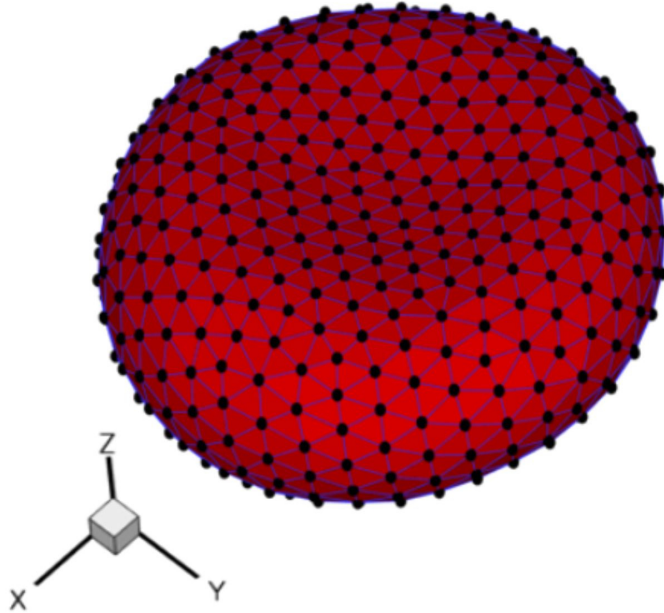


Figure 2.3: A RBC membrane modelled as a triangulated network of springs.

The total energy contribution of the springs is identical to that in the 2D model shown in equation 2.30. However, the equilibrium length of each spring  $l_{0j}$  is set in

accordance with an initial triangulated mesh of a stress-free biconcave RBC shape [121, 122].

The membrane bending rigidity in absence of spontaneous curvature is described by a bending energy identical in form to equation 2.33. Although, in the 3D case  $\theta_j$  refers to the instantaneous angle between the two triangles incident on edge  $j$ .

Finally, the area and volume constraints are accounted for by two potentials:

$$U_{\text{area}} = k_a \frac{(A - A_r)^2}{2A_r} + \sum_{j \in 1 \dots N_t} k_d \frac{(A_j - A_j^0)^2}{2A_j^0}, \quad (2.36)$$

$$U_{\text{vol}} = k_v \frac{(V - V_r)^2}{2V_r}, \quad (2.37)$$

where  $k_a$ ,  $k_d$ , and  $k_v$  are the global area, local area, and volume constraint coefficients, respectively.  $A$  is the instantaneous surface area of the membrane,  $A_j$  is the instantaneous area of the  $j^{\text{th}}$  triangle in the network, and  $V$  is the instantaneous RBC volume. The desired total surface area  $A_r$ , individual triangle area  $A_j^0$ , and interior volume  $V_r$  are set in accordance with the initial triangulation [121, 122].

The RBC model's variables are related to physical macroscopic properties of the RBC membrane by linear analysis for a regular hexagonal network [121, 122]. The membrane shear modulus is related to the spring parameters by

$$\mu_0 = \frac{\sqrt{3}k_B T}{4\zeta l_m x_0} \left( \frac{x_0}{2(1-x_0)^3} - \frac{1}{4(1-x_0)^2} + \frac{1}{4} \right) + \frac{3\sqrt{3}k_p}{4l_0^3}, \quad (2.38)$$

with  $x_0 = l_0/l_m$ . The area-compression  $K$  and Young's  $Y$  moduli are found as  $K = 2\mu_0 + k_a + k_d$  and  $Y = \frac{4K\mu_0}{K+\mu_0}$ . The Helfrich model is employed to describe the bending coefficient  $k_b$  in terms of macroscopic bending rigidity  $\kappa$ , yielding  $k_b = 2\kappa/\sqrt{3}$  [123]. The value of  $x_0$  is set to 2.2 for all springs [122]. The remaining model parameter values are found in table A.4 in appendix A.

### 2.2.3 Cell-Fluid Coupling

The cell models employed need to be coupled to fluid particles in order to investigate their behaviour in flow through DLD devices. The bead-spring and RBC network models are coupled to fluid flow via viscous friction between the  $N_v$  mesh vertices and local fluid particles. The viscous interaction is governed by the dissipative and random force components of the DPD method 2.1 [121]. No-slip boundary conditions at membrane vertices are enforced by careful selection of the friction parameter  $\gamma$  in the dissipative force equation 2.3. A fluid sheared over the effective surface of a membrane vertex exerts a friction force on the membrane given as  $\mathbf{F}_v = \int_{V_h} n g(r) \mathbf{F}^D dV$ , where  $n$  is the fluid number density,  $g(r)$  is the radial distribution function of fluid particles about

the membrane vertices, and  $V_h$  is the hemisphere volume of fluid situated above the vertex. Equating this integral to the total force required by a continuum hydrodynamical description leads to an expression for the calculation of  $\gamma$  [121]. In the 2D models, a chain segment of length  $L$  is considered instead of an area  $A$ , and particles within the area half circle are considered instead of the volume of a hemisphere. Finally, to prevent mixing between intra- and extra-cellular fluids, bounce-back reflections for the solvent particles are also introduced at cell membranes.



## EXPERIMENTAL TECHNIQUES

---

### 3.1 DETERMINISTIC LATERAL DISPLACEMENT

DLD devices consist of an array of micrometre scale obstacles which serve to divide the flow of fluid through a microfluidic channel into multiple well-defined parallel streams. It is possible to modify the width of flow streams by carefully tuning the geometry of the obstacle array, hence preventing particles above a critical size from residing within a stream when they are in close proximity to obstacles. As suspended particles traverse the DLD device, their trajectory is determined by their size relative to the obstacle array's critical size: Particles which are sufficiently small will follow the fluid flow direction and particles which are above the critical size will experience regular perturbations as they interact with obstacles, displacing them laterally with respect to the flow direction. These two modes of motion through devices allow for the continuous sorting of particles based on their effective size within the obstacle array and separated fractions of particles may be collected at the end of a device.

The functionality of DLD devices arises primarily from the successive shifting of rows of posts within the obstacle array. In order to understand the transit of particles through the obstacle array, it is first necessary to consider the nature of fluid flow through these shifted rows without the presence of particles. Once the flow field is well defined, the behaviour found for rigid spheres in DLD is considered, as it represents the simplest sorting case. Next, the behaviour of more exotic particles (such as RBCs) in row-shifted pillar arrays is discussed, along with the implications for DLD separation of deformable non-spherical particles.

#### 3.1.1 *Flow in Row-Shifted Arrays*

The geometry of a row-shifted pillar array is formally defined by three parameters; the post diameter  $D$ , the centre-to-centre spacing of posts  $\lambda$ , and the distance successive rows are shifted in the direction perpendicular to flow  $\Delta\lambda$ . A schematic of an obstacle array defined by these three parameters is shown in figure 3.1. Furthermore, each successive row of pillars is numbered, where row  $N + 1$  has the same lateral position as row 1 such that the obstacle array has a period of  $N$ . See figure 3.2a for a pillar array geometry with a period of  $N = 4$ .

By making a number of assumptions it is possible to arrive at an analytical prediction for the critical radius for which spherical particles of a smaller radius will follow

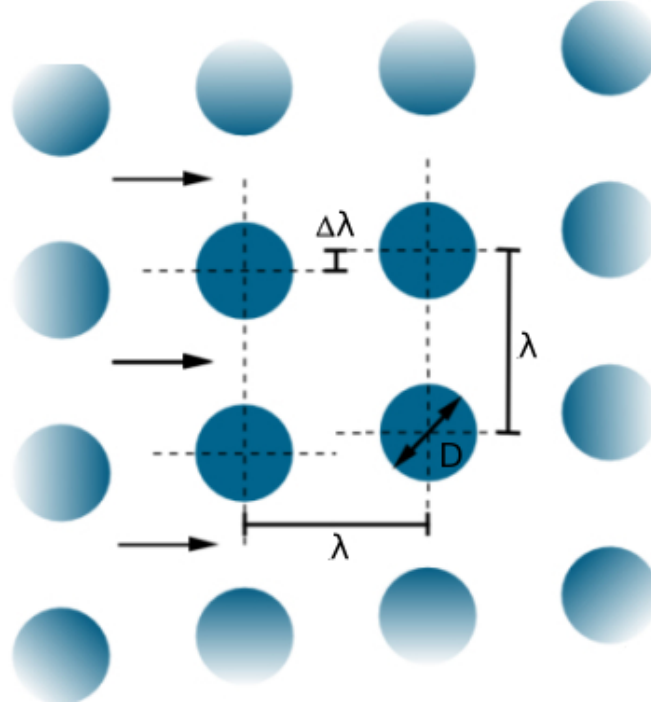


Figure 3.1: A schematic of a small section of the pillar array geometry in a DLD device, defined by post diameter  $D$ , post spacing  $\lambda$ , and the row-shift  $\Delta\lambda$

the fluid flow and particles of a larger radius will displace laterally. The two main assumptions are: The device is operated at a low Reynolds number  $Re \ll 1$  (laminar flow) and fluid flow between two posts adopts a parabolic velocity profile due to no-slip boundary conditions. Under these assumptions it is possible to divide the fluid into well-defined laminae, as is shown in figure 3.2a. The laminae carry an equal fluid volume, follow periodic paths through the obstacle array and have an average flow of zero in the lateral direction. The total fluid flux  $\phi_{\text{total}}$  can be expressed as a sum of the contributions of each laminae

$$\phi_{\text{total}} = \sum_i^N \phi_i. \quad (3.1)$$

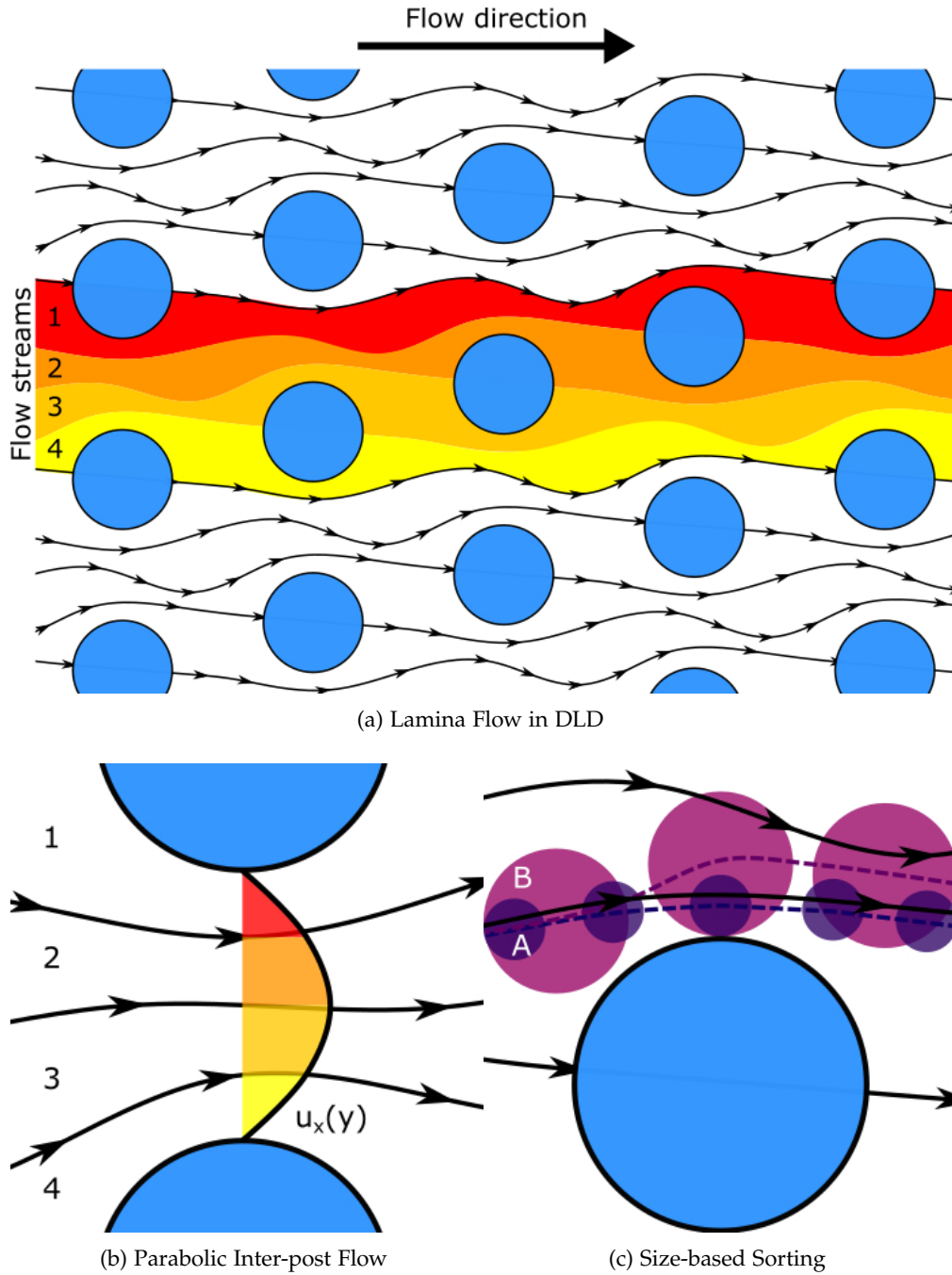


Figure 3.2: (a) Shows the division of the flow through an obstacle array into well-defined laminae. The obstacle array has a period of  $N = 4$  and hence the division is made into 4 equal lamina carrying equal fluid volumes with zero net flow in the lateral direction. (b) displays an approximately parabolic velocity profile of the flow between two pillars. Note, because the fluid flux carried through a cross section of each lamina is equal, and the velocity is greatest at the central point between the pillars, the lamina are widest near the pillar surface and thinnest at the channel center. (c) A depiction of two different sized particles, A and B. Both particles are initially placed in a lamina which would carry them under the next pillar. However, the larger particle is bumped laterally by the post into a neighbouring lamina. This key mechanism allows DLD devices to sort based on size.

Furthermore, figure 3.2b shows how the laminae travel fastest when in the channel center and slowest when near a post's surface. Consequently, each lamina must be widest when at a post-fluid interface and narrowest when in the channel centre in order to conserve its fluid flux. The width of the lamina flowing along the post-fluid interface  $W$  is of particular interest; it puts a size limit on particles the lamina can accommodate, else they are bumped into the neighbouring lamina by the pillar, as shown in figure 3.2c. By solving the following integral, it is possible to approximate a value for the width  $W$ :

$$\begin{aligned}\phi_1 &= \frac{1}{N}\phi_{\text{total}}, \\ \int_0^W u(y)dy &= \frac{1}{N} \int_0^G u(y)dy,\end{aligned}\tag{3.2}$$

where  $u(y)$  is the horizontal fluid flow velocity and  $G = \lambda - d$  is the gap between posts and  $d$  is the post diameter. If a parabolic flow profile is assumed,

$$u(y) = \left[ \frac{G^2}{4} - \left( y - \frac{G}{2} \right)^2 \right],\tag{3.3}$$

the integral 3.2 can be solved to find

$$W = \frac{d}{2} \left[ 1 + 2C + \frac{1}{2} \right],\tag{3.4}$$

where,

$$C^3 = \frac{1}{8} - \frac{1}{4N} \pm \sqrt{\frac{(1-N)}{16N^2}}.\tag{3.5}$$

If the array in question has a period of  $N > 10$  the approximation  $1/N = W/G$  holds, and the relation 3.4 is further simplified yielding

$$W \approx \sqrt{\frac{N}{3}} \cdot \frac{G}{N}.\tag{3.6}$$

This value gives a good approximation for the critical radius  $R_c \approx W$  of the obstacle array, and has been used for designing DLD devices [124, 125]. However, the aforementioned calculations also assume that particles have a negligible effect on the fluid flow field. This is of course untrue, so whilst  $W$  serves as a good approximation, it carries an innate degree of error.



### 3.1.2 Sorting by Size

Particles suspended within fluid flow in a DLD device are carried by viscous drag. In order to illustrate how two particles of different sizes might be separated, consider the laminae numbered 1 – 4 in figure 3.2a and the trajectory of two the particles (A and B), shown in figure 3.2c, with initial positions in lamina 4. Particle A has a radius  $R_A$  smaller than  $R_A < R_c$  and particle B has a radius  $R_B > R_c$ . Notice that particle A's hydrodynamic centre of mass remains within lamina 4 as it travels in the flow passed the post. However, due to steric interactions with the post, particle B's hydrodynamic centre of mass will be displaced into the above flow stream of lamina 3. Lamina 3 is the next to interface with a post and hence particle B will displace again into lamina 2, and so on, leading to the continuous lateral displacement of particle B as it traverses the device. This is in contrast to the trajectory of particle A, which follows the fluid flow unperturbed. The trajectory of particle A is referred to as the zig-zag mode as it appears to weave in and out of pillars, and the trajectory of particle B is referred to as the displacement mode, as it is laterally displaced by an amount  $\Delta\lambda$  with each post encounter.

In the design process of a typical DLD device, a user identifies two particles for separation and then selects an array geometry with a critical radius that falls in between the radii of the two particles. The previous sections showed an analytical prediction for the critical radius of a given array geometry in equation 3.6, however this fails to account for the flow perturbations caused by particles themselves. An alternative equation for the critical radius has been determined empirically by Davis *et al.* [7, 126],

$$R_c = 1.4 \cdot GN^{-0.48} \quad (3.7)$$

Figure 3.3 displays the transitions between the zig-zag mode and displacement mode for rigid beads of different size, and the dependence on post spacing and the period of the obstacle array. Generally, as the particle size decreases (or gap size increases) there is a transition from the displacement to the zig-zag mode. This transition occurs earlier for obstacle arrays with a smaller period, which intuitively makes sense because the width of the flow laminae  $W$  depends on  $N$ . Note, the parabolic flow profile prediction consistently underestimates the true critical radius shown through the empirically determined equation determined from experimentally observed values. Consequently, the majority of DLD devices are designed using the empirically determined equation 3.7 to tune devices' critical radii.

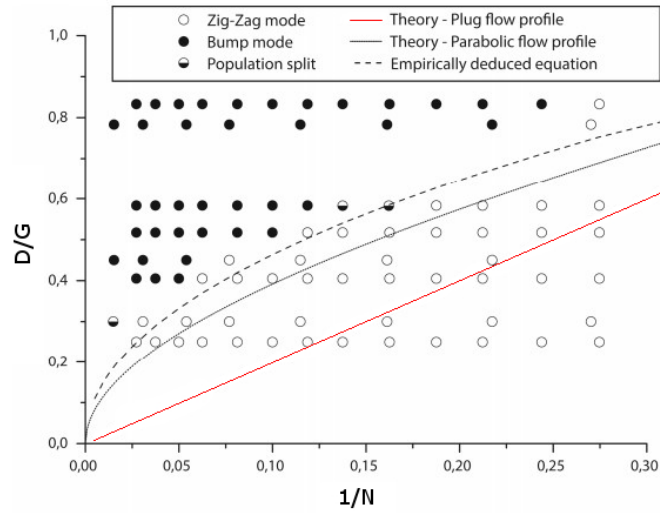


Figure 3.3: A comparison of experimental results vs. theoretical predictions. A graph showing the experimentally observed trajectory behaviour of beads with diameter  $D$  inside DLD obstacle arrays with geometries defined by their period  $N$  and gap size  $G$ . The empirically derived curve achieves the best agreement with experiment. The curve predicted by parabolic flow consistently yields an  $R_c$  smaller than the observed value due to its failure to account for flow disturbances caused by particles. Finally, predictions which assume plug-flow are completely incorrect due to the omission of no-slip boundaries. Graph and experimental data sourced from [126].

### 3.1.3 Non-spherical Deformable Particles

In many cases it is desirable to separate particles with more complex shape and mechanical properties than the rigid spherical bead. For instance, in clinical biology and diagnostics many bio-particles will be the focus of attention and only a small fraction of these will behave in the same way as a rigid sphere. RBCs are a good example of a particle which exhibit complex behaviour in flow and their trajectories through DLD devices will depend on far more variables than the critical radius defined solely by the devices geometry. The key properties can be divided into two categories: (i) Those that inherently belong to the cell such as shape and rigidity: (ii) Those that pertain to device geometry and operation (such as the flow speed and device depth), and can alter the behaviour of deformable non-spherical particles. Each of the key differences between non-spherical deformable particles and rigid beads in DLD devices are identified and discussed in this section.

#### *Aspect Ratio and Shape*

As previously stated, a particle's transit mode through a DLD device depends on whether its hydrodynamic centre of mass is ever pushed across flow laminae due to

steric interactions with posts. In the case of rigid spheres, it is easy to predict laminae crossing events, as the minimum distance between particles and post surfaces is independent of the orientation of particles. However, if you consider the case of any non-spherical particle, it is clear that the distance between it and the post surface will depend on its orientation. For instance, a discocyte's trajectory through an obstacle array will depend heavily on whether its principle axis is perpendicular or parallel to the device floor and ceiling. In addition to the instantaneous orientation of non-spherical particles, particle orientation is likely to change as they rotate due to shear forces found in the complex flow field of the obstacle array. Consequently, periodic rotational behaviour is expected to play an important role in sorting.

### *Deformation*

Many bio-particles are deformable and it is well established that velocity gradients in flow can exert shear stresses on suspended soft particles, causing them to deform [120]. In addition to deformation in flow, soft particles will also deform upon direct interaction with the posts. The exact nature of these deformations is very difficult to determine, as the shear stresses themselves depend on the nature of the flow field, which is in turn altered by disturbances from the particle. From a simplistic point of view, it is safe to claim that identically shaped and sized particles with different mechanical properties can undergo different transit modes through a DLD device.

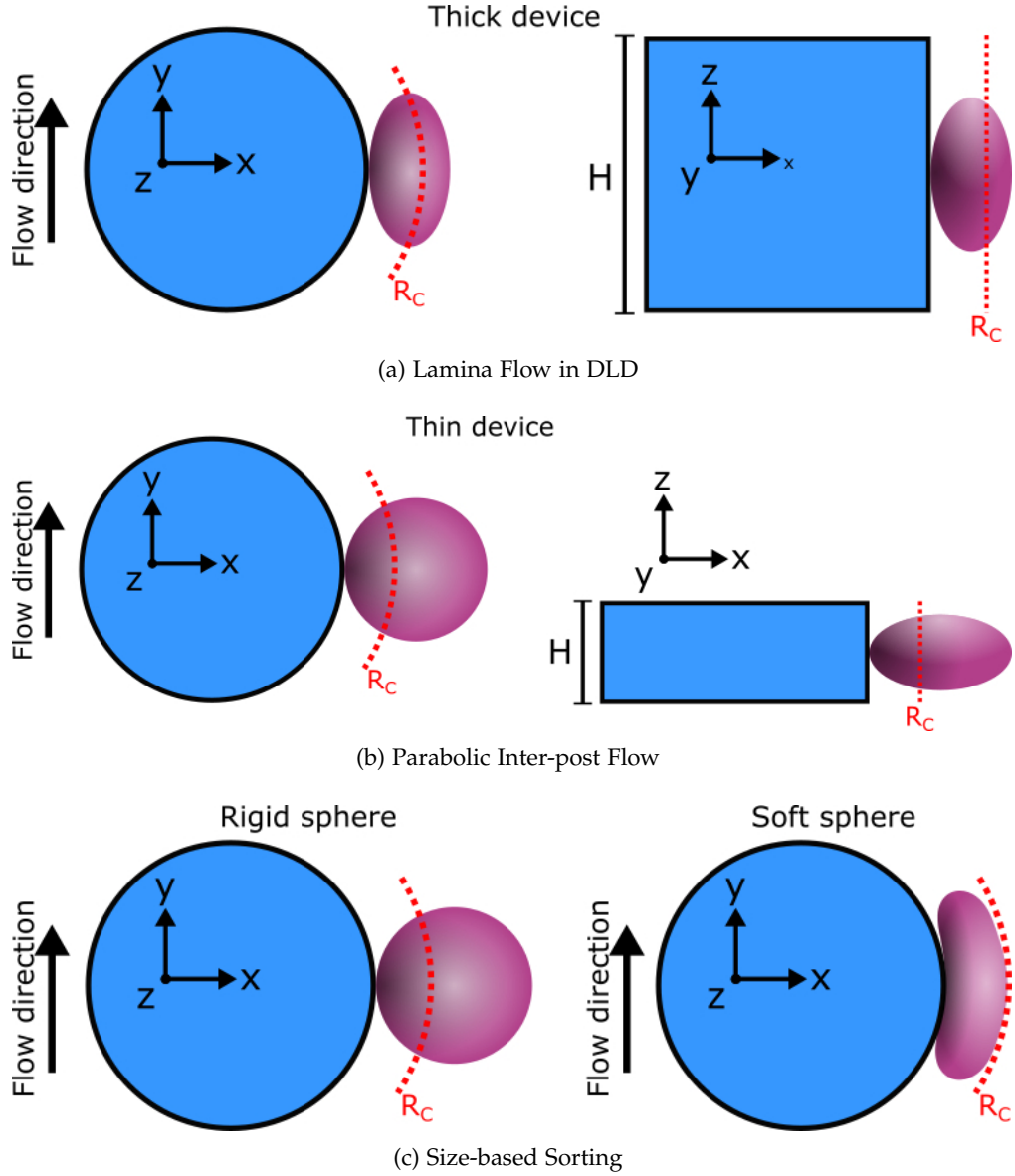


Figure 3.4: (a) A rigid disc shaped particle in a DLD device where the pillar height  $H$  is larger than the length of the particle's semi-major axis. (left) A view looking down onto the device. (right) A view looking down the device in the flow direction. The particle orientates itself such that the distance between the post surface and its hydrodynamic centre of mass is at a minimum. (b) A rigid disc shaped particle in a DLD device where the pillar height  $H$  is smaller than the length of the particle's semi-major axis. (left) a view looking down onto the device. (right) A view looking down device in direction of flow. In this case, the particle is unable to align with the pillar in a way to minimise its distance because it is physically constrained by the floor and ceiling of the device. (c) A depiction of the difference between a rigid (left) and deformable (right) spherical particle in a DLD device. The two particles' effective sizes in the device fall either side of the critical radius and consequently they would undergo different transit modes.

### *Dynamic Behaviour*

The additive effects of deformability and non-sphericity can result in many complex dynamic behaviours. For example, as discussed in the previous section, RBCs are known to exhibit a range of motions under different flow conditions and a tank-treading RBC's trajectory might be different from that of a rolling or tumbling RBC. Dynamic behaviour can be controlled to some extent by the device design and operation. Perhaps the simplest method is by altering the depth of the device; a sufficiently shallow device will limit the orientation of particles, essentially reducing the available degrees of freedom. A second method for controlling dynamics is by altering the flow speed itself. As previously discussed, velocity gradients in flow result in the deformation of particles, so any increase in the severity of these gradients will increase deformation or even push particles from one regime of dynamic behaviour into another. Finally, vesicle-type particles which are composed of a membrane enclosing an internal fluid experience shear stresses in flow which depend on the ratio between the suspending medium viscosity and the internal fluid viscosity. This phenomenon is well established for RBCs: under physiological conditions the inner fluid is approximately five times more viscous than the suspending plasma however if the viscosity of the suspending fluid is increased so they are equal, a dynamic behaviour emerges called tank-treading.

### *Diffusion*

As the separation in DLD devices is achieved by particles either remaining in one flow laminae or repeatedly crossing over into neighbouring laminae, it is important to ask whether diffusion is significant in a device. If a particle diffuses a distance equal to the difference between the device's critical radius and the particle radius  $d_{\text{diff}} \geq R_c - R_p$ , it would be possible for the particle to undergo transitions between the displacement and zig-zag modes. Whether the effects of diffusion are important or not can be determined from the Péclet number  $Pe = LU/D_{\text{diff}}$ , which is the ratio between the flow velocity  $U$ , characteristic length  $L$  and the mass diffusion coefficient  $D_{\text{diff}}$ . If the flow velocity and particle size are sufficiently large relative to the diffusion constant the Péclet number is high, and diffusion can be neglected. For the scenarios in this work, where all particles are micro-meter sized and the flow velocity is relatively high, the Péclet number is large and diffusion is not important. Indeed, for sub-micrometre particles, the effects of diffusion might become important and transitions between zig-zag and displacement mode trajectories would become blurred.

*Collective Behaviour*

Particles perturb the surrounding flow field and as a consequence their trajectories are slightly different from those predicted by a parabolic flow profile. In a similar way, if particle concentration is high enough, we can expect neighbouring particles to undergo hydrodynamic interactions. Furthermore, high concentrations of particles can also give rise to device clogging, resulting in a local change in critical size and alteration of the fluidic resistance of a device. Quantitatively understanding the effects particle-particle interactions is a complex problem and given that the behaviour of individual non-spherical soft particles is still poorly understood, it is first necessary to devote attention to the behaviour of individual particles. As such, all simulations in this work consider one single particle and all experimental data are refined to exclude particles which have come into close proximity with other particles. Only once the isolated behaviour for a particular particle is well understood does it make sense to analyse the behaviour of high concentrations of particles and describe the observations in terms of deviations from the single particle case.

*Implications for DLD sorting*

At a first glance, the vast number of parameters affecting the transit of non-spherical deformable particles in DLD devices seems a hindrance. When comparing the case of non-spherical deformable particles to that of rigid spheres, where the trajectory is solely dependent on the geometry of the device and the size of the particle, there is indeed an overwhelming number of factors which must be considered. However, the richness in behaviour allows for particle sorting based on factors other than size. For example, two particles which are identical in all aspects apart from their elastic properties will deform to a different degree in the same flow and would be expected to undergo different transit modes, allowing deformability based separation. Furthermore, two different shaped particles may or may not be distinguishable to a device depending on their orientation. By altering the depth of the device it would be possible to force certain orientations, making them adopt different transit modes. Finally, the dynamic behaviour of two cells which have different internal viscosities or elastic properties could be manipulated by altering the flow speed or viscosity of the suspending medium.

The obvious caveat of these more advanced sorting schemes is that every parameter must be carefully selected in order to achieve the desired separation and it is highly unlikely that there will be a simple model which can account for all of the competing effects of deformability, non-sphericity and dynamic behaviour in a given DLD array geometry. Consequently, device design becomes more complicated for non-spherical deformable particles. The theory for rigid spheres may be borrowed with some suc-

cess, for example if a deformable sphere is known to deform by a certain degree when at a ‘decision point’ in the DLD device, an effective radius of the particle can be taken instead of the rest radius. This effective radius can then be compared with the critical radius in order to determine whether the particle will travel under a zig-zag or displacement mode. However, this method becomes insufficient as soon as dynamic behaviour begins to play a role, as the model would need to predict the orientation of the particle, the degree of deformation and account for the hydrodynamic effects. A more reliable method of device design is to perform mesoscopic simulations for a specific separation scheme. If the mechanical properties of two particles are well known, it is then possible to perform numerous simulations at different flow speeds and device geometries in order to find the best candidates for separation.

### 3.2 EXPERIMENTAL PROCEDURE

This section discusses the process of DLD device design in light of the factors previously outlined and how simulations might be used to overcome problems with current design processes.

#### 3.2.1 *Device Design*

The functionality of a DLD device is not only dependent on the geometry of the obstacle array, the nature in which sample is introduced to and collected from the device is also of importance. A device with a single wide inlet can only be used to increase the concentration of larger particles from a population of smaller particles or vice-versa. In order to achieve explicit separation of two particle types, it is necessary for the particle flow to be focused such that there is vacant buffer into which particles can move. This principle is demonstrated in figure 3.5 and is best achieved by introducing multiple inlets for the sample and buffer. Furthermore, the selectivity of an obstacle array is limited by the number of outlets into which the separated particles can be extracted.

In the case of hard rigid spheres, one can approach the problem of device design by appealing directly to the empirical equation relating array geometry to a critical radius [7]. However, due to the complications which arise for deformable non-spherical particles, this approach is significantly less accurate and it may be necessary for a device to go through numerous iterations of design before it is performing as desired. Instead we propose an initial simulation step in device design which could reduce time and resources spent in fine-tuning and calibrating devices in the lab. Furthermore, a reliable simulation technique would allow for the investigation of novel sorting schemes which focus on things such as the dynamic properties of cells. However, as far as we are aware, simulations are yet to provide quantitative predictions for the behaviour of non-spherical soft particles in DLD devices. This work intends to make the first steps in

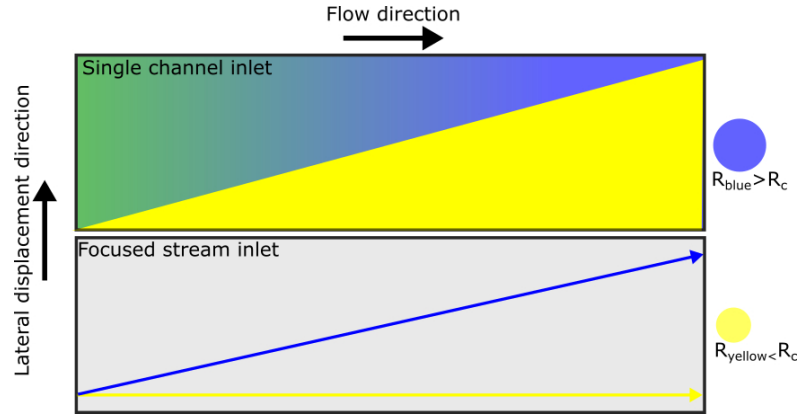


Figure 3.5: Examples of a DLD channel being used for concentrating or separating particles depending on whether the particle sample is introduced to the device via a focused stream or broad inlet equal in width to that of the device. (top) a mixture of large blue particles and small yellow particles enter the DLD channel in an unfocused stream. The blue particles travel in the displacement mode as they are larger than the critical size and the smaller yellow particles travel with the direction of flow in a zig-zag mode. Consequently the blue particles are concentrated in the top of the device and the yellow particles are left in a broad distribution across the width of the channel. (bottom) The particle mixture enters the device in a focused stream, meaning that the blue particles are displaced into empty buffer. In this case both particles can be collected at the end of the device, whereas in the single channel inlet example only an enriched sample of blue particles can be collected.

realising accurate simulations of particle behaviour in DLD devices which could in turn be used to make informed designs for devices intended to sort specific particles. As such, all experimental devices are chosen such that they span a large variation in obstacle array geometries, to increase the volume of experimental data available for comparison with simulations.

Chirped DLD devices are typically used to separate multiple particles types into many fractions. A schematic of a chirped DLD device composed of a series of  $n = 13$  pillar arrays with different critical radii can be seen in figure 3.6. This means that a device with  $n$  arrays is able to separate a mixture of particles into  $n + 1$  distinct fractions based on their size. A chirped device may also be used to determine the array geometry at which a certain particle undergoes the transition from the displacement mode to the zig-zag mode. This is useful for non-spherical deformable particles because they do not have a well-defined radius to compare to the critical radius of the obstacle array [8]. By performing simulations for different particles and obstacle array geometries which match those of the chirped DLD device, we hope to see the transition from displacement to zig-zag mode occur in the same array geometry. Good agreement would vindicate the simulation method and motivate further simulations which would in turn be used to design more specialised devices.



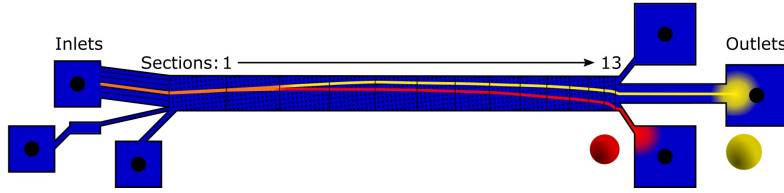


Figure 3.6: A schematic for a chirped DLD device initially developed by Holm *et al.* [8], with  $n = 13$  successive sections, each with larger critical radii  $R_{c1} < R_{c2} < \dots < R_{c13}$ . The smaller red particle undergoes an early transition from displacement to zig-zag mode, whilst the larger yellow particle transitions in a later section of the device. Additionally, both particles are hypothetically free to migrate in a negative lateral direction, which would not be possible if the sample was injected via the lower inlet.

The experimental data used in this work is used solely for comparison with simulation results, hence the manner in which devices are used is different from a typical set-up for cell sorting. Firstly, a chirped device is normally used with a focused stream of particles, allowing for the collection of different particle populations at the end of the device. However, the locations where particles exit the device are a result of their trajectory and the section of the device in which it switched from the displacement mode to the zig-zag mode. As such, videos of each section of the device must be recorded and analysed in order to realise the type of the transit mode present in each section of the device. Furthermore, instead of inserting particles in a focused stream at the edge of the device, it is more revealing for particles to be introduced via a single wide inlet as it reduces the initial concentration of particles and the likelihood of particle-particle interactions. Depositing particles in the centre of the device channel also allows for particles to undergo negative zig-zag modes, a motion which is unlikely but should not be excluded as no such limitations will be present in the simulations.

### 3.2.2 Device Fabrication

There are many ways of making microfluidic devices, materials include glass, silicon or polymers and fabrication can employ injection moulding or lithography, amongst other techniques. The DLD devices used throughout this study were made out of polydimethylsiloxane (PDMS) and created by replica moulding. A relief pattern of the DLD design is created in a robust material which can be used as a master for moulding the device out of PDMS. Liquid PDMS poured over the master is cured and removed from the mould. In order to seal off the DLD device, it and a flat glass sheet are treated with oxygen plasma and then bonded together [72].

### 3.2.3 *Data Collection and Analysis*

DLD devices are generally used to sort heterogeneous populations of particles, as such, a typical user's primary concern is the exit locations of certain particle types from a device. A detailed description of the distribution of particles as they exit the main flow channel allows the user to collect the desired particles at different outlets of the device. However, in the stage of device design and optimization, as is the case with this work, a detailed picture of what is happening to particles as they undergo transit through DLD devices is necessary: Not only is there a need to know where particles exit a device but it is important to understand how the particle got there. For hard rigid spherical particles, there are only two permitted modes of motion so the lateral exit location alone is sufficient information to deduce which mode of motion the particle adopted in the device. However, deformable and anisotropic particles may have many transit modes available, so such deductions are not possible. Furthermore, chirped DLD devices have different sections, each with different geometries, and in order to optimize such a device it is necessary to know the particle behaviour specific to each section. By observing transitions between transit modes as particles move between different array geometries, it is possible to understand what mechanical processes are responsible. Finally, given that the focus of this work is to demonstrate the importance and relevance of simulation techniques in microfluidic device design, we wish to perform detailed comparisons between the particle trajectories and dynamic behaviours predicted by simulation with those observed in an experimental setting. This section explains the methods used to obtain detailed information on particle transit in DLD devices and the analysis applied thereafter.

#### *Data Collection*

Recordings are taken of RBCs in transit through each section of the chirped DLD devices. Low magnifications of  $10 - 20\times$  allows the simultaneous observation of multiple particles as they migrate across the entirety of sections. However, at these low magnifications, RBCs are poorly resolved and their dynamic behaviour is unobservable. For this reason, videos that track individual RBCs as they traverse the device are taken at higher magnifications of  $40 - 60\times$ , these recordings allow direct observation of RBC deformation and dynamic behaviour.

#### *Trajectory Extraction*

In order to perform a quantitative comparison with simulation results, individual particle trajectories must be extracted from the videos as raw data. The method for extracting the raw data is outlined in figure 3.7. The first step removes all background

information from each frame of the video, this is achieved by projecting every frame of a video onto one single image, taking the median value for each pixel, subtracting this median projection from each frame leaves only the pixels which are unique to that frame. After the background subtraction is complete, the contrast is enhanced, as it increases the efficiency of the particle-tracking algorithm. The processed video is analysed using the MOSAIC particle tracking suite in the image processing application ImageJ, where each frame is checked independently for particle like objects and the results for neighbouring frames are compared in order to stitch together the particle locations, forming particle trajectories.

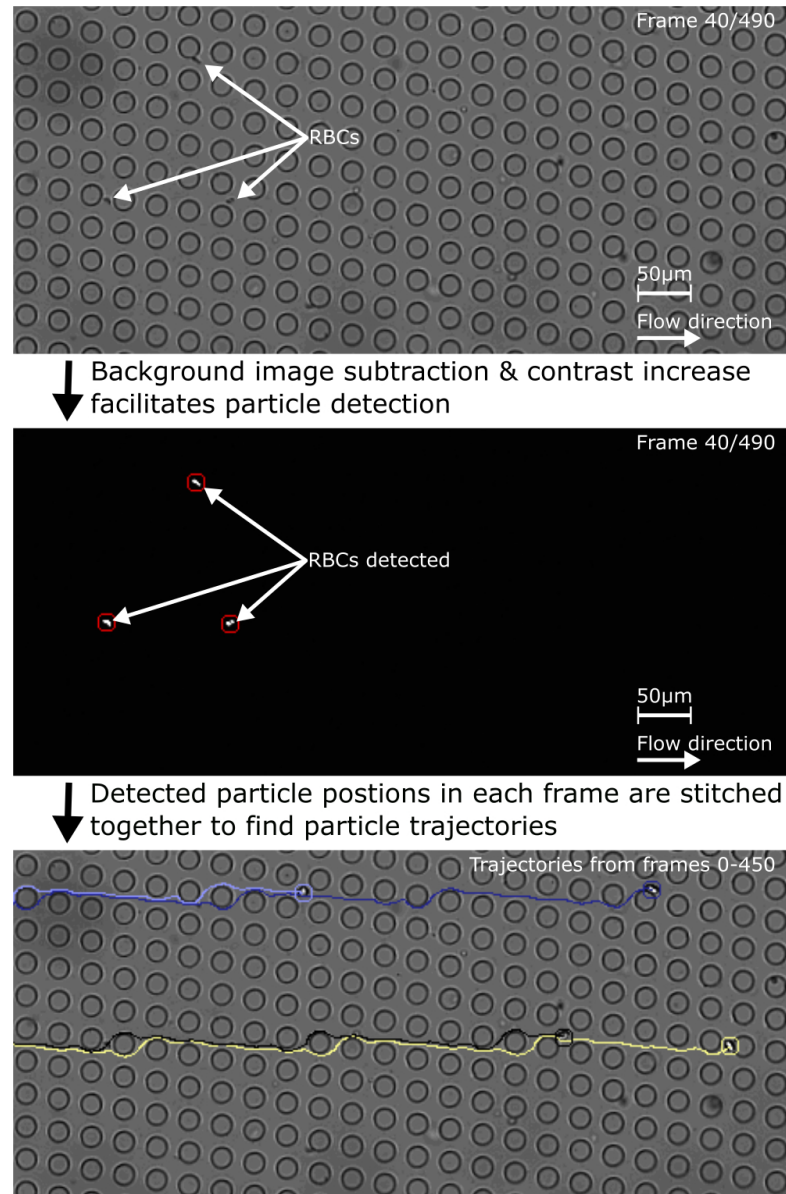


Figure 3.7: The step-by-step process of extracting particle trajectories from 450 frames of a video recording of a DLD obstacle array. (top) Three RBCs are observable in frame 40, however they are undetected by the tracking algorithm due to obfuscation by the pillar array. (middle) subtracting a median image of the 450 frames from each image removes the background and leaves detectable RBCs. (bottom) The positions of the particles detected in neighbouring frames are compared to identify the total trajectories.

### *Trajectory Analysis*

After the particle tracking stage, the trajectory of each detected particle is now available in terms of its position with respect to time  $\mathbf{r}(t)$ . A comprehensive post processing screening stage is carried out to ensure the experimental data is suitable for comparison

with simulated data. Firstly, some trajectories are too short, and consequently need to be disregarded, this can be attributed to the recordings starting after the particle has entered the frame (or ending before the particle has exited the frame) or the particle being stuck in the device. Secondly, the trajectories of particles which interact with other particles are removed. This data screening is formed because the simulated case only ever considers one isolated particle and it is clear that particle-particle interactions could alter particle trajectories.

Following the screening process, all trajectories from each obstacle array geometry are cross-examined in order to establish a general pattern for particle transit in each section of the device. In many cases there can be hundreds of trajectories for one section and it is inefficient to compare trajectories directly by eye. Instead an algorithm is employed to compare trajectories. The algorithm employed borrows many ideas used in image recognition, principally, the concept of identifying a specific pattern and then searching for similar patterns in a second image [127]. This technique requires a means by which the image similarity can be evaluated numerically, one such method is minimization of a value called the Hausdorff distance  $d_H$ .

The Hausdorff distance between two images (A and B) is defined as the largest possible distance from a point in the first image to the closest point in a second image, that is to say, every other point in image 1 is at a distance  $d < d_H(A, B)$  from another point in image 2. Formally this can be defined as

$$d_H(A, B) = \max\left\{ \sup_{a \in A} \inf_{b \in B} d(a, b), \sup_{b \in B} \inf_{a \in A} d(a, b) \right\}, \quad (3.8)$$

where  $\sup$  denotes the supremum and  $\inf$  the infimum of the distances between points in image A and B. Figure 3.8 depicts  $d_H(A, B)$  for two sets of points, where A and B are points sets found on the edge of two similar shapes. This picture is analogous to the case of two particle trajectories, each defined by a series of particle positions. The hausdorff distance between two sets of points is minimised by performing many spatial translations on one set while keeping the other set stationary. The translation which achieves the lowest  $d_H$  is then evaluated and if  $d_H$  is below some threshold value then a match between the two images is confirmed. Figure 3.9 shows the trajectory alignment of particles whose extraction is demonstrated in figure 3.7. These trajectories in graph 3.9a were cross examined and their  $d_H$  values minimized in order to achieve alignment. Figure 3.9b shows trajectory plots after alignment in addition to a general trajectory which represents the average of the aligned trajectories. This single averaged trajectory provides a suitable way to compare the observed experimental behaviour within a section with the trajectory predicted by simulations.

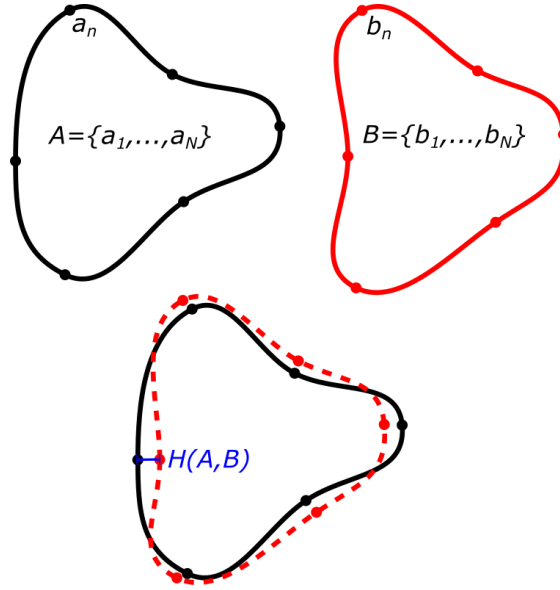
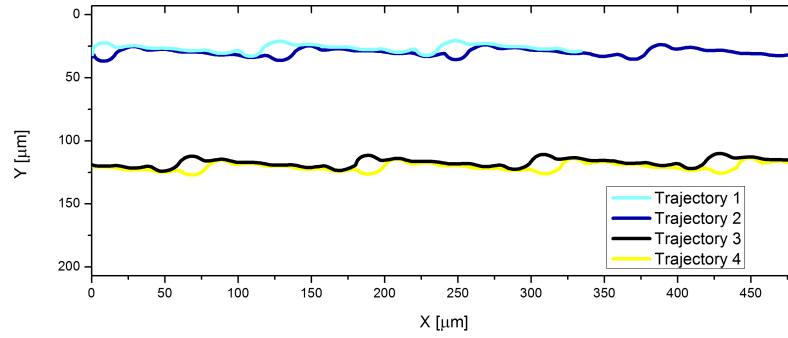
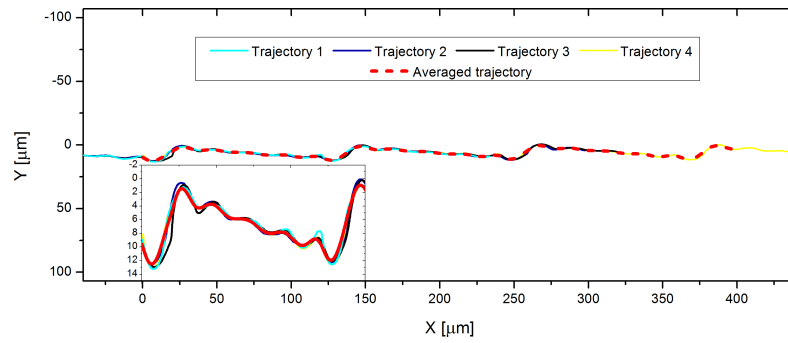


Figure 3.8: Depiction of the minimum Hausdorff distance obtainable between two point sets  $A = \{a_1, \dots, a_N\}$  and  $B = \{b_1, \dots, b_M\}$  which define two similar shapes. Note that once  $d_H$  has been minimized all points are a distance  $d \leq d_H(A, B)$  from a point in the opposite shape's point set.



(a) Particle Trajectories.



(b) Aligned Trajectories.

Figure 3.9: (a) A plot of the 4 trajectories extracted in the 450 frames depicted in figure 3.7. (b) A plot of the same trajectories after they have been spatially translated in order to minimise  $d_H$ . The dotted red line represents the average trajectory of this particle type (RBCs) in the given DLD geometry.

## SORTING RIGID AND DEFORMABLE PARTICLES IN DLD: A 2D SIMULATION APPROACH

---

### 4.1 INTRODUCTION

In this chapter, the DPD fluid model introduced in section 2.1.1 and the two-dimensional bead-spring model from section 2.2.1 are employed to simulate the transit of rigid spheres and RBCs through micro-pillar obstacle arrays in DLD devices. These coarse grained techniques are particularly well suited to simulating processes in microfluidics as they sacrifice the atomistic level of detail available with MD to facilitate the much longer length/time scales relevant in soft matter systems. Additionally, simulations are carried out in two dimensions. 2D treatment allows for much faster computational times and allows for a systematic exploration of a wider parameter space. However, 2D simulations require a level of caution as fluid flow and cell deformations and dynamics in microfluidics are intrinsically three-dimensional. With this said, numerous studies of RBCs in microchannels [103, 128] and WBCs in blood flow [129] demonstrate that the behaviour of deformable particles in 3D can be reproduced qualitatively using 2D simulations. Hence, the 2D picture should capture essential physics behind particle separation and is expected to provide valuable insight into particle motion in DLD devices.

As an initial proof of concept, simulation results for hard spherical particles in circular-pillar arrays are compared with experimental results for the same geometries. Comparison shows that 2D simulations achieve near quantitative agreement with experiment, which is a non-trivial result as the flow fields around circular obstacles and particles are appreciably different from those induced by spherical particles and cylindrical posts. Subsequently, RBC transit through the same geometries is simulated in order to investigate how deformable anisotropic particles behave differently compared to rigid spherical particles. The results show there is a clear dependence on the deformation of cells and the dynamic behaviour they undergo in the micro-channel, which is in agreement with findings found in different micro-scale geometries. Consequently, sorting based on the characteristic critical radius of an obstacle array is not valid for deformable, non-spherical particles. Instead, the particle transit depends on additional factors such as flow rate and cell-mechanical properties, significantly complicating the design of sorting devices. However, with the increase in complexity comes new opportunities for more elaborate sorting schemes able to sort cells that would otherwise be inseparable using design principles developed for hard spherical particles.

## 4.2 SIMULATION SETUP

The DLD mechanism is simulated in 2D using a single circular obstacle and a lone suspended particle within the computational domain. The repetition of the device geometry is represented using periodic boundary conditions in both the flow (x) and row-shift (y) directions. The periodic boundary in the x direction imposes a lateral shift on particles in the y after boundary-crossing events, this mimics the lateral shift  $\Delta\lambda$  between successive pillar rows. In all simulations the post diameter  $d = 15\mu\text{m}$ . No-slip boundary conditions are imposed at the fluid-post interface, as described in section 2.1.4; with a layer of frozen particles within the pillar wall, bounce-back reflections at the fluid-pillar interface, and a tangential adaptive shear force applied to particles within a near-wall layer.

The fluid flow is driven by a force applied to each fluid particle, and can be tuned to achieve different flow rates. Furthermore, the lateral shift imposed on particles at the x-boundary condition induces a non-zero net flow in the y direction. However, real DLD devices have channel limits and net flow in the y direction is prohibited by the device's side walls. Consequently, a corrective force is applied to particles perpendicular to the fluid flow in simulations, ensuring zero net flow in the y direction. The magnitude of the corrective force is determined by calculating the fluid flux across the y boundary and adapting the force iteratively until flux converges to zero.

The simulation parameters are related to physical parameters via characteristic length and time scales. In simulations for rigid particles, the fluid viscosity is used to define a time scale but in Stoke's flow, different flow profiles can be scaled linearly. Consequently time scaling is not crucial for rigid particles. Conversely, RBCs in different flow rates experience different degrees of cell deformation and a time scale must be defined. In this case, the characteristic RBC relaxation time is used

$$\tau = \frac{\eta D_{\text{RBC}}^3}{\kappa}, \quad (4.1)$$

where  $D_{\text{RBC}}$  is the RBC diameter,  $\eta$  is the suspending fluid viscosity, and  $\kappa$  is the bending rigidity coefficient. This time scaling can relate the simulation parameters to physical parameters, for instance a healthy RBC has values  $D_{\text{RBC}} \approx 7.5\mu\text{m}$ ,  $\kappa = 50 - 70k_{\text{B}}T$  at body temperature, and blood plasma has a viscosity of  $\eta \approx 1.2 \times 10^{-3}\text{Pas}$ .



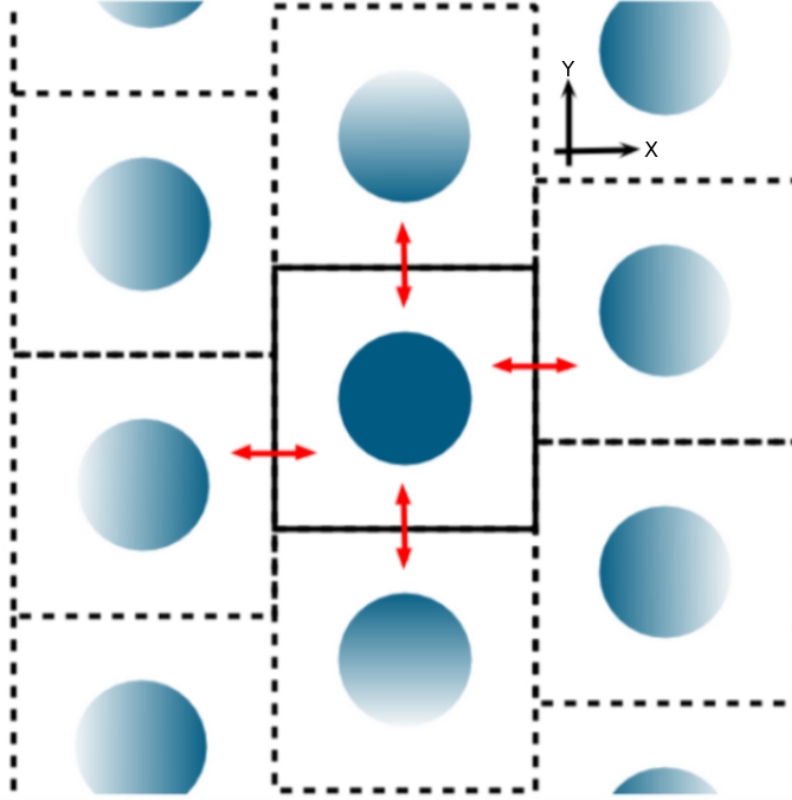


Figure 4.1: DLD array with circular posts. The geometry is defined by the post center-to-center distance  $\lambda = 25 \mu\text{m}$ , the post gap  $G = 10 \mu\text{m}$ , and the row shift  $\Delta\lambda$ . The red arrows indicate the direction of entry and exit of particles across the periodic boundary conditions, note the shift in lateral position for particles crossing the vertical boundaries. Figure source with permission from /citehenry2016sorting.

#### 4.3 RESULTS

The motion of rigid spherical particles flowing through circular obstacle arrays can be divided into two types; the zigzag and displacement modes. The transport mode adopted is dependant on the particle size relative to the array's critical size [6, 7], which at present is best predicted by the empiric formula 3.7 found from systematic experimentation of polystyrene bead transit in different circular-post array geometries. This equation can be re-written in terms of the row-shift fraction  $\epsilon = \Delta\lambda/\lambda = 1/N$  and rearranged to give a critical radius normalized by the obstacle array gap size  $G$

$$\frac{D_C}{G} = 1.4\epsilon^{0.48}. \quad (4.2)$$

This gives a more general equation for comparing experimental and numerical data, as it depends on the ratio between gap size and particle size.

#### 4.3.1 Rigid Spheres in DLD Obstacle Arrays

Before the exploration of a more complex geometries, different post shapes, and particle deformation, careful testing and validation of the simulation technique is essential. Hence, initial 2D mesoscopic simulations compare the trajectories of simulated rigid spheres with the behaviour predicted by equation 4.2. This is followed by an investigation of the effects of post shape on the separation of spherical and non-spherical particles.

##### *Circular Pillars*

To test the effectiveness of 2D simulations, the separation of 7 different sized rigid spherical particles ( $D_{sp} \in [2.78 - 5.59]\mu\text{m}$ ) in circular post arrays is investigated. The simulation results are then compared with predictions made from equation 4.2, which is empirically obtained and hence represents a comparison experimental results. Several array geometries are considered, spanning a range of different row shifts  $\Delta\lambda$  which are chosen such that all transit modes available to the different sized particle are observed.

The typical trajectories observed for a simulated rigid spherical particle in a circular post array is shown in figure 4.2. Here the particle size is  $D_{sp}\mu\text{m}$  and it is clear that the particles changes from the displacement mode at small row shifts ( $\Delta\lambda \leq 2.5\mu\text{m}$ ) to the zigzag mode as the row shift increases to ( $\Delta\lambda > 3.0\mu\text{m}$ ). It is interesting to note however, some less well defined trajectories appear at intermediate row shift values of ( $2.5 < \Delta\lambda < 3.0\mu\text{m}$ ), where particles appear to alternate between the displacement and zigzag modes randomly. These intermediary types of transit mode are subsequently referred to as “mixed modes”. Similar particle behaviour has also been observed in other simulations and experimentally [6, 130, 131]. Huang *et al.* suggests the random mode switching can be attributed to the diffusion of particles across different stream lines. The effect of diffusion should become increasingly pronounced in the regime where particle size is very close to the obstacle array critical size, as it becomes increasingly likely for particles to cross into neighbouring flow lamina. Ultimately an increase in the diffusivity of particles causes a widening of the transition region between well defined displacement and zigzag modes. In addition to diffusive effects, Kulrattanarak *et al.* speculate that mixed modes occur due to asymmetric flow line distribution in DLD geometries where  $G_x/G_y \leq 3$  and  $d/G_y > 0.4$  ( $G_x$  and  $G_y$  are the post gap sizes in the  $x$  and  $y$  directions). Despite the fact that the devices in simulations satisfy these criteria, with  $G_x = G_y = G$  and  $d/G_y = 1.5$ , the postulation for asymmetric flow effects is for point-like tracer particles in simulated flows. The simulations in this work consider particles of finite size and interactions with obstacles and flow field disturbances represent a significant departure from the systems simulated by Kulrattanarak *et al.*

Instead it is more likely that diffusion is responsible for the mixed mode, as the DPD fluid used in 2D simulations throughout this work accounts for thermal fluctuations.

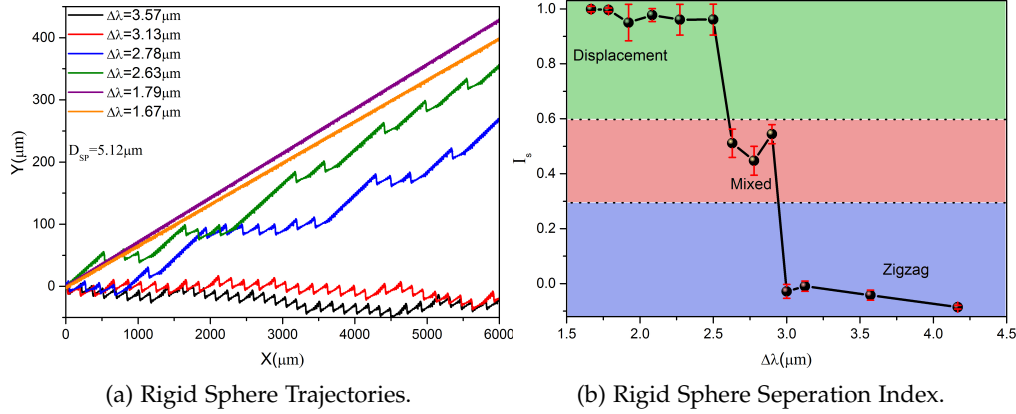


Figure 4.2: (a) Typical trajectories of a 2D rigid spherical particle with  $D_{SP} = 5.12 \mu\text{m}$  in conventional circular post arrays which are defined by different row shifts  $\Delta\lambda$ . (b) The separation index  $I_s$  for the same particle is shown as a function of the row-shift fraction  $\epsilon$ , where  $I_s$  is defined as the ratio of the mean lateral displacement of particles per post encounter and the row shift. Figures originally sourced with permission from [134].

In order to characterize particle trajectories in a quantitative manor, a dimensionless parameter called the separation index  $I_s$  is used. This separation index is defined as the ratio of the average lateral displacement of particles per post encounter to the row shift of the post array  $\Delta\lambda$ . Concepts similar to the separation index, such as migration angle, have been used previously in experimental works [6, 130–132]. Particles in an ideal displacement mode will have a value of  $I_s = 1$  because their average lateral displacement per post is equal to  $\Delta\lambda$ . Conversely, particles in an ideal zigzag mode should have a value of  $I_s = 0$ , as they will follow the fluid flow without significant influence from the obstacle array. The presence of mixed modes in this work means there is no simple binary choice between  $I_s = 0$  and  $I_s = 1$ . Instead, there exists a region of intermediary values in the transition region between displacement and zigzag modes. The transitions from the displacement mode through mixed modes to the zigzag modes for sphere with  $D_{SP}$  is shown clearly in figure 4.2b. Here, the mixed mode regions consistently fall in the range  $I_s = 0.3 - 0.6$ , irrespective of simulation time or initial simulation conditions. Consequently, the mixed mode region is formally defined as  $I_s \in [0.3, 0.6]$  and it follows that values of  $I_s > 0.6$  and  $I_s < 0.3$  define the displacement and zigzag modes, respectively.

The process described above for the particles of size  $D_{SP}$  is repeated for six additional particles of different diameters. The transit modes observed are presented in figure 4.3 as a function of the row shift fraction  $\epsilon$  and the normalized particle diameter. Furthermore, the line representing the critical radii of each DLD geometry as defined

by equation 4.2 is plotted so that the results can be compared with experimental results. Note that the mixed mode region follows the empirical transition line, indicating good agreement between the simulations and experimental observations. The agreement with Davis *et al.*'s results [133] demonstrates the reliability of the 2D models employed and shows their ability to capture the physical processes necessary to describe the separation of rigid spherical particles in circular DLD post arrays. Consequently, subsequent simulations of DLD arrays composed of posts with alternative shapes are expected to yield reliable results and provide valuable information for designing more exotic DLD devices for separating rigid spherical particles.

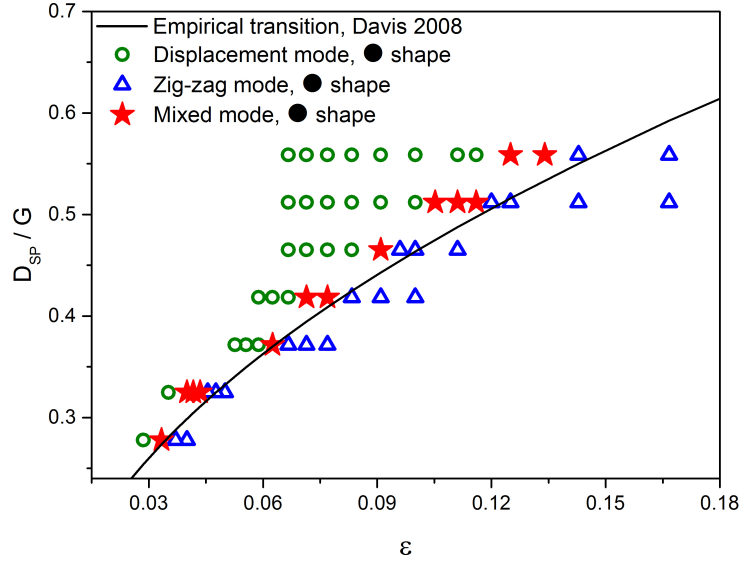


Figure 4.3: A transit mode diagram for rigid spherical particles in circular post arrays as a function of the normalized particle diameter ( $D_{SP}/G$ ) and the row shift fraction ( $\epsilon$ ). The predicted critical size from the empirical formula in equation 4.2 is drawn by the solid line and represents the expected transition region between displacement and zigzag modes. Figure originally sourced with permission from [134].

#### Alternative Pillar Shapes

With confidence in the 2D simulations to quantitatively describe rigid spherical particle transits in post arrays, additional simulations are carried out to investigate the effect of post shape. Diamond, square and triangular posts are simulated to determine how transit behaviour compares to that in circular post arrays. Compared to the circular posts, the chief difference of the alternative post shapes is the presence of sharp vertices which are expected to alter the flow profile in between posts.

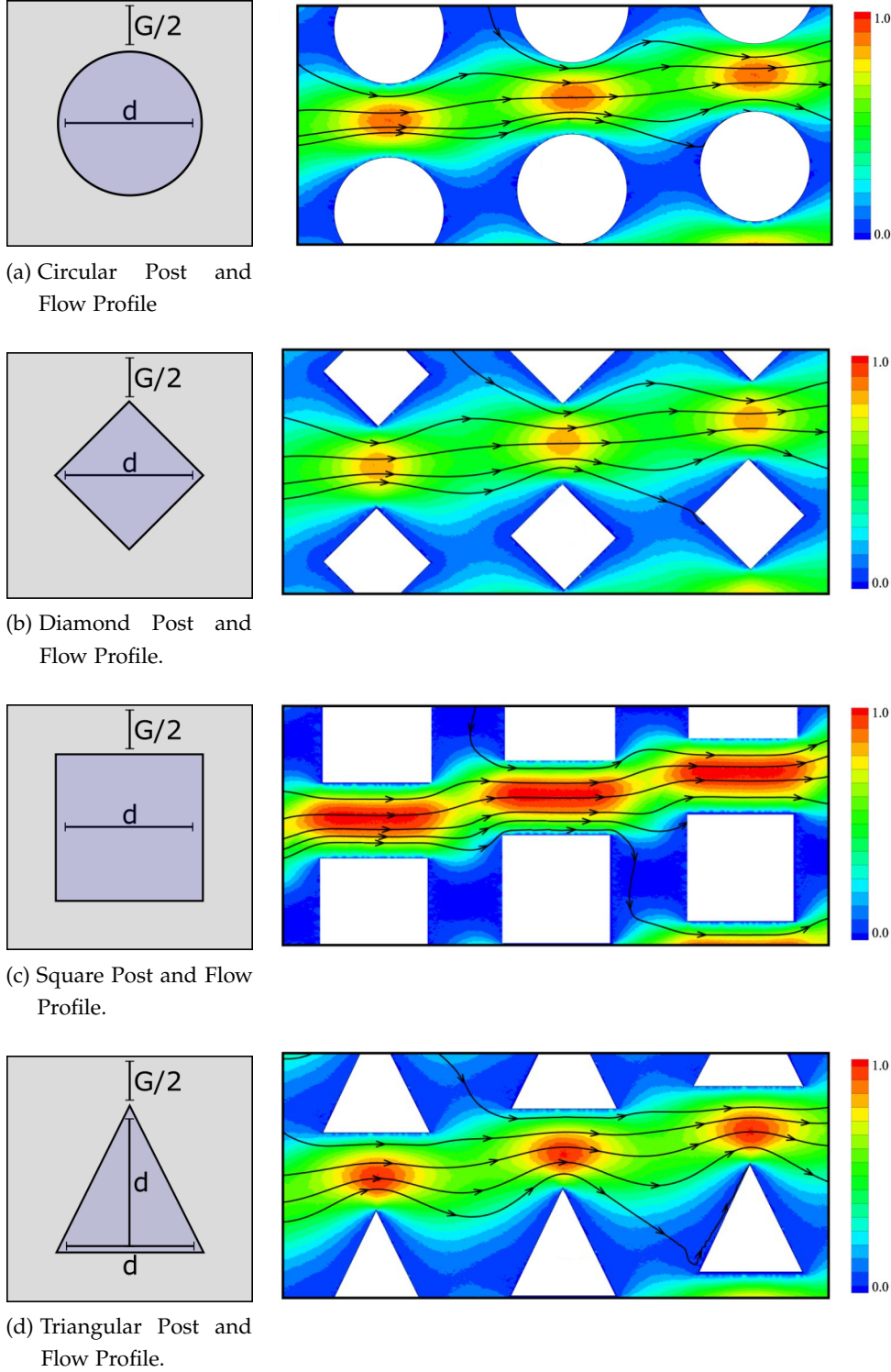


Figure 4.4: Each of the different post geometries are defined by the post-post gap  $G = 10\mu\text{m}$  and the post size  $d = 15\mu\text{m}$ . The flow profiles represents the flow velocity in the x direction and are normalised by the maximum flow value observed in the square post array. (a) Circular post schematic and the corresponding flow profile. (b) Diamond post schematic and the corresponding flow profile. (c) Square post schematic and the corresponding flow profile. (d) Triangular post schematic and the corresponding flow profile. Note the triangle has equal height and width so it is not equilateral but allows for equal posts spacing in the x and y direction. Figures originally sourced with permission from [134].

Figure 4.4 demonstrates the changes in flow profile induced by the different post shape arrays. The inter-post regions of highest velocity are characterised by elliptical, circular, cigar-shaped, and pear-shaped regions for the circular, diamond, square, and triangular post shapes, respectively. Additionally the minimal flow zones are dramatically different for the different post shapes. Most notably, the square post array has a vast region of almost zero flow between successive posts. The variations in flow profiles are expected to alter particle trajectories through the DLD arrays and the impact on separation of rigid particles is explored throughout this section.

The transit behaviours exhibited by rigid spherical particles in diamond and square post arrays are shown in figures 4.5 and 4.6. Compared to the simulation results and empirical predictions for circular post arrays, the main difference is that the transition from the zigzag to displacement mode occurs at a larger row shift fraction  $\epsilon$  which is especially prevalent for square posts. This shift in transition indicates a decrease in critical size for square and diamond post arrays and is in agreement with experimental and numerical studies [135–137].

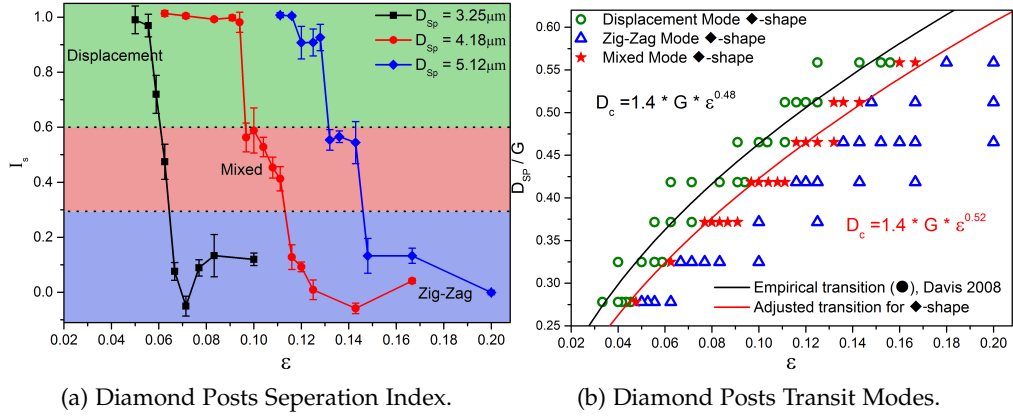


Figure 4.5: (a) The separation indices for three different sized rigid spheres  $D_{sp} = 3.25, 4.18, 5.12\mu m$  in diamond post arrays with different row fractions  $\epsilon$ . (b) Shows the mode diagram for rigid spherical particles in diamond post arrays and the corresponding adjusted empiric equation 3.7. Figures originally sourced with permission from [134].

The decrease in the critical size of the diamond shaped post array can be understood by appealing to the theory introduced in section 3.1.1 for lamina flow in obstacle arrays. The flow is split up into several ( $N = 1/\epsilon$ ) laminae, each with equal volumetric flow rate, and the width  $W$  of the lamina directly in contact with the post corresponds to the array's critical radius  $R_C$  (as shown in figure 3.2a). Given the fluid in all 2D simulations have identical volumetric flow rates, it can be inferred that pillar shapes which induce higher central channel flow velocities should have narrower laminae at the channel center and consequently wider laminae in direct contact with the pillars (i.e. larger critical size as  $W \approx R_C$ ). This is clearly the case when comparing the flow profiles for

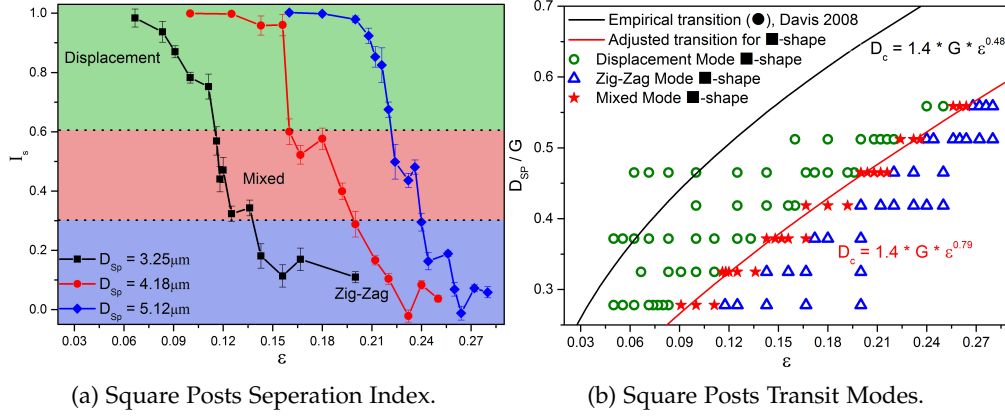


Figure 4.6: (a) The separation indices for three different sized rigid spheres  $D_{sp} = 3.25, 4.18, 5.12 \mu m$  in square post arrays with different row fractions  $\epsilon$ . (b) Shows the mode diagram for rigid spherical particles in square post arrays and the corresponding adjusted empiric equation 3.7. Figures originally sourced with permission from [134].

the circular and diamond post arrays, shown in figures 4.4a and 4.4b, explaining the decrease in critical size.

This concept however is not applicable to the square pillar arrays. In the case of circles and diamonds, the important steric interactions with particles occur at the top most point of the posts i.e. the zenith of the circle and the upper vertex of the diamond. Conversely, the most important steric interactions with the square pillars occur at the two vertices on it's upper side. The flow profile at these points is clearly no longer parabolic, indeed the flow is heavily influenced by the regions of low flow between horizontally adjacent posts. Furthermore, the flow lines shown in figure 4.4c show lateral flow velocity near the square vertices, which is not seen in parabolic flow. Consequently, square post arrays exhibit an even stronger reduction in critical size as the key steric interactions occur in both the inlet and outlet of the post gap, both of which have more complex flow fields than the roughly parabolic flow profiles seen for circular and diamond posts.

Recent work proposes an adaptation of the empiric formula 3.7 which includes a single shape dependant prefactor, allowing an estimation of the critical size in DLD arrays with different post shapes [137]. However, the values found from fitting data in numerical studies of square- and I-shaped arrays are identical, which is in disagreement with experimental observations [136]. Due to these discrepancies, a more general formula is proposed

$$D_C = \alpha G \epsilon^\beta, \quad (4.3)$$

where the dimensionless parameters  $\alpha$  and  $\beta$  are geometric factors determined by the shape and arrangement of posts.



Fitting the general formula 4.3 to the transit modes found for rigid spheres in circular, diamond, and square post arrays yields the values of  $\alpha$  and  $\beta$ ; as shown in figures 4.3, 4.5b, and 4.6b. For circular posts,  $\alpha = 1.4$  and  $\beta = 0.48$ , in agreement with equation 3.7. The values found for the diamond and square post arrays are  $\alpha = 1.4, \beta = 0.52$  and  $\alpha = 1.4, \beta = 0.69$ , respectively.

Triangular posts introduce a new layer of complexity to the trajectory behaviour as they have no top-down symmetry (unlike squares, diamonds, and circles). Consequently fluid flow near the base of a triangle is slower than that at the triangle's tip. This results in an asymmetric flow profile, as is evident from the pear-shaped flow regions shown in figure 4.4d. The broken symmetry means that the pillar array has two characteristic critical sizes depending on the flow direction. Figure 4.7 shows the separation indices and transit modes of different sized particles in triangular post arrays in both directions. It is clear that flow in the forwards direction (as shown in 4.4d) results in a reduced critical size compared to circular post arrays. Conversely, when the flow direction is reversed such that the key steric interactions occur along the triangle base where flow is slower, the critical size is larger than in circular post arrays. The general equation for critical size 4.3 is fitted to the simulations results in the triangular post arrays in figure 4.7b, and values of  $\alpha = 1.4, \beta = 0.44$  and  $\alpha = 1.4, \beta = 0.61$  for forwards and backwards flow, respectively.

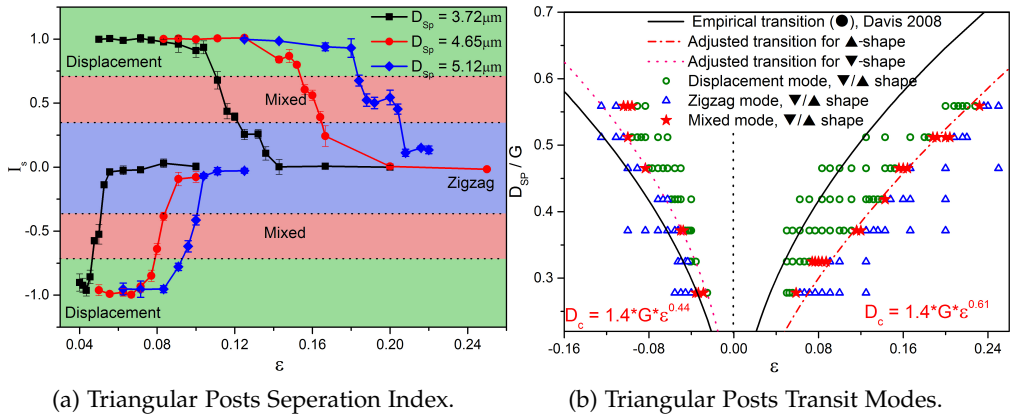


Figure 4.7: (a) The separation indices for three different sized rigid spheres  $D_{sp} = 3.25, 4.18, 5.12 \mu m$  in triangular post arrays with different row fractions  $\epsilon$  and for different flow directions. (b) Shows the mode diagram for rigid spherical particles in triangular post arrays in forwards and backwards fluid flow, and the corresponding adjusted empiric equations 3.7. Figures originally sourced with permission from [134].

Given the previous results for the circular post arrays agreed quantitatively with experimental data, the simulation results for the exotic post shapes in this section can be used directly for device design. For instance, considering the separation indices  $I_s$  for the square post arrays shown in figure 4.6a, a post array with a row shift of  $\Delta\lambda =$



$4\mu\text{m}$  ( $\epsilon = 0.16$ ) will induce displacement, mixed, and, zigzag transit modes for particles of size  $D_{SP} = 3.25, 4.18$ , and  $5.12$ , respectively. As such; the smallest particle with  $I_s = 0.11$  experiences almost no lateral displacement as it traverses the device, the largest particle with  $I_s = 1.0$  achieves maximal lateral displacement, and the intermediate sized particle with  $I_s = 0.60$  will be found roughly in the middle. This device could therefore be used for sorting a heterogeneous population of particles of these three sizes.

#### 4.3.2 Red Blood Cells

The investigation so far focuses on the motion of rigid spherical particles within DLD arrays. However, bioparticles which are commonly of interest can rarely be described as rigid spheres. Instead, they are often non-spherical and deformable, characteristics which have been shown to influence their trajectories through DLD devices [8, 9, 72]. To better understand the behaviour of deformable non-spherical particles, a number of simulations using the 2D RBC model from section 2.2.1 are performed for various obstacle arrays; including circular-, diamond-, and square- shaped posts. As RBCs are highly deformable and biconcave in shape, an effective RBC size  $D_{eff}$  in a given DLD geometry is defined to identify the transition between the displacement and zigzag mode. For instance, if a RBC within some obstacle array is found to transition from the displacement to the zigzag mode at a row-shift fraction  $\epsilon$ ,  $D_{eff}$  is then given by  $D_{eff} = \alpha G \epsilon^\beta$  where  $\alpha$  and  $\beta$  are determined from fitting data for rigid spherical particles.

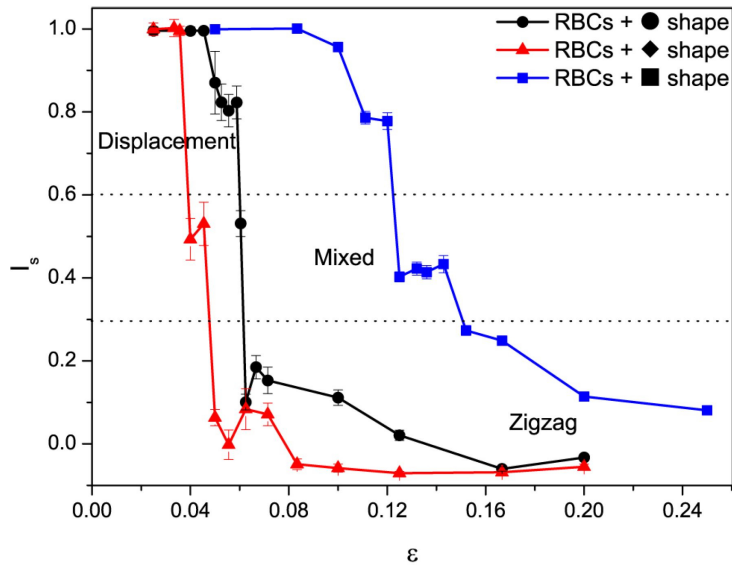


Figure 4.8: Typical distributions of the separation index  $I_s$  for RBCs within circular, diamond, and square post arrays as a function of the row shift fraction  $\epsilon$ . Figure originally sourced with permission from [134].

The separation index as a function of row-shift fraction  $\epsilon$  for RBCs in each post shape array is presented in figure 4.8. The transitions between the displacement mode and zigzag mode for each post shape are found to be:  $\epsilon = 0.06 \pm 0.002\mu\text{m}$  for circular posts,  $\epsilon = 0.043 \pm 0.007\mu\text{m}$  for diamond posts, and  $\epsilon = 0.14 \pm 0.01\mu\text{m}$  for square posts. Taking these values and using them with the adjusted fits of equation 4.3 found for rigid spherical particles yields effective RBC sizes of  $D_{\text{eff}} = 3.65 \pm 0.07\mu\text{m}$ ,  $2.65 \pm 0.14\mu\text{m}$ , and  $3.50 \pm 0.15\mu\text{m}$ , in circular, diamond, and square post arrays, respectively. Note that these effective sizes are in the range of 2D RBC model's maximum and minimum dimensions of  $\text{width}_{\text{RBC}} = 7.5\mu\text{m}$  and  $\text{height}_{\text{RBC}} = 2.0\mu\text{m}$ , suggesting that RBC's deformation and dynamic behaviour depend on the different flow fields created by each post shape.

Stroboscopic images of RBCs in transit via displacement and zigzag modes through the different post shape arrays are displayed in figure 4.9. For the majority of zigzag mode trajectories, a flipping motion tends to precede lane-swapping events. This can be attributed to the fact the effective size of the RBC is largest when it is orientated perpendicular to the flow direction. When the RBC is presented to the flow at such an orientation it usually experiences large deformations as it obstructs much of the fluid flow. Generally, if the RBC effective size satisfies  $D_{\text{eff}} < D_C$  then RBCs will transit the post array via the zigzag mode. The flow field between horizontally adjacent posts plays a major role in determining the transition to the zigzag mode. For example, the square post array shown in figure 4.9c, shows very gradual migration of the RBC in between posts as it undergoes a lane-swapping event due to the weak flow field shown in figure 4.4c. Note that the inter postal behaviour of RBCs is markedly different for the circular and diamond shaped post arrays.

If the effective RBC size satisfies  $D_{\text{eff}} > D_C$  then RBCs are continually bumped laterally upwards by interactions with the posts, resulting in displacement mode transit as shown in figure 4.9. Furthermore, when  $D_{\text{eff}} \gg D_C$  in the square post array, the displacement motion of RBCs changes from being in regularly bumped by successive posts (see the displacement modes in figures 4.9a and 4.9b) to steady flow at a fixed distance from the square posts, as shown in figure 4.9c. This displacement mode behaviour is very similar to that seen for RBCs in cylindrical micro-channels, where RBCs are repelled from the channel walls as a result of hydrodynamic interactions. This phenomenon is referred to as the lift force [108, 138, 139] and it is unsurprising that similar behaviour is observed in square post arrays, as the flow profile between posts in figure 4.4c looks very similar to that seen in cylindrical micro-channels.

In order to quantitatively describe the change in RBC shape due to deformation, a quantity called asphericity  $\delta$  is utilised to measure deviations from a circular shape.

$$\delta = \frac{(\phi_1 - \phi_2)^2}{(\phi_1 + \phi_2)^2}, \quad (4.4)$$

where  $\phi_1$  and  $\phi_2$  are given as the square roots of the two non-zero eigenvalues obtained from the squared radius-of-gyration tensor. The asphericity  $\delta$  varies from 0 to 1, depending on how close the particle shape is to that of a circle; where 0 is a perfect circle and 1 is a strongly elongated object. The 2D RBC model employed in this work has an asphericity of  $\delta \approx 0.29$  when at rest. By measuring the distribution of asphericities attained by a RBC in flow through a DLD array it is possible to monitor the different morphologies which are induced by the flow field and interactions with obstacles. Figure 4.10 shows the probability distribution of  $\delta$  in several different circular post arrays. Arrays which have row shifts that induce displacement mode transit clearly show very few deviations away from the equilibrium rest shape defined by  $\delta = 0.29$ . Conversely, post arrays with higher row shifts which cause a transition to the zigzag mode show an increased probability for deviations away from the rest shape towards a more circular shape, suggesting stronger RBC deformation in zigzag flow. This is supported by the previous observations, where RBCs experience strong deformations as they flip before lane-swapping events.

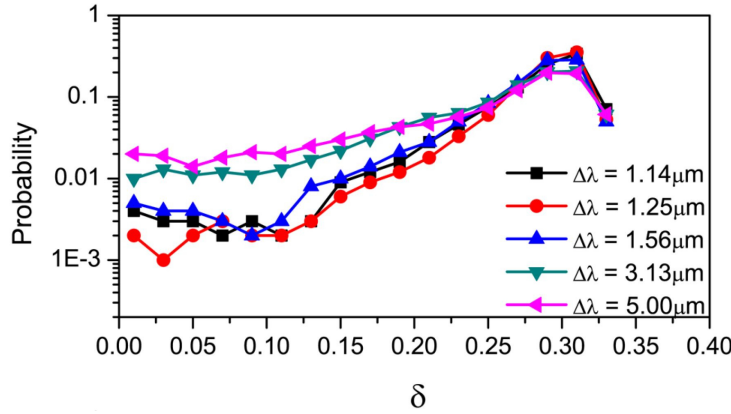
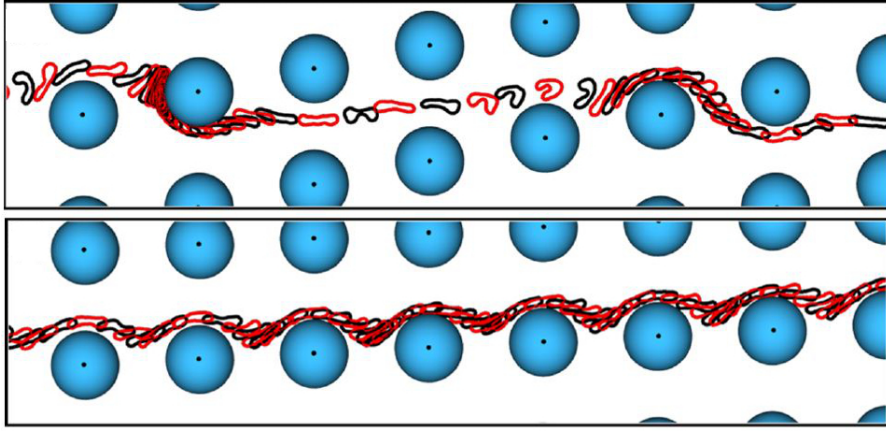


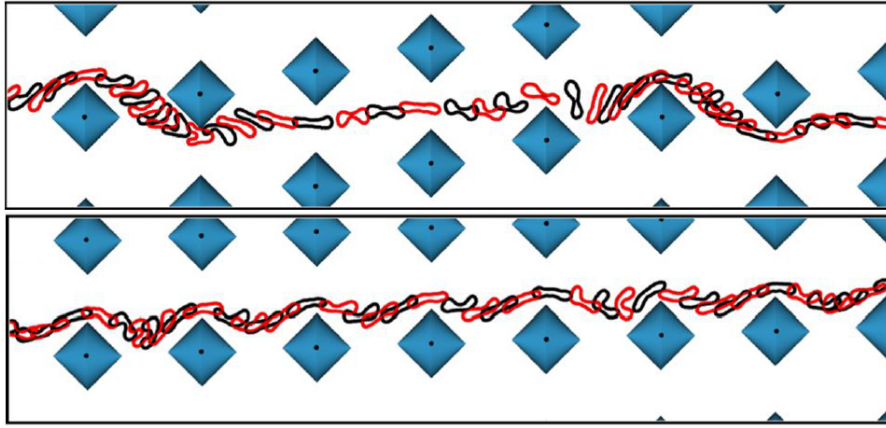
Figure 4.10: Distributions of the asphericity ( $\delta$ ) of RBCs in DLD arrays with circular posts at various row shifts  $\Delta\lambda$ . Figure originally sourced with permission from [134].

The results throughout this section should demonstrate that the transit of deformable non-spherical particles in DLD devices is much more complicated than that for rigid spheres. Rigid spherical particle sorting is solely based on particle size. Soft particle sorting however depends heavily on the deformation and dynamic behaviour of cells in post array flow field. For instance, the flow rate will effect the magnitude of particle deformation, meaning the sorting depends on the particle's mechanical properties, the fluid flow rate and the particle's effective size. This effect has already been observed experimentally [72]. Additionally, studies on the dynamic motion of anisotropic particles within DLD arrays has been shown to effect the sorting efficiency [136]. In light of these observations, it is clear that the concept of a single critical size for an obstacle array used to separate deformable non-spherical particles is overly simplistic. Instead

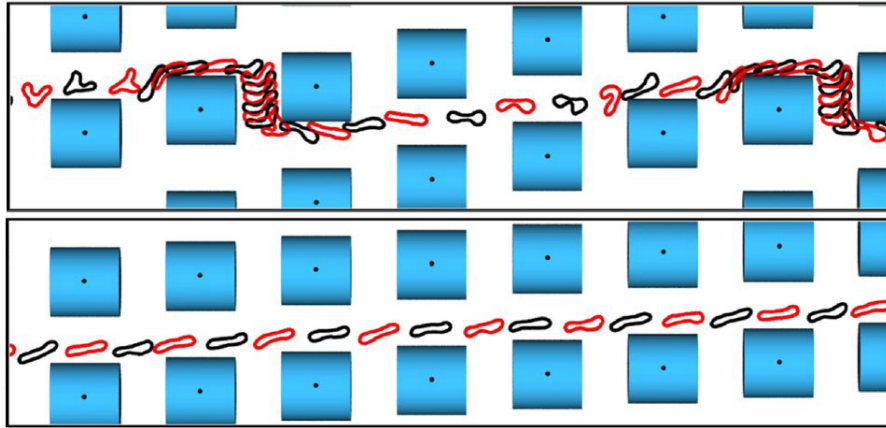
devices must be designed to account for specific particle properties and dynamic behaviour.



(a) Circular Post Dynamics.



(b) Diamond Post Dynamics.



(c) Square Post Dynamics.

Figure 4.9: Snapshots of typical RBC trajectories in different types of DLD array. The regular alternation of black and red RBCs represents sequential frames with an interval of  $0.023 \tau$ . (a) Shows the zigzag mode and displacement mode in circular post arrays with  $\Delta\lambda = 5.0\mu\text{m}$  and  $\Delta\lambda = 1.25$ , respectively. (b) Shows the zigzag mode and displacement mode in diamond post arrays with  $\Delta\lambda = 5.0\mu\text{m}$  and  $\Delta\lambda = 1.0$ , respectively. (c) Shows the zigzag mode and displacement mode in square post arrays with  $\Delta\lambda = 5.0\mu\text{m}$  and  $\Delta\lambda = 1.25$ , respectively. Figures originally sourced with permission from [134].

#### 4.4 SUMMARY

The chapters presented a 2D study of rigid spherical particles and deformable RBCs in transit through DLD obstacle arrays geometries using mesoscopic simulation techniques. The different post geometries used were circular, diamond, square, and triangular shapes. Simulations results for the rigid spherical particle agreed extremely well with experimental observations, where the transit behaviour could be categorized as the displacement, mixed, or zigzag modes. Particles in the displacement mode undergo regular lateral displacement as they regularly interact with successive posts to achieve a separation index of  $I_s \approx 1$ . The zigzag mode occurs for suitably large row shifts  $\Delta\lambda$  and allows particles to travel in the general flow direction with a separation index  $I_s \approx 0$ . Particles in transit with a separation index  $I_s \in [0.3, 0.6]$  are in the mixed mode, and randomly alternate between the displacement and zigzag behaviour. The size at which particles transition between the displacement and zigzag mode is well predicted by the empirical formula 3.7, which defines a critical particle size for a given circular array geometry.

The size at which rigid spherical particles transition from the displacement mode to the zigzag mode in diamond, square, and triangular shaped post arrays shows notable differences from the predictions made by the equation for circular posts. This is due to the fact that the post shape heavily impacts the flow field and hence alters particle trajectories. With this said, particle transit can still be described by the same modes and the correct critical particle size can be obtained by fitting a generalised form of equation 3.7 to the simulation results. Based on the quantitative agreement achieved between simulations and experiments of circular post arrays, the new found forms of equation 3.7 relating to each post shape should provide a means for designing devices which use alternative post shapes. Furthermore, the success of the general equation 4.3 for different post shapes indicates that the flow mechanisms responsible for size based particle sorting are qualitatively consistent across different DLD device geometries.

Finally, flow behaviour for non-spherical deformable particles in different DLD geometries has been explored using a 2D RBC model. The results show that deformation and dynamic behaviour of RBCs in fluid flow strongly effect which transit mode is adopted within a given geometry compared to that of a rigid sphere. Specific to dynamic motion; tumbling behaviour plays a key part in the transition to the zigzag mode as cell flipping consistently occurs before lane-swapping events. Furthermore, as the degree of cell deformation will depend on the shear forces RBCs experience in flow, the flow rate will also determine the row shift  $\Delta\lambda$  where the transition from zigzag to displacement mode occurs. Similarly, the post shape also effects the flow field and consequently the simulations with different post shapes show shifts in the transition region between the displacement mode and zigzag mode.

Ultimately the results demonstrate that the simplified picture of a single critical size for a given DLD array geometry can no longer be used to sort anisotropic deformable

particles. This is because transit behaviour is no longer solely dependent on particle size. Instead, the particle's mechanical properties, shape and dynamic behaviour are of explicit relevance. This considerably complicates the device design for sorting non-rigid spherical particles but it also presents opportunities for novel sorting schemes based on characteristics such as deformability and shape. The work following this chapter will begin to address the design of such devices by using similar simulations but in 3D to achieve quantitative agreement with experiments for RBCs in DLD devices.





## UNDERSTANDING RBC DYNAMICS IN DLD: A 3D SIMULATION APPROACH

---

### 5.1 INTRODUCTION

The work presented in this chapter combines numerical and experimental investigations of RBC sorting in DLD devices. The previous chapter was able to achieve quantitative agreement between 2D simulations and empirical predictions for rigid sphere behaviour in DLD devices. However, 2D simulations are clearly limited to a qualitative description for RBCs, as the shape and dynamic behaviour of RBCs are intrinsically 3D. The experimental work presented focuses on precisely following the trajectories of RBCs through DLD post arrays, differing from typical experimental approaches which only measure the lateral location of particles as they exit the obstacle array. This rigorous analysis is necessary because, as seen in the previous chapter, RBC transit modes are not limited to the displacement and neutral zigzag modes. Generally the experimental and simulation results find that the displacement mode defined by device geometry remains similar to that seen for rigid spherical particles, whilst the range of zigzag modes observed are depicted in figure 5.1. The variety of zigzag modes can lead to positive, neutral and negative displacement of RBCs within different obstacle array geometries.

The detailed experimental data and the precise description of RBC deformation and dynamics afforded by simulation results allow rigorous investigation of the underlying physical mechanisms responsible for the different transit modes. Examination of RBC motion immediately before and after lane-swapping events in DLDs helps reveal the relationships between RBC trajectory, its dynamic behaviour and hydrodynamic interactions with posts. This relationship is further investigated by altering the ratio between the intracellular and extracellular viscosity, as viscosity contrast is known to strongly effect RBC dynamics [103]. Indeed, simulation and experimental results both demonstrate that dynamic behaviour such as tumbling and tank-treading can be invoked, which in turn alter the trajectories of RBCs. Ultimately the results show that it is possible to control and rationalize RBC trajectories in DLD devices based on factors other than size. Furthermore, the reliability of the simulation techniques employed for deformable anisotropic particles is proven to be a powerful tool for designing novel sorting strategies which depend on particles' dynamic behaviour and hence, intrinsic mechanical properties such as deformability and internal viscosity.

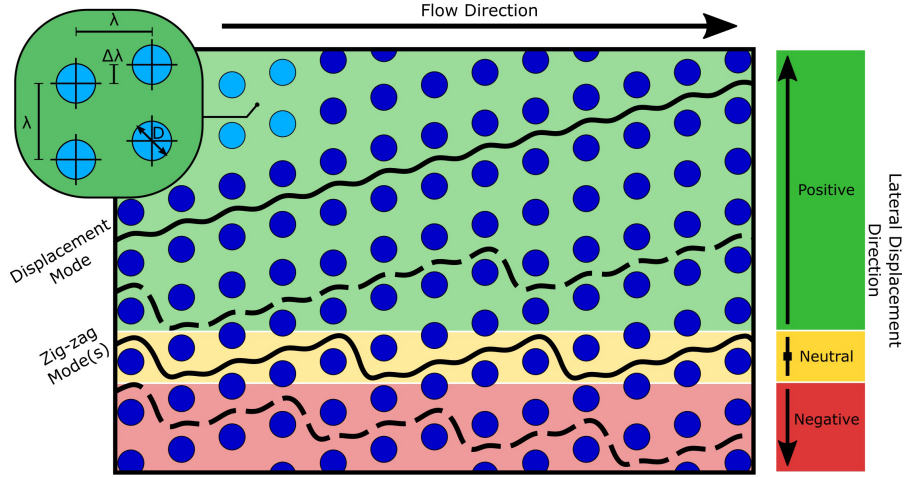


Figure 5.1: The possible trajectories of particles traversing an obstacle array defined by the central post-to-post distance  $\lambda$ , row shift  $\Delta\lambda$ , and post diameter  $d$ . Solid lines represent the displacement (no lane swapping) and neutral zig-zag (swapping between lanes, where a lane is defined as a straight path running parallel alongside a row of pillars) modes available to rigid spherical particles. Anisotropic deformable particles have access to many additional zig-zag modes which allow for positive or negative lateral displacement, two of which are shown as dashed lines. Figure source with permission from [140].

## 5.2 SIMULATION SETUP

The fluid within the simulations is represented using the mesoscale hydrodynamic approach SDPD, introduced in section 2.1.3, which has been adapted to conserve angular momentum [96]. The RBC membrane is modelled as a triangulated network of springs [119–121], and is coupled to the fluid via frictional forces acting upon the vertices.

The obstacle array is simulated using a similar set-up to the one in the previous chapter for 2D simulations. The infinite bumper array is achieved with the same periodic boundary conditions in the  $x$  and  $y$  directions and a shift in the  $y$  direction for each boundary crossing event in the  $x$  direction, as shown in figure 4.1. The flow is driven by a body force in the  $x$  direction applied to each fluid particle and cross flow in the  $y$  direction is negated by application of an adaptive force to mimic the constraints enforced by side walls in real DLD devices. However, there are some key modifications required to bring the method into three dimensions shown in figure 5.2. Firstly, the simulation exists in a cube shaped box as opposed to square, necessitating the implementation of impenetrable non-slip planes to represent the device roof and floor. Secondly, the DLD obstacle is represented as a cylinder instead of a circle, with its axis perpendicular to the roof and floor of the domain box.

The floor, ceiling, and post boundaries in the DLD device are modelled as a layer of frozen particles which share the same equilibrium structure as the suspending fluid. Additionally, in order to prevent particles from penetrating the walls and mixing of the

intra- and extra- cellular fluid, RBC vertices and fluid particles are subject to bounce-back reflections at walls and the RBC membrane.

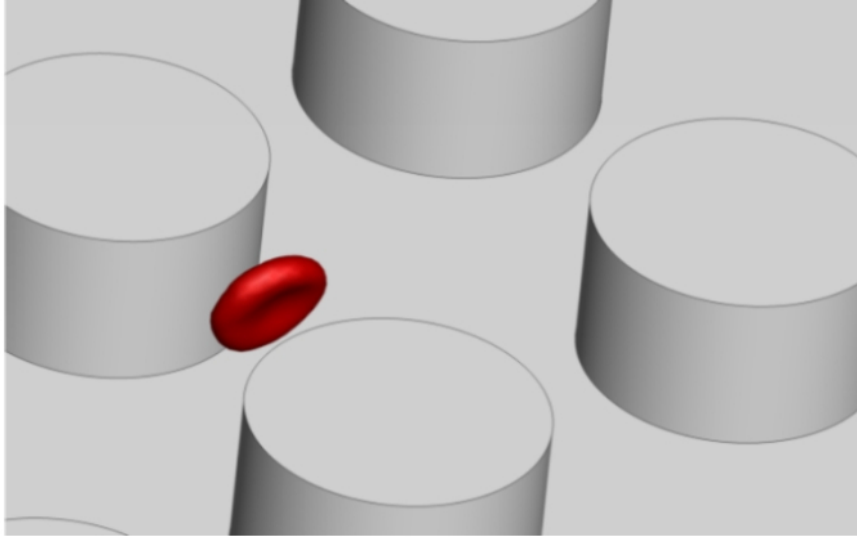


Figure 5.2: A snap shot of a simulated RBC in a cylindrical DLD obstacle array. Figure source with permission from [140].

### 5.3 EXPERIMENTAL SETUP

The experimental devices employed in this work were fabricated using replica molding, and the same method and equipment was applied as in previous experimental work by Beech *et al.* [72]. Specific information regarding the details of post-array manufacturing are outlined in appendix B. Two different devices are used: The first device is thick enough to allow RBCs to explore a full range of dynamic behaviour, with a distance between the device floor and ceiling of  $H = 11 \mu\text{m}$  (larger than a RBC diameter of about  $8 \mu\text{m}$ ). The second device is sufficiently thin to force horizontal orientation of RBCs and suppress dynamic behaviour due to confinement, with a thickness of  $H = 4 \mu\text{m}$  (smaller than the RBC diameter but larger than the RBC thickness which is roughly  $2 - 3 \mu\text{m}$ ). This concept of controlling particle orientation using confinement is illustrated in figure 3.4. A schematic of the device structure and pillar array geometry can be seen in figures 3.6 and 4.1. Both devices have chirped structure composed of 13 sequential sections, each housing a cylindrical obstacle array defined by the post diameter  $D = 20 \mu\text{m}$ , central post-to-post distance  $\lambda = 32 \mu\text{m}$ , and row shift  $\Delta\lambda$ , which increases from a value of  $0.8 \mu\text{m}$  to  $8.8 \mu\text{m}$  incrementally between subsequent sections (see Appendix B).

Given that the experiment required blood samples, the study received the necessary approval of the Review Board of Lund University and was performed in accordance with all applicable guidelines and regulations. Furthermore, blood was taken from

healthy volunteers via finger pricking (informed consent was obtained from all subjects). The samples were subsequently diluted in an autoMACS™ buffer to achieve a suspending medium viscosity roughly equal to that of blood plasma. In cases where the viscosity of the suspending medium viscosity required alteration, Dextran-500 (# 700013-096, VWR International LLC, PA, USA) solute was added at a concentrations of 11%, 4.5%, and 1%, in order to change the viscosity by factors of 20, 5, and 2.5, respectively. The dilute blood solutions were driven through the DLD devices at a pressure drop of 22mbar. Running the simulations at a comparable pressure drop, the average velocity of fluid travelling between two vertically adjacent posts was found to be  $0.5\text{mm s}^{-1}$  for the thick device and  $0.12\text{mm s}^{-1}$  in the thin device, values which correspond to physiological conditions for blood flow in capillaries.

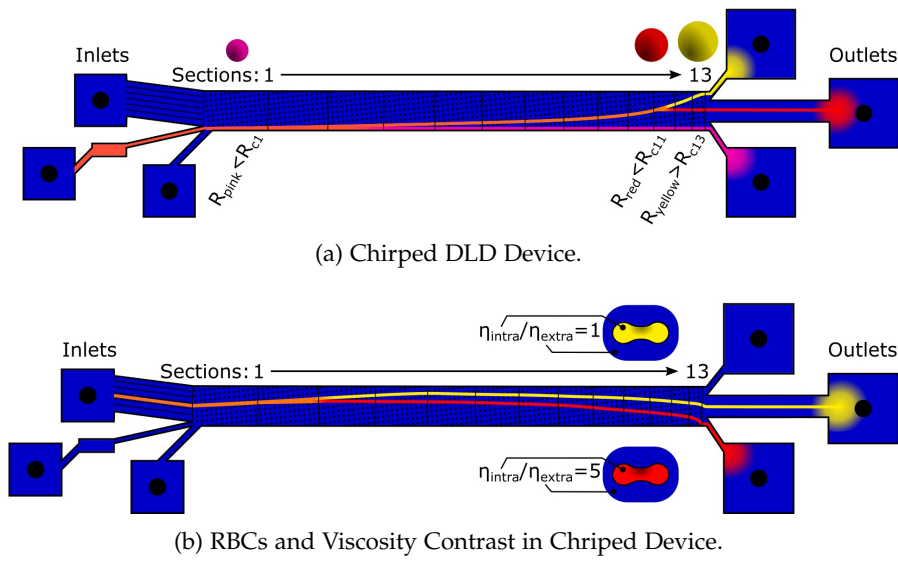


Figure 5.3: Schematic behaviour of particles in a DLD device with 13 successive sections, each with larger critical size. (a) Shows the device being used to sort 3 sizes of rigid spherical beads, each size undergoes a transition from the displacement mode to a neutral zig-zag mode in a different section. The orange color corresponds to an initially polydisperse suspension of different spheres, while the other colors depict separated monodisperse fractions at the end of the device. (b) Shows how the same device sees very different separation trajectories when sorting RBCs undergoing different types of dynamic behaviour. Dynamic behaviour can be controlled by changing the viscosity contrast between interior and extracellular fluids. Note that due to the presence of negative zig-zag modes for RBCs it is necessary to use the large central inlet to accommodate separation in both directions. Figures source with permission from [140].

## 5.4 RESULTS

The experimental and simulation results throughout this chapter work are presented in unison to facilitate a detailed and continuous comparison. Initially the possible transit modes available to RBCs in the two different DLD devices are considered, as these modes differ from the displacement and neutral zigzag modes available to rigid spheres and to the modes predicted for RBCs in 2D simulations. The transit of deformable anisotropic particles through the 13-section device is considerably different from that of rigid spheres, as depicted schematically in figure 5.3. This is not only due to transitions from the displacement to zigzag modes occurring in different sections but also due to the availability of additional zigzag modes. Ultimately, there is no reason why a particle should prefer the neutral, zero lateral-displacement, zigzag mode; depending on the frequency of lane swapping, negative, neutral, and positive net lateral displacement can be induced.

Subsequent investigation focuses on RBC dynamic behaviour and the role it plays in determining the device sections which show a transition between transit modes. The dynamic behaviour is controlled using the different confinements of the thick and thin devices, and by altering the ratio between the intra-cellular viscosity of the RBC  $\eta_i$  and the viscosity of the external suspending medium  $\eta_o$ . This ratio is called the viscosity contrast  $C$  and is defined as

$$C = \frac{\eta_i}{\eta_o} \quad (5.1)$$

Finally, a qualitative discussion highlights the reasons for different dynamic behaviours and how certain dynamics favour certain transit modes.

### *DLD transit modes in the thick device*

In order to understand the nature of the transit modes available to RBCs, the trajectory of a RBC's center of mass is recorded via its  $x$  and  $y$  coordinates as it traverses the obstacle array. Here the  $x$  and  $y$  axes correspond to the direction of flow and perpendicular to the flow, respectively. Figure 5.4b depicts a selection of different zig-zag modes of RBCs in different sections of the thick DLD device at a physiological viscosity contrast of  $C = 5$ , while figure 5.5a shows a side by side comparison of simulated and experimental snapshots of a RBC undergoing a zigzag trajectory in section 11 of the device. Section 11 of the device is defined by a row-shift of  $\Delta\lambda = 6.8\mu\text{m}$  and the high frequency of lane-swapping in the RBC trajectory makes it a good initial example of a zig-zag mode because it is possible to view it with isometric scaling. This type of data representation forms the basis for comparisons between experimental and simulated results in this chapter. In other sections of the devices, trajectories might have periodicity at length scales too large for isometric visualization. Consequently, the trajectories

seen in Fig. 5.4b are displayed with different  $x$  and  $y$  scaling. This allows a complete, albeit distorted, depiction of RBC trajectories in all manner of transit modes. Furthermore, the experimental trajectories in figure 5.4b have been selected from a population of recorded trajectories in accordance with pre-screening criteria outlined in section 3.2.3, used to remove trajectories of insufficient length as well as trajectories where inter-RBC interactions were detected. Further details about the data sample and the pre-screening criteria can be found in appendix B.

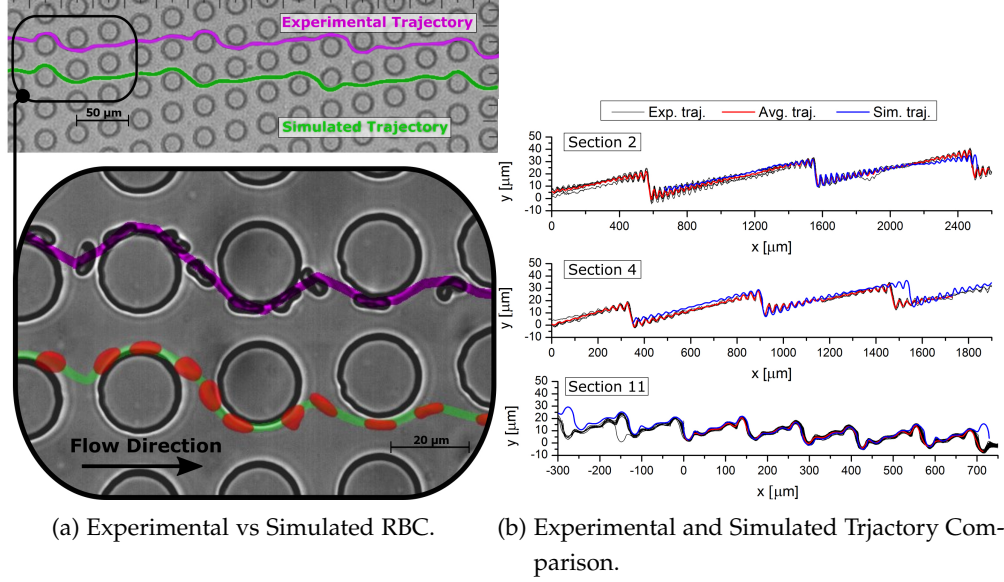


Figure 5.4: Experimental and simulated trajectories for RBCs at viscosity contrast  $C = 5$ . (a) The trajectories of experimental and simulated RBCs which are obtained by following their center of mass through the post array. Zoomed in a; stroboscopic image shows snapshots of the experimental and simulated RBC used to obtain the trajectories. (b) Experimental and simulated RBC trajectories for several sections of the thick device. Black lines show multiple aligned experimental RBC trajectories and red lines correspond to average experimental trajectories. The blue lines show the RBC trajectories found in simulations. Section 2 shows an approximately neutral zig-zag mode, section 4 illustrates a positive zig-zag mode, and section 11 leads to a negative zig-zag mode. Figures source with permission from [140].

Figure 5.4b compares experimental and simulated RBC trajectories in various sections of the thick DLD device and nicely presents the range of different zig-zag modes observed. In order to quantitatively describe and differentiate these zigzag modes, we define their average lateral displacement,  $l$ , per post encounter. The value of  $l$  can be calculated by considering the competing effects of lane-swapping events and lateral displacement induced by the geometry of the pillar array. The positive lateral displacement per post is simply  $\Delta\lambda$  and the average displacement per post encounter due to

lane-swapping is given by the frequency of lane-swapping events multiplied by the distance between rows,  $-\lambda f_i$ . The additive effect of these two motions yields

$$l_i = \Delta\lambda_i - \lambda f_i, \quad (5.2)$$

the average lateral displacement per post encounter in the  $i^{\text{th}}$  section of the device. The frequency  $f_i$  of lane-swapping is determined by the inverse of the average number  $m$  of post encounters per lane-swapping event. Theoretically,  $m$  could have any positive value, where the special cases  $m = \infty$  and  $m = \lambda/\Delta\lambda$  yield the ideal displacement and neutral zigzag modes discussed previously. Note that the value  $l$  is very closely linked to the dimensionless separation index introduced in chapter 4, which can be thought of as  $I_s = l/\lambda$ . However the average displacement per post  $l$  is used throughout this chapter to emphasise the quantitative agreement between experiment and simulations in terms of real physical units.

Using the formula 5.2 for  $l_i$  the trajectories in figure 5.4b are analysed to quantitatively describe the observed zigzag modes: The trajectory in section 2 with  $\Delta\lambda_i = 1.2 \mu\text{m}$  yields an approximately neutral zigzag mode with  $l_2 = 1.2 - 32/30 = 0.13 \mu\text{m}$ . Section 4's trajectory is slightly more positive with  $l_4 = 0.22 \mu\text{m}$  arising from the row shift of  $\Delta\lambda_i = 2.0 \mu\text{m}$ . Finally, section 11 with a row shift of  $\Delta\lambda = 6.8 \mu\text{m}$  induces a negative zigzag mode, where the lateral displacement caused by the array geometry is offset by regular lane-swapping events to give an average lateral displacement per post of  $l_{11} = 6.8 - 32/4.4 = -0.47 \mu\text{m}$ . Note that  $m$  takes a non-integer value in this case, because the periodicity between lane-swapping events is irregular. The presence of irregular periodicities supports the idea that changes in RBC orientation and deformation cause it to explore more than one flow stream, hence exhibiting more complex behaviour than simple rigid spheres. However, it is important to emphasize that the non-integer  $m$  values we find are not the result of random RBC behaviour in the device. The behaviour of RBCs is governed by local fluid flow and their elastic and viscous properties, which is supported by RBC dynamics in shear [141, 142] and tube [103] flows, and therefore, there is no reason to expect random RBC dynamics in DLDs. The only randomness arises from the initial orientation and position of the RBCs as they enter the device, and the thermal fluctuations which result in cell diffusion and membrane flickering; however, RBC diffusion can practically be neglected in the current simulation and experiments in comparison to RBC transport induced by the flow due to flow rates sufficiently large for a high Péclet number. Consequently, even the trajectories with a non-integer lane-swapping frequency are expected to be deterministic for the fixed simulation conditions. In experiments, there also exist a number of uncertainties (e.g., cell properties, flow control, device fabrication limits) which may affect the trajectory of a cell in the device. In fact, The inherent variability in RBC properties may perhaps be the least controlled variable. However, the example of experimental results for section 11 of the thick device in figure 5.4b, which consists of 69 well-aligned RBC trajectories (see figure 5.5), shows a consistent pattern of traversing

4 or 5 obstacles before performing a lane-swap. This indicates that the trajectories are not random, as otherwise a much broader variety of lane-swapping patterns would be observed, and that the geometry of section 11 and the corresponding flow are not very sensitive to ‘moderate’ variations in RBC properties. Furthermore, the few trajectories which could not reach adequate alignment with the majority of the population were found to reside in two well defined sub-populations shown in figure 5.5b, and not a random distribution of 4,5 lane-swapping intervals. This complex yet deterministic nature of trajectories can be explained by an interplay between RBC dynamics (e.g., flow-rotation, deformation) and local flow mainly determined by the periodic geometry of the DLD device. Thus, a mismatch between RBC motion and periodic geometry may result in several different cell states (e.g., position, orientation) after a lane-swap, which will in turn decide the number of pillars traversed before the next swap and indeed the lane-swapping pattern thereafter.

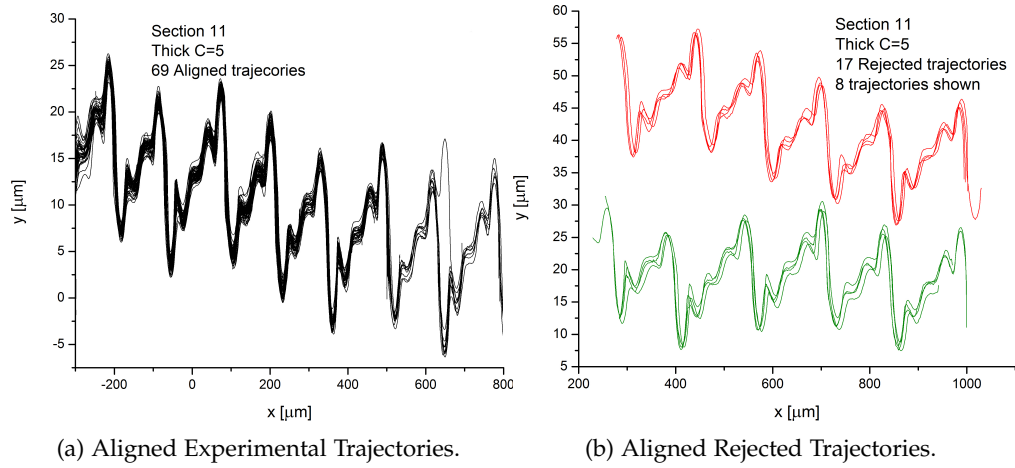


Figure 5.5: The accepted and rejected experimental trajectories of RBCs recorded through section 11 of the thick DLD device at  $C = 5$ . (a) An example of the most prevalent trajectory observed in section 11 of the DLD device. 69 trajectories were aligned, each showing the displacement-zigzag pattern  $\{5, 4, 5, 4, 4, 5, 4\}$ . (b) A selection of the two minor populations of trajectories observed in section 11 of the thick device. 17 trajectories could not be aligned sufficiently with the other 69, instead they were found to undergo the displacement-zigzag patterns  $\{5, 4, 4, 4, 5\}$  or  $\{5, 4, 5, 5, 4\}$ . Figures source with permission from [140].

Plotting the changing values of  $l_i$  as RBCs traverse the entire DLD obstacle array reveals the section in which transitions occur between different sorting modes. The average lateral displacement per post encounter  $l_i$  for each section of the thick device defined by  $\Delta\lambda$  is shown in figure 5.6a and the number of experimental RBC trajectories used to calculate each  $l$  value is shown in table 5.1. The RBC acceptance and rejection data for the remaining experimental results in this chapter are presented in appendix B.



The results allow several important conclusions to be made. Firstly, there is very good agreement between the simulated and experimental trajectories recorded at the physiological viscosity contrast  $C = 5$ . The only notable deviations occur in the final sections of the device, where experimental trajectories are seen to undergo more negative lateral displacement due to flow field disturbances caused by close proximity to the flow outlet. These outlet disturbances are observed consistently throughout the course of the experimental component of this work. The close agreement away from outlet disturbances indicates that the simulation techniques adequately capture hydrodynamic effects, and RBC dynamics and deformation. Secondly, the transition between the zigzag mode and displacement mode occurs in the first two sections of the device. Following the transition, RBC transit modes become gradually more negative as the row shift  $\Delta\lambda$  in each section increases along the length of the device. The increase in  $\Delta\lambda$  promotes positive displacement due to the obstacle array geometry, however there is also a tendency towards lane-swapping events as the critical size is also increasing. Whilst the negative zigzag modes observed display only slight deviations from the neutral mode, they still present a key manifestation of the transit behaviour attainable to deformable particles and unavailable to rigid spheres. The difference in behaviour could be due to the dynamic properties of RBCs and the responsible mechanisms are discussed later in this chapter. Finally, it is worth noting that the additive effect of some sections may cancel each other out, making their serial use in a chirped DLD device inefficient for separation.

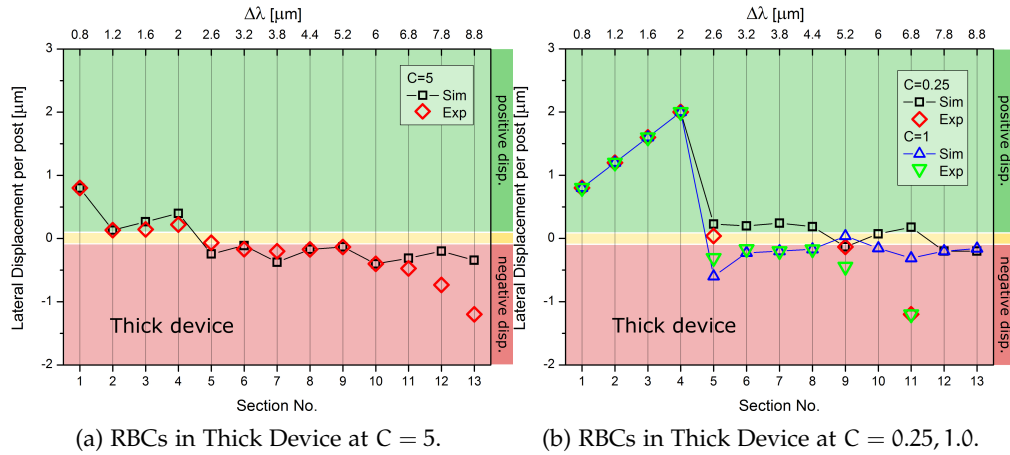


Figure 5.6: The average lateral displacement per post encounter  $l$  of RBCs in each individual section of the thick device at various viscosity contrasts  $C = \eta_i/\eta_o$  (a) Data for the thick device at  $C = 5$ . Experimental values agree well with the simulated values and the transition to zig-zag modes occurs between sections 1 and 2. (b) Data for the thick device at  $C = 1$  and  $C = 0.25$ . Experimental and simulation trajectories at both viscosity contrasts undergo a transition from displacement to zig-zag modes between sections 4 and 5, later than found for the physiological value of  $C = 5$ .

SECTION	TOTAL # OF TRAJ.	ACCEPTED	ACCEPTED FRACTION	AVERAGE # OF POSTS
1	27	25	0.93	46
2	25	20	0.8	67
3	17	15	0.88	37
4	10	9	0.9	30
5	15	14	0.93	27
6	12	11	0.92	26
7	28	26	0.93	25
8	25	22	0.88	32.2
9	23	22	0.96	28
10	50	48	0.96	22
11	86	69	0.80	22
12	134	113	0.84	19
13	97	89	0.92	14

Table 5.1: The total number of RBC trajectories recorded in each section of the thick device at  $C = 5$  and the number of excluded and accepted trajectories. The average number of posts describes number of posts traversed by the RBCs and hence the length of the average trajectory.

### *DLD transit modes in the thin device*

The thin DLD device prevents RBC re-orientation in flow, forcing cells to align with the device floor and ceiling. The highly constrained environment of the thin device limits the range of dynamics available to RBCs and consequently, the results should be closer to those for rigid spheres. Figure 5.7a shows the average lateral displacement of RBCs per post encounter for the range of row shifts  $\Delta\lambda$  for each section of the thin device.

At a viscosity contrast of  $C = 5$ , the results for sections 1 – 7 demonstrate an excellent agreement between simulations and experiment, showing strong positive lateral displacement. In section 7 of the device, lane-swapping events start to occur. However, these events are infrequent and the video frame is too narrow to capture successive lane-swapping events in one trajectory. Thus it is difficult to obtain a reliable period for the zigzag trajectory. Furthermore, simulations must run for an infeasible length of time before they capture multiple lane-swapping events in section 7. Ultimately, strong positive lateral displacements is observed in sections 1 – 7 of the thin device at  $C = 5$ . In the subsequent sections, lane-swapping events occur frequently and the RBCs traverse the post arrays in well-established zigzag modes in both experimental and simulated trajectories. This transition between the displacement mode to the lane-swapping dominated zigzag modes in section 8 agrees well with the critical size of the array predicted by equation 3.7 for rigid spheres. The empirically determined critical size is  $R_C = 3.02\mu\text{m}$  only slightly less than the RBC radius of  $4.00\mu\text{m}$ , which will effectively be smaller in the DLD device due to deformation in the flow. It is also important to notice the discrepancy between experimental and simulated trajectories after the transition to zigzag modes in figure 5.7a, which is discussed below.

A sharp transition from pure positive displacement modes to zig-zag modes occurs in section 8 of the device for  $C = 5$  (figure 5.7a). It is in this section and subsequent ones that agreement between simulations and experiments appear to begin to break down. Specifically, simulated trajectories undergo less severe negative lateral displacement due to a smaller frequency of lane-swapping events. Additionally, increasingly positive zigzag modes are observed in sections 8-10 in simulations, due to the increasing value of  $\Delta\lambda$  in subsequent sections which causes an increased positive lateral displacement but a relatively low increase in the frequency of lane-swapping events. Larger deviations between experimental and simulation results are not unexpected when the confinement of the RBC is increased in a device due to the fact that the forced orientation of RBCs in the thin device amplifies the impact of size differences between simulated and sample RBCs. The diameter of real RBCs varies with a range between  $6\mu\text{m}$  and  $9\mu\text{m}$ , which is approximately a 10 – 15% deviation from the simulation value of  $8\mu\text{m}$ . The possible differences in size are on the same order of magnitude as the change in critical radius for successive sections of the thin device.

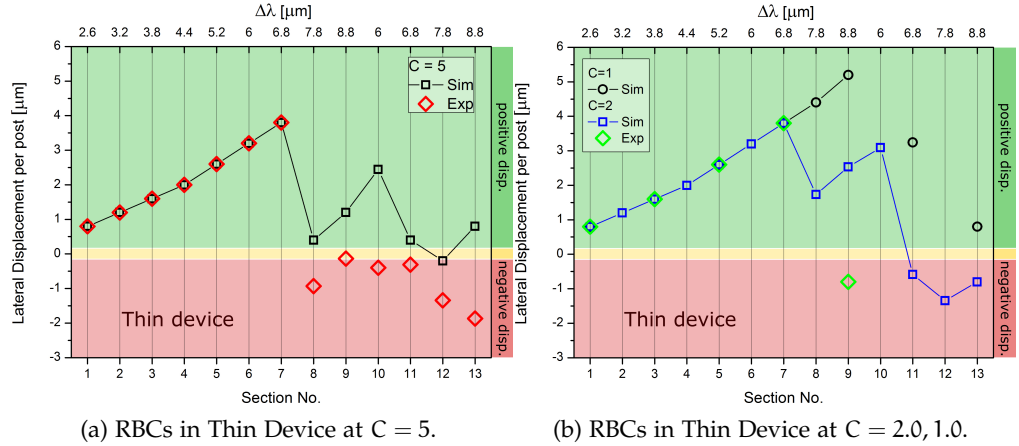


Figure 5.7: The average lateral displacement per post encounter of RBCs in each individual section of thin device at various viscosity contrasts  $C = \eta_i/\eta_o$  (a) Data for the thin device at physiological viscosity contrast  $C = 5$ . Transition to zigzag modes is the same in experiments and simulations, occurring between sections 7 and 8. However, evolution of zigzag modes with section number shows discrepancies due to inherent variability in RBC size. (b) Data for the thin device at viscosity contrasts  $C = 1$  and  $C = 2$ . Transition to zigzag modes at contrast  $C = 2$  occurs between sections 7-8 for simulations and experiments, whereas the transition occurs in section 10 for the simulation at  $C = 1$ . Again, variability between experimental and simulation results can be attributed to the inherent variability in RBC diameter. Figures source with permission from [140].

To investigate the effect of RBC size in more detail, additional simulations for RBCs with different diameters are carried out at a viscosity contrast of  $C = 5$ , the results are displayed in figure 5.8. The simulation results at different RBC sizes indicate that the discrepancies between experimental and simulated results are likely a result of the inherent variations in size that occur in RBC populations. These results also confirm that the later sections in the thin device are extremely sensitive to sub-micrometer variations in size. Furthermore, it is hard to achieve an extensive comparison between experimental and simulated results in figure 5.8 because the experimental data points correspond to the averages of multiple RBC trajectories which potentially have different sizes. Indeed, a number of experimental trajectories were excluded from the alignment process as they could not meet the alignment criteria. The number of rejected trajectories was significantly higher in the thin device than in the thick device, as can be seen in figure 5.9, which displays a clear decrease in the fraction of accepted trajectories in the thin device after the transition to zigzag transit modes in section 8 of the device. The thick device is expected to be less sensitive to size variations in RBC populations because the effective RBC size correspond to the cell thickness, rather than the cell diameter, due to its preferred orientation in flow.

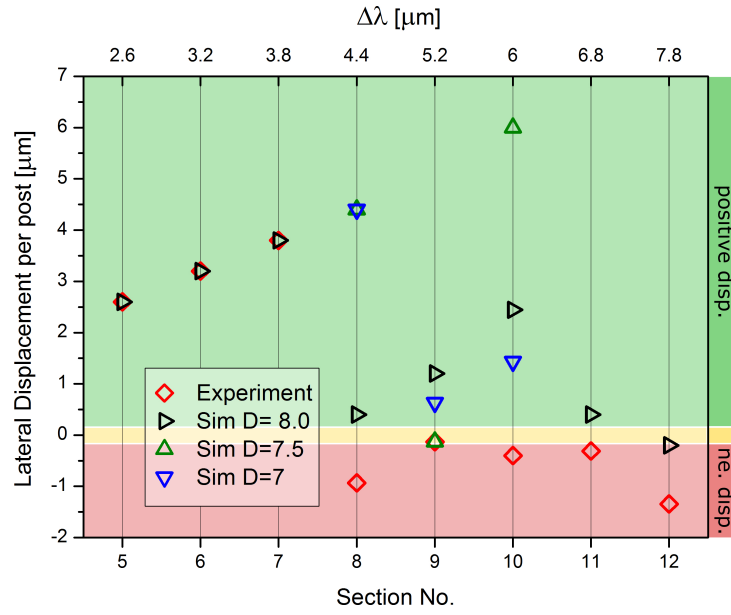


Figure 5.8: The average lateral displacement per post encounter  $l$  for individual sections of the thin device. Several RBC diameters were considered to confirm that the later sections of the thin device are quite sensitive to moderate changes in the RBC size. Several sets of simulation results for the RBCs with diameters 7, 7.5 and 8  $\mu\text{m}$  are shown. Figures source with permission from [140].

Finally, the simulation results for RBC size variation also illustrate the importance of simulation techniques in DLD device design; enabling a confident investigation into device sensitivity to RBC properties which are hard to measure and consistently manipulate in a lab setting, such as a variable cell size.

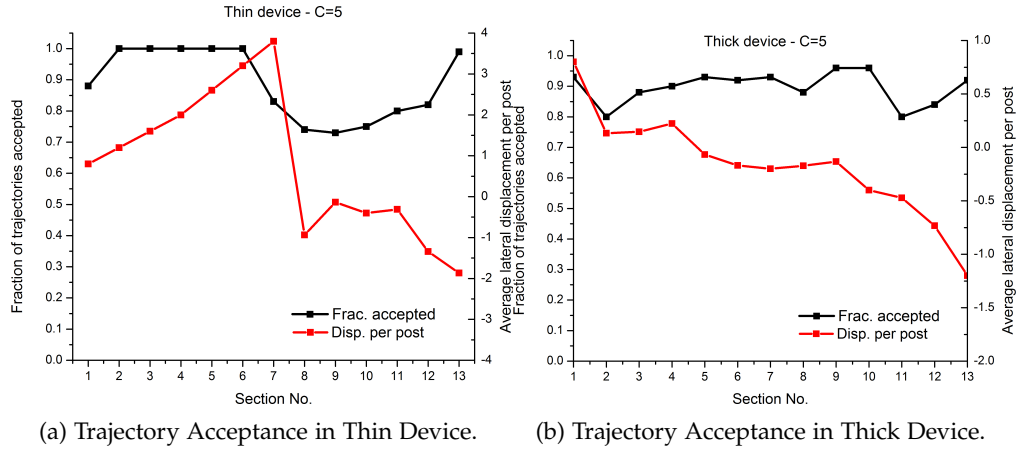


Figure 5.9: The fraction of RBC trajectories accepted for each device section after data pre-processing compared with the average lateral displacement per post. (a) The fraction of trajectories accepted in each section of the thin device at  $C = 5$ . Note dip in the acceptance fraction corresponding to the transition from displacement to zigzag in sections 7-11 of the device. Note that the acceptance fractions for sections 2-6 are taken as 1 because the displacement-mode transit was evident from simple analysis of videos by eye. (b) The fraction of trajectories accepted in each section of the thick device at  $C = 5$ . Note dips in the acceptance fraction that correspond to the transition from displacement modes to zigzag modes and in later sections indicating an increase in transit mode sensitivity (as shown in 5.5). Figures source with permission from [140].

#### *Viscosity-contrast-based sorting*

The viscosity contrast between the intra- and extra-cellular fluids used in the simulations and experiments discussed so far is close to the value of  $C = \eta_i/\eta_o = 5$  for physiological conditions in real blood. However, viscosity contrast is well established as a vital factor in determining RBC dynamics in shear flow, and as its value increases a transition from tank-treading to tumbling dynamics occurs [143, 144]. Consequently, altering the viscosity contrast demonstrates the importance of RBC dynamics within the device when attempting to use DLD as a technique for RBC separation. In addition to viscosity contrast  $C = 5$  between the intra- and extra-cellular fluids, simulations and experiments were carried out at  $C = 1$  and  $C = 0.25$  for the thick device, and  $C = 2$  for the thin device. Note that the different choices of  $C$  for thick and thin devices are due to the pronounced adsorption of RBCs in the confined environment of the thin device when adding a dextran solute at concentrations sufficient to yield a contrast below  $C = 2$ . The lateral displacements per post of the trajectories under these additional viscosity contrast conditions are shown in figures 5.6b and 5.7b. Simulations were first used to predict the sections which should display interesting behaviour, and these sections were then investigated experimentally in order to validate results. For both  $C = 1$  and  $C = 0.25$  in sections 1-4 of the thick device, the change in viscosity contrast com-

pletely inhibits lane-swapping events. This substantial shift from behaviour observed in the physiological case of  $C = 5$  may be attributed to a change in RBC dynamics and is discussed later. In subsequent device sections, there is a transition to approximately neutral zigzag modes, with a gradually increasing tendency to adopt an average negative lateral displacement towards the latter sections of the device. In the device sections after the transition, zigzag modes at  $C = 0.25$  are slightly more positive than those for the  $C = 1$ , but the  $l$  values for both cases converge in the last two sections of the device. This suggests a small difference in dynamic behaviour which is only relevant in deciding the lane swapping frequency in the middle sections of the device. Generally, good agreement is observed between experimental and simulated results and the main differences occur in the later sections of the device, which are attributed to a distortion of the flow field in close proximity to the device outlet. The difference between the trajectories in the early sections at viscosity contrast  $C = 5$  compared with those at  $C = 1$  and  $C = 0.25$  demonstrates the importance of viscosity contrast for RBC sorting since it can dramatically alter the transit modes.

Figure 5.7b shows that viscosity contrast also plays an important role in the transit of RBCs through the thin device. For a viscosity contrast of  $C = 1$ , the simulated RBC trajectories undergo a transition from the displacement mode to zigzag mode only at section 10, while for  $C = 5$  the transition occurs earlier, at section 8. Additionally, for the intermediate viscosity contrasts of  $C = 2$ , the transition to zigzag modes occurs in the same section as for  $C = 5$ . Well defined zigzag modes follow the transition, with a region of positive zigzag modes in sections 8-10. The  $l$  values in sections 8-10 are more positive than for the physiological contrast  $C = 5$ , and indicate an intermediate behaviour which is between the  $C = 5$  and simulated  $C = 1$  cases. Generally, good agreement is found between simulated and experimental results in the sections where RBCs are in a displacement mode. After the transition to the zigzag modes, deviations between the simulated and experimental cases occur. However, these can again be explained by the potential effects of RBC size variations which were already explored in figure 5.8. These results suggest that changes in RBC dynamics and deformation are still relevant in the thin device and that their effects manifest as a shift in the displacement to zigzag mode transition; and as differences in the average lateral displacement per post once the zigzag modes are established. Generally, the results confirm that the viscosity contrast can be used as a targeted separation parameter on its own, without other changes in RBC properties.

#### *RBC dynamics in DLDs*

The dependence of the transit modes of RBCs traveling through DLD obstacle arrays on viscosity contrast has revealed the importance of RBC dynamics. Single RBCs in shear flow have been shown experimentally to tumble at low shear rates and tank-tread at

high shear rates [141, 142, 145, 146]. Note that each of these experiments have been performed under the conditions where the viscosity of suspending media was larger than that of the RBC cytosol  $\eta_o > \eta_i$ . However, recent experiments [143] and simulations [144] indicate that the physiological viscosity contrast of  $C = \eta_i/\eta_o = 5$  suppresses the tank-treading motion of RBCs, leading to the preference for RBC tumbling. In case of  $C \lesssim 2 - 3$ , RBC membrane tank-treading is possible and the transition between tumbling and tank-treading for an increasing shear rate is attributed to the existence of a RBC minimum energy state, related to the weakly anisotropic shape of the spectrin network, such that the RBC has to exceed a certain energy barrier in order to transit to the tank-treading motion [146]. Moreover, recent shear-flow experiments [142] have identified another dynamic state, RBC rolling, which occurs within the range of shear rates between RBC tumbling and tank-treading states.

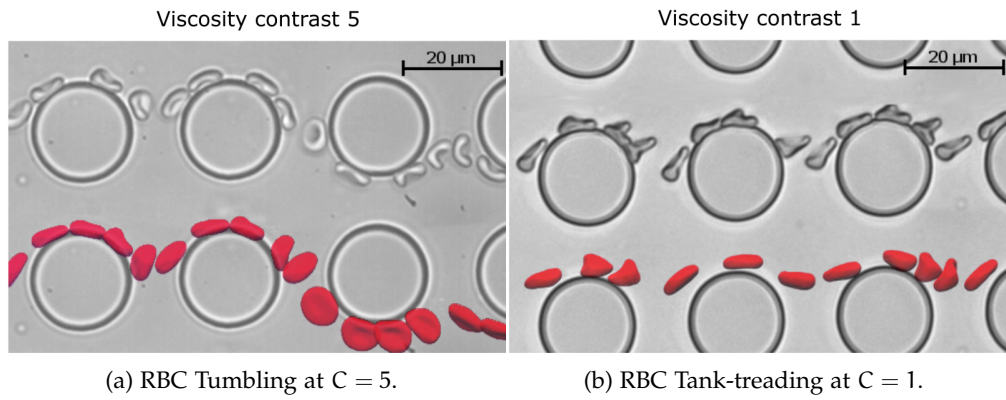


Figure 5.10: Stroboscopic images demonstrating different RBC dynamics in section 2 of the thick device, taken from simulations and experiments. (a) RBC lane swapping is promoted by tumbling when  $C = \eta_i/\eta_o = 5$ . (b) Tank-treading type dynamics occur at  $C = 1$  and the RBC favours the displacement mode. Figures source with permission from [140].

The main difference in RBC dynamics for the cases of  $C = 0.25 - 1$  and  $C = 5$  is the preference of tank-treading motion and tumbling dynamics, respectively. Figure 5.10 shows snapshots of simulated and experimentally observed RBCs in section 2 of the thick device at viscosity contracts  $C = 1$  and  $C = 5$ . In addition to demonstrating the accuracy of the simulated RBC dynamics in comparison to the corresponding experimental data, figure 5.10 shows the preferred transit modes of RBCs exhibiting different dynamic behaviour. The tumbling and rolling motion, which occurs at the physiological viscosity contrast, favour a zigzag transit mode. In contrast, the tank-treading dynamics at viscosity contrast  $C = 1$  noticeably inhibits lane swapping and the membrane deforms considerably (see trilobe RBC shapes in figure 5.10b) due to the shear forces experienced in the local vicinity of obstacles. Also, similar to observations made for 2D simulations of RBCs in chapter 4, figure 5.10a demonstrates that RBC tumbling motions directly precede and follow lane-swapping events, indicating



that tumbling dynamics play an important role in determining the lane-swapping frequency of zigzag modes. In comparison to the tumbling motion, the tank-treading RBC seen in figure 5.10b is subject to local shear-flow alignment, which suppresses cell tumbling and therefore, swapping of lanes. This fact is consistent with the simulation data in figure 5.6, where the transition to zigzag modes occurs at a later section for  $C = 1$  and  $C = 0.25$  in comparison with  $C = 5$ . The results for  $C = 0.25$  and  $C = 1$  are very similar, however this seeming contradiction can be attributed to the fact that the only difference in RBC dynamics is an increase in the frequency of tank-treading at  $C = 0.25$  due to the reduced internal viscosity. This minor change in dynamics is reflected in the minor changes in  $l$  values between the two cases, and is in stark contrast to the severe change in  $l$  values that arise from the transition between tumbling to tank-treading dynamics.

Another important aspect which influences the transit of RBCs through DLD devices is related to hydrodynamic interactions of deformable particles with walls and obstacles. It is well known that deformable particles (including RBCs) in flow near a wall are subject to a lift force driving them away from the wall [108, 139, 147]. Even though the lift force would depend on particle properties (e.g., rigidity, viscosity contrast) and its dynamics (e.g., tank-treading or tumbling, inclination angle), it is well established that lift force is stronger on a tank-treading RBC in comparison to a tumbling cell. Thus, the lift force on a RBC from the pillars in the thick device may inhibit the transition to zig-zag modes in early sections for  $C = 1$  and  $C = 0.25$  in comparison with  $C = 5$ .

## 5.5 SUMMARY

This chapter has presented a detailed comparison of experimental and 3D simulated results for the transit of RBCs through chirped DLD devices under various conditions. The behaviour of RBCs in DLD sorting devices differs from that of rigid spheres in two key ways. The first distinction lies with the additional transit modes available to RBCs compared to rigid spheres. The new transit modes are due to the complex interplay between hydrodynamic interactions with obstacles (such as lift force), and the RBC deformations and dynamics. The second distinction follows directly from the first: given that an RBCs dynamic behaviour and deformation depends on physical properties such as viscosity contrast and membrane rigidity, changes to these properties will result in transitions between different transit modes in DLD devices. For instance, the preference for tumbling motion at a viscosity contrast of  $C = 5$  promotes a transition from the displacement mode to the zigzag mode in section 2 of the thick device. Conversely, the tank-treading motion preferred by RBCs at a contrast of  $C = 1$  and  $C = 0.25$  delays the transition from the displacement to the zigzag mode to section 5 of the same device. The main differences between the two viscosity contrast cases arises from a well-documented hydrodynamic interaction that occurs between cells

and wall in close proximity called the lift force [108, 139, 147]. Lift forces are stronger for tank-treading cells than for cell performing tumbling dynamics, and tank-treading RBCs are pushed away from DLD posts causing a delayed transition to zigzag mode transit. Note that the lift force is not present for rigid spheres when inertial effects are negligible and the Reynolds number is nearly zero, as is the case in the experiments and simulations in this work.

The results for thick devices, which allow complete freedom in RBC orientation, show excellent quantitative agreement between simulations and experiments at a viscosity contrast of  $C = 5$ . In the case of viscosity contrasts  $C = 1 - 0.25$ , changes in RBC dynamics to tank-treading motions inhibited lane-swapping events in early sections of the device. Simulations of the thin device at viscosity contrast  $C = 5 - 2$  also display good quantitative agreement within the first 7 sections of the device, where RBCs moved in a displacement mode. The discrepancies observed between experiment and simulation following the transition to the zigzag modes in sections 8 and onwards are attributed to the inherent size distribution of RBC populations, a characteristic which the thin device is more sensitive to. Changing the simulated RBC size to values within the accepted range of experimentally observed RBC sizes or altering the viscosity contrast significantly changes the average lateral displacement per post  $l$  of RBCs in sections 8-10. Additionally, simulations at a viscosity contrast of  $C = 1$  in the thin device show an inhibition of lane swapping when compared to the  $C = 5$  or  $C = 2$  cases, similar to observations made for the thick device, as the transition to zigzag modes shifts from section 8 to section 10 of the device.

Based on observations made throughout this chapter, several suggestion for DLD device design and optimization can be made, in addition to possible novel sorting schemes. Foremost, the neutral zigzag mode and perfect displacement modes make up a small fraction of the available cell transit modes. Consequently, in order to design optimal chirped DLD devices for cell sorting, it is necessary to consider the net displacement arising from a range of negative, neutral and positive transit modes. The results for different viscosity contrast suggest that careful selection of the suspending medium will allow for sorting based on the viscosity of suspended particles intracellular fluid. A viscosity based sorting scheme would be best suited to the thick device, which allows exploration of the full range of dynamic behaviours induced by viscosity contrast. For instance two types of particle which are identical in all but their internal viscosity could be sorted by choosing a suspending medium with a viscosity such that each particle displays different dynamic behaviours, which in turn favour different transit modes.

An additional potential sorting scheme for DLD devices is elasticity based sorting, which has seen some interest in recent experiments [72]. Based on the present knowledge on RBC dynamics in shear flow [141–143, 146], it is possible that DLD devices could be well suited for sorting particles based on their elastic properties. This is of particular interest as diseases such as malaria are known to alter the mechanical prop-

erties of RBCs. In these DLD devices, transitions between tank-treading, rolling and tumbling could be exploited [142]. However, transitions appear to be suppressed by high viscosity contrasts [143, 144], which are dominated by tumbling dynamics. Therefore, elasticity based cell sorting in thick devices would be best suited to viscosity contrasts of  $C \leq 2 - 3$ .

In theory, elasticity based sorting of RBCs should also be possible in the thin DLD device. Simulation results in figure 5.7 demonstrate differences in the transit behaviour of RBCs at viscosity contrasts of  $C = 2 - 5$  and  $C = 1$  in the later sections of the device. The differences must arise from varying degrees of RBC deformation in flow which occur due to the differences in internal fluid viscosity. Furthermore, the later sections of the thin device have proven very sensitive to slight changes in effective RBC size, which may occur due to cell deformation in flow. Unfortunately, as seen in figure 5.8, the trajectories of RBCs in the section immediately after the zigzag mode transition are somewhat unreliable due to the inherent variability in RBC sizes, so it is unlikely that such a device would be able to distinguish between minor changes in size and minor changes in deformability. The effect of deformations has recently been illustrated in a simulation study by Krüger *et al.* [148], where the effect of flow rate on the transit mode of RBCs in a similar thin device has been explored. As the flow rate is increased in the device, so too does the deformation of the RBCs, leading to a change from the displacement mode to the zigzag mode. This highlights that the flow rate must also be tuned correctly in devices hoping to separate deformable cells based on their mechanical properties and dynamic behaviour. Returning to the traditional concept of size-based sorting, the thin device suppresses the variability in RBC dynamics and is thus more sensitive to variations in cell size. As such, thin chirped DLD devices seem to best suited for the task of sorting RBCs based on size.

As discussed previously in this work, the empirical relation between device geometry and critical size of rigid spherical particles allows reliable prediction of their trajectories through DLD devices using equation 3.7 [133, 149]. The simpler picture for rigid sphere relies on there being only two possible transit modes, the neutral zigzag mode and the displacement mode, and the fact that a particle's preference for each depends solely on its size relative to the characteristic critical size of the post array geometry. However, as demonstrated in this chapter; the transitions between displacement, neutral zigzag, and non-neutral zigzag modes are much harder to predict. This is because the transitions are dependant on several additional variables such as particle elasticity, viscosity contrast, and flow rate. Consequently, the development of a simple empirical relation which encompasses all of these variables seems highly unlikely. Additionally, any simplification of the models used in this work (e.g. omission of certain cell properties) would prevent predictive results for RBC transit in DLDs. It is vital to use reliable fluid simulation techniques which properly include hydrodynamic interactions, and particle models which accurately describe the mechanical properties of cells (i.e. elasticity, viscosity ratio and cell morphology).

In conclusion, this chapter demonstrates that a complex interplay between the dynamic behaviour of deformable particles and the hydrodynamic interactions they experience near obstacles give rise to a far richer behaviour in DLD devices than seen for rigid spherical particles. Whilst the behaviour is more complex, it is important to stress that transit modes do not occur randomly and are still deterministic in nature, and are determined by fluid flow and the mechanical properties of the deformable particle in question. Furthermore, the combination of quantitatively accurate simulations and experimental methods is demonstrably a powerful tool for designing novel sorting schemes that utilise the dynamic behaviour and intrinsic mechanical characteristics of bioparticles as separation parameters or biomarkers. Such sorting schemes are not limited to blood related diseases and disorders like malaria and sickle-cell anaemia, but could also find application in areas such as bacteriology, parasitology, and oncology. Finally, this chapter demonstrates the importance of reliable predictive simulation approaches for the development of purpose-specific microdevices, as simulations are able to provide a better understanding of dynamic behaviour of bioparticles in microfluidics and could lead to significant design optimizations.

## 6.1 INTRODUCTION

The work presented within this chapter ties together the findings in the previous two chapters 4 and 5 in order to address the issue of deformability based sorting which, as identified in section 1.2, is highly relevant for the diagnosis of malaria from human blood samples. Numerous experimental studies identify that RBCs infected by *plasmodium falciparum* undergo mechanical changes through the erythrocytic stage of the parasite's life-cycle [23, 29, 150, 151]. In the early stages of the parasite life-cycle, RBCs have not yet adhered to the endothelium of the cardiovascular system and are consequently present in blood samples taken from patients. However, malaria parasitemia is often very low during the early stages of infection and a DLD device capable of isolating infected RBCs due to the changes in their physical properties would greatly increase the chances of successful diagnosis. Furthermore, the mechanical properties of RBCs are only slightly altered in the early stages of the *plasmodium falciparum* infection. Indeed, experiments show that the RBC shear modulus increases from a healthy value of  $\mu_0 \approx 6\mu\text{N/m}$  to  $\mu_0 \approx 8 - 16\mu\text{N/m}$  for ring-stage RBCs, depending on the experimental method used [150, 151]. Consequently, a deformability based DLD device for malaria diagnosis needs to be sensitive to relatively small changes in the mechanical properties of RBCs.

The DLD array design investigated in this chapter is motivated by several findings from the previous chapters:

- i The behaviour of RBCs in DLD arrays with different post shapes explored in chapter 4 reveals that RBCs have different effective sizes in different post-shaped arrays, indicating that RBC deformation depends on post shape.
- ii Thin devices investigated in chapter 5 are very sensitive to the inherent size variations in RBC populations. Hence, changes in RBC motion within thin DLD devices due to slight variations in RBC mechanical properties would be blurred by the inherent variability in RBC size.
- iii Viscosity contrast is shown to strongly influence RBC transit through DLD devices in 5. Consequently a viscosity contrast of  $C = 1$  should be used to ensure that cell behaviour is not dominated by viscous effects.
- iv Finally, chapter 5 shows that dynamic behaviour strongly influences RBC transit, bringing the opportunity to induce deformability based separation in flow regimes

where RBCs with different mechanical properties undergo different dynamic motion.

Considering these observations, the device explored in this chapter consists of triangular shaped posts in a thick channel. The triangular shape is selected, as it is reasonable to assume that RBCs in flow near posts will experience strong deformations when they interact with triangles' upper most vertices. Furthermore, viscosity contrast is kept at  $C = 1$  to ensure that the devices probe deformability and not viscous effects. Two mechanical properties pertaining to RBC deformation are considered: shear modulus  $\mu_0$  and bending rigidity  $k_b$ . Additionally, two different flow speeds are investigated. The first flow rate is chosen such that all cells undergo roughly similar dynamic motion, hence all differences in RBC trajectories can be attributed explicitly to deformations which occur upon interaction with the posts and flow field. The second flow rate is chosen such that cells with slightly different mechanical properties undergo different dynamic behaviours, facilitating separation via deformability induced changes in RBC dynamics.

## 6.2 SIMULATION SETUP

The fluid and membrane models used in the 3D simulations presented in this chapter are identical to those used in the previous chapter 5. However, a range of values for certain RBC model parameters are used to simulate unhealthy RBCs. Specifically, a range of RBC membrane bending rigidities  $k_b$  and shear moduli  $\mu_0$  are considered to simulate the possible mechanical properties of RBCs in pathological states:  $k_b^u = 0.5-4k_b^h$  and  $\mu_0^u = 0.5-4\mu_0^h$ , where superscripts u and h refer to unhealthy and healthy cell states respectively.

The obstacle array investigated in this chapter is simulated using the same methodology for boundary conditions as in chapter 5; with impenetrable non-slip planes and frozen wall particles to represent the roof, floor, and post faces. The posts which make up the obstacle array have a triangular cross section, as shown in figure 6.1a, and figure 6.1b shows an example flow field induced the triangular post array with row shift  $\Delta\lambda = 2.6\mu\text{m}$ . The triangular posts have a base width and height of  $D_H = D_W = 15\mu\text{m}$  and each vertex is cut, resulting in three additional faces of width  $1\mu\text{m}$  at each corner of the triangle (see figure 6.1a). Consequently, the post cross section is formally described as an irregular hexagon. However, the shape is referred to as triangular throughout this work because the purpose of the vertex cuts is to mimic the shape of triangular posts in real-world microfluidic devices which are subject to fabrication limits. Additionally, the inter-post spacing in the obstacle array is anisotropic, with horizontal and vertical gaps between posts of  $G_H = 6\mu\text{m}$  and  $G_V = 10\mu\text{m}$ , respectively. The anisotropic spacing is motivated by experimental work by Zemin *et al.* which demonstrates that asymmetrical gap sizes increase the resolution of RBC separation in DLD devices [152]. Finally,

the height of the microfluidic channel is the same as in the thick device considered in chapter 5 with  $H = 11.0\mu\text{m}$ , allowing a full range of RBC dynamic motion.

The flow rate in DLD devices intended for deformability based sorting is especially important because it is known to strongly effect the dynamic behaviour of RBCs in confined channels [99, 103]. The flow between vertically adjacent triangles is characterized by a non-dimensional shear rate

$$\dot{\gamma}^* = \tau \bar{\gamma} \quad (6.1)$$

where  $\tau$  is the characteristic RBC relaxation time introduced in equation 4.1 and  $\bar{\gamma} = \bar{v}/G_V$  is the average shear rate; where  $\bar{v} = Q/(G_V H)$  is the average flow velocity between adjacent posts, and  $Q$  is the volumetric fluid flow rate through the device.

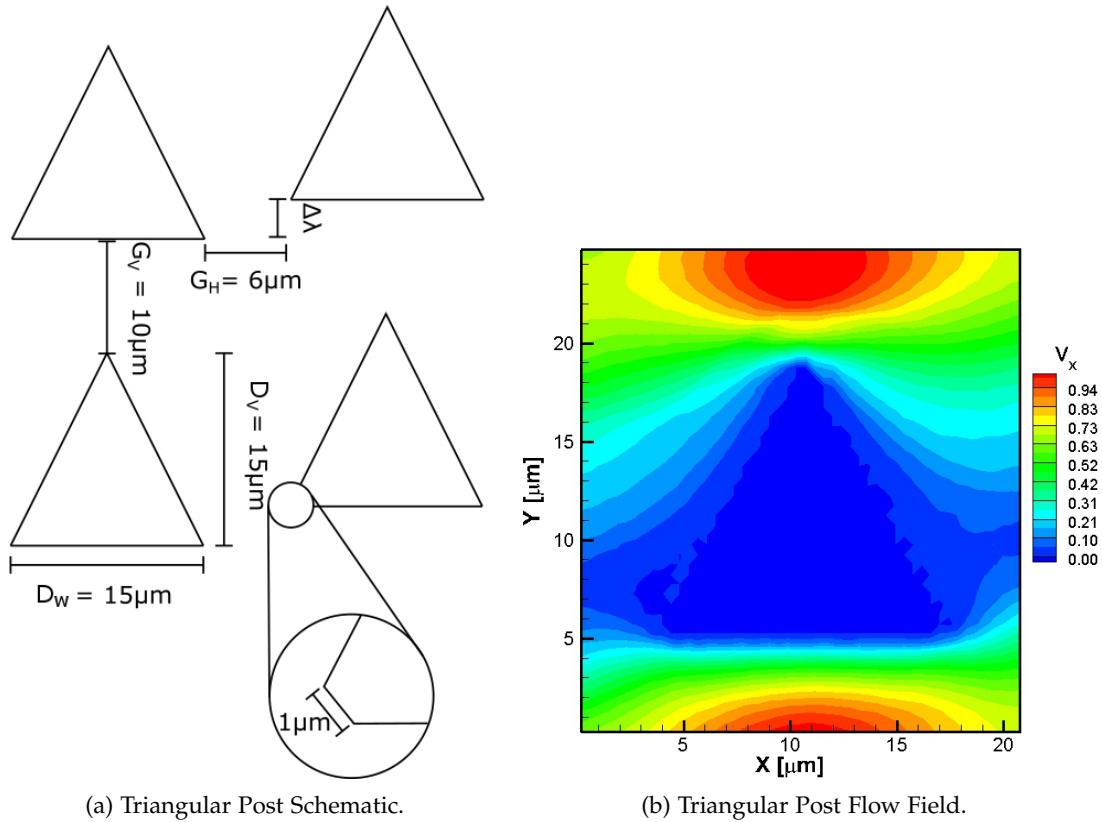


Figure 6.1: (a). A schematic of the triangular post-shaped array used in the simulations. With anisotropic spacing  $G_V = 10\mu\text{m}$  and  $G_H = 6\mu\text{m}$ . Note that a each vertex is cut such that there are three small  $1\mu\text{m}$  faces at the triangle vertices, this is to simulate device fabrication limits which prevent perfectly sharp vertices. (b) A colour map of the simulated flow field around a triangular post in an obstacle array with  $\Delta\lambda = 2.6\mu\text{m}$ . The colour map represents the fluid velocity in the x direction.

### 6.3 RESULTS

The initial investigation of deformability based sorting presented in this chapter considers the explicit effects of RBC membrane properties on cell sorting within a triangular pillar array. That is to say, sorting which is driven by the degree of RBC deformation that occurs when cells interact directly with triangular posts. Note, this type of sorting does not intend to utilise changes in RBC dynamic behaviour to drive sorting, as was demonstrated in chapter 5; where viscosity contrast was used to induce changes in RBC dynamics thereby facilitating sorting. Consequently, a value of  $\dot{\gamma}^* = 105$  is used for in the initial simulations in this chapter, as the corresponding flow rate puts all the pathological simulated RBCs in roughly the same dynamic regime. Thus, differences in the transit modes of unhealthy RBCs vs. healthy RBCs in the triangular post array can predominantly be attributed to changes in RBC membrane deformation.

The last set of simulation results presented in this chapter use a dimensionless shear rate of  $\dot{\gamma}^* = 13$ . In this flow regime, RBCs with different shear moduli are seen to undergo different dynamic motions and hence traverse the DLD array via different transit modes. In this case, the underlying reason for the differences in DLD transit modes of RBCs in pathological states is still their abnormal mechanical properties. However, it is changes in the dynamic behaviour of cells with different shear moduli which drives the lateral separation of RBCs when  $\dot{\gamma}^* = 13$ .

#### *Bending Rigidity Based Sorting*

The average lateral displacement per post encounter  $l$  for RBCs with varying values of bending rigidity  $k_b$  in triangular post arrays with different row shifts  $\Delta\lambda$  is shown in figure 6.2. At bending rigidities of  $k_b^h$  and  $k_b^u = 0.5k_b^h$ , RBCs move in positive displacement modes until the row shift increases to  $\Delta\lambda = 2.6\mu\text{m}$ , and a gradual transition to positive zigzag modes occurs for higher values of  $\Delta\lambda$ . RBCs with higher rigidities of  $k_b^u = 2 - 4k_b^h$  under go the transition from positive displacement modes to positive zigzag modes at a larger row shift of  $\Delta\lambda = 2.7\mu\text{m}$ , indicating that rigid unhealthy RBCs have a larger effective size in the triangular post arrays than the healthy or less rigid RBCs.

The asphericities  $\delta$  of RBCs with different bending rigidities moving in DLD devices can also be divided into the same two groups: with healthy and less rigid RBCs displaying roughly identical asphericity distributions, and more rigid RBCs showing alike asphericity distributions. The asphericity distributions of RBCs moving in the displacement mode and positive zigzag modes through the triangular post arrays is shown in figure 6.3. All of the RBCs in the triangular post array with row shift  $\Delta\lambda = 2.4\mu\text{m}$  move via the displacement mode, and figure 6.3a demonstrates that healthy and less rigid RBCs have nearly identical asphericity distributions when travelling in the dis-



placement mode. However, the more rigid RBCs with  $k_b^u = 2 - 4k_b^h$  display slightly different asphericity distributions when in the displacement mode, with a tendency towards higher  $\delta$  values. The same pattern is seen for RBCs moving via the zigzag mode in the triangular post array with  $\Delta\lambda = 2.8\mu\text{m}$  in figure 6.3b; with healthy and less rigid RBCs showing approximately identical  $\delta$  distributions, and the more rigid RBCs showing a tendency for higher  $\delta$  values. Generally, the asphericity distribution widens when RBCs transition from the displacement mode to the zigzag mode, and higher values of  $\delta$  become more probable, indicating that RBCs experience stronger deformations when in the zigzag mode.

The changes in asphericity distributions seen between rigid and flexible RBCs in the triangular post arrays indicate that RBC deformation is responsible for the different transition values of  $\Delta\lambda = 2.6\mu\text{m}$  and  $\Delta\lambda = 2.7\mu\text{m}$ . The different shapes observed for RBCs with bending rigidities  $k_b^u = 0.5k_b^h$  and  $k_b^u = 0.5k_b^h$  travelling in the displacement mode are shown in figure 6.4. The snap shots are taken from the triangular array with  $\Delta\lambda = 2.5\mu\text{m}$ , which represents the last geometry in which all the RBCs move in the displacement mode. Given that the transition to the zigzag mode for the most flexible RBC occurs at  $\Delta\lambda = 2.6\mu\text{m}$ , and that the RBC bending rigidities differ by a factor of 8, it would be expected that observed RBC shapes would be noticeably different. However, figure 6.4 demonstrates that the RBCs are almost identical in shape, and the only obviously noticeable difference occurs immediately after RBCs move over the triangular post's upper vertex.

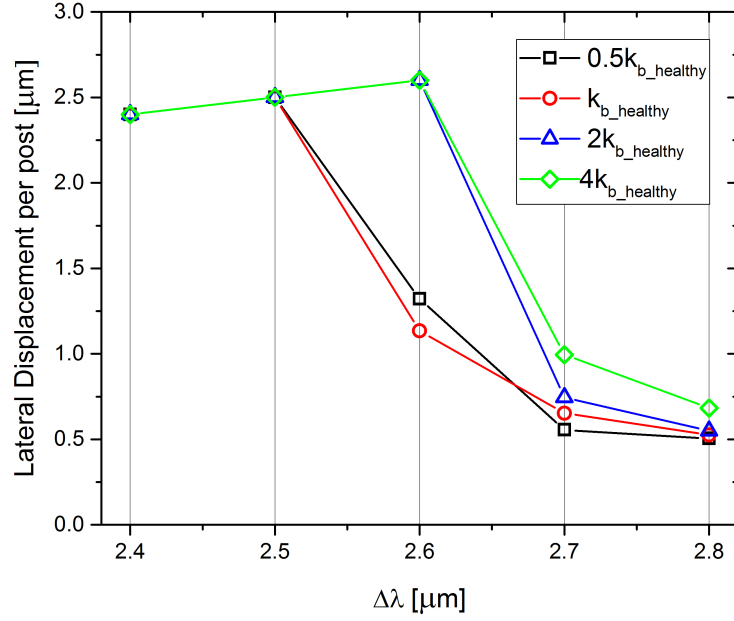


Figure 6.2: The average lateral displacement per post encounter  $l$  of RBCs with different unhealthy bending rigidities  $k_b$ . The transition from the displacement mode and zigzag mode occurs at different values of  $\Delta\lambda$  for RBCs with different  $k_b$  values. RBCs with  $k_b = 0.5k_{b\_healthy}$  are found to undergo show roughly the same behaviour as healthy RBCs; transitioning to the zigzag modes at a row shift of  $\Delta\lambda = 2.6\mu\text{m}$ . RBCs with higher bending rigidities of  $k_b = 2 - 4k_{b\_healthy}$  are found to undergo the transition to zigzag modes at a row shift of  $\Delta\lambda = 2.7\mu\text{m}$ . Note that the transition to zigzag motion is steep for rigid RBCs, while the less rigid and healthy RBCs move more gradually to the zigzag modes.

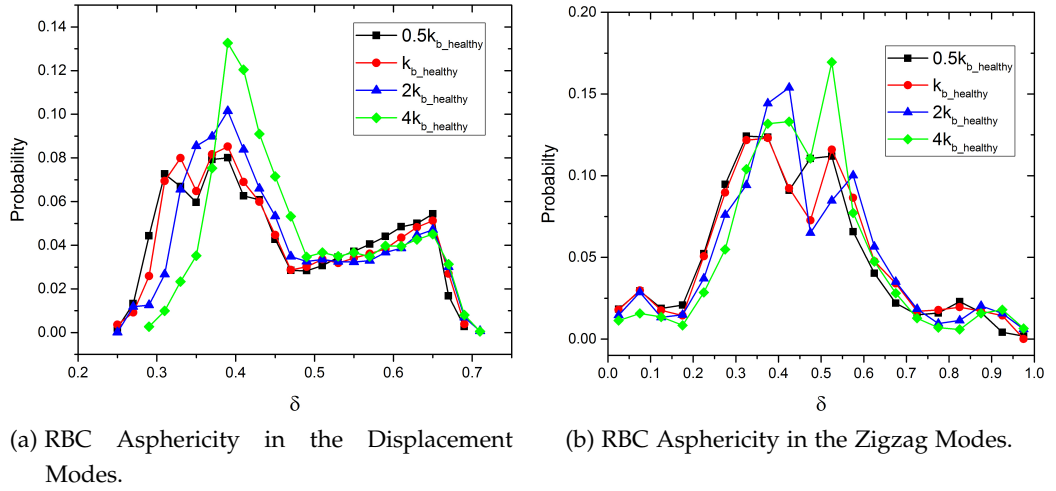


Figure 6.3: The asphericity  $\delta$  probability distributions for RBCs with different bending rigidities travelling in displacement modes and zigzag modes. (a) Shows the asphericity distributions for RBCs moving in the displacement mode in a triangular post array with  $\Delta\lambda = 2.4\mu\text{m}$ . (b) Displays the asphericity distribution for RBCs travelling in positive zigzag modes within a triangular post array with  $\Delta\lambda = 2.8\mu\text{m}$ .

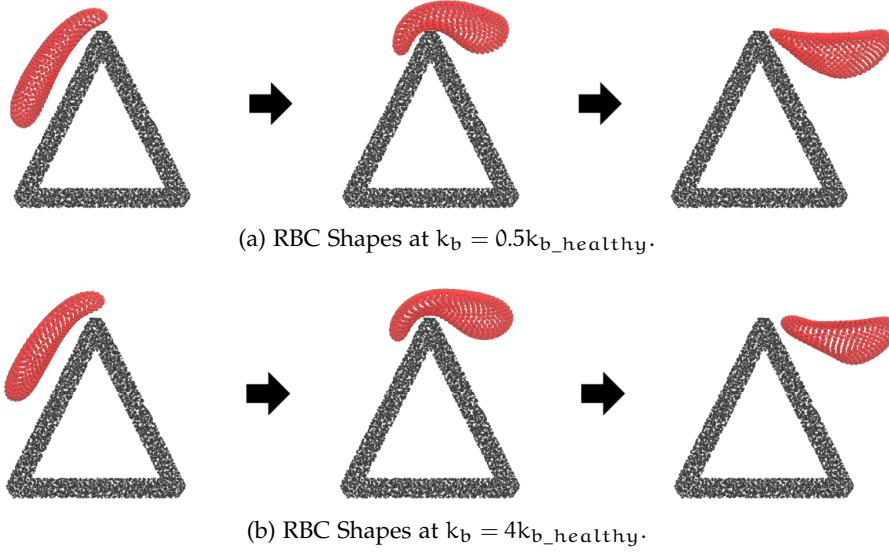


Figure 6.4: The deformed shapes of pathologically flexible and rigid RBCs in triangular post arrays. Snap shots of RBCs moving in the displacement mode in a post array with  $\Delta\lambda = 2.5\mu\text{m}$  are taken before, during, and immediately after interaction with a triangular post's upper most vertex. (a) Shows three snap shots of an RBC with  $k_b = 0.5k_b^h$  as it encounters a single post in a triangular post array. (b) Shows three snap shots of an RBC with  $k_b = 4k_b^h$  as it encounters a single post in the same triangular post array

### *Shear Modulus Based Sorting*

The transit modes of RBCs with pathological shear modulus values in the triangular post array is shown in figure 6.5. The results show that, as RBC shear modulus increases, the transition from the displacement mode to the zigzag mode occurs in array geometries with larger row shifts  $\Delta\lambda$ . Healthy RBCs and the softer RBCs with  $\mu_0 = 0.5\mu_0^h$  transition to zigzag motion at a row shift of  $\Delta\lambda = 2.5\mu\text{m}$ , and reach well established positive zigzag modes when  $\Delta\lambda = 2.7\mu\text{m}$ . The RBCs with a shear modulus of  $\mu_0 = 2\mu_0^h$  switch to the zigzag mode when  $\Delta\lambda = 2.7\mu\text{m}$ , and reach a well established neutral zigzag mode more rapidly than the softer RBCs. The fact that the softer cells and more rigid RBCs with  $\mu_0 = 2\mu_0^h$  undergo positive and neutral zigzag modes, respectively, indicates that RBCs with increased shear moduli can be separated from healthy RBCs even if all of the cells are in the zigzag mode. Finally, the most rigid RBC with  $\mu_0 = 4\mu_0^h$  travels in the displacement mode for all  $\Delta\lambda$  values explored in these simulations, indicating an increase in effective size compared to the softer RBCs. Generally the results show that RBCs with larger shear moduli transition to the zigzag mode at larger row shifts, suggesting that the effective size of RBCs in the triangular post arrays increases with  $\mu_0$ .

The asphericity distributions shown in figure 6.6 help to explain why the transition to zigzagging occurs for higher  $\Delta\lambda$  for more rigid RBCs. RBCs in the displacement mode show narrowing asphericity distributions for higher  $\mu_0$  values in figure 6.6a. Additionally, the average asphericity is seen to decrease for more rigid RBCs, indicating a larger effective size in the DLD obstacle array. Both of these observations indicate that triangular posts strongly probe the deformation properties of RBCs with different shear moduli. A similar trend is seen for RBCs in the zigzag mode in figure 6.6b, with even broader asphericity distributions for softer RBCs. Generally, a wider spectrum of asphericities is expected for RBCs in zigzag modes because they explore more of the flow field depicted in figure 6.1b and hence experience a wider range of shear rates compared to RBCs in the displacement mode.

The trends demonstrated by the asphericity distributions of RBCs in the displacement mode are reinforced by snap shots of RBCs with different shear modulus values interacting with triangles in a post array with  $\Delta\lambda = 2.5\mu\text{m}$ . The softest RBCs with  $\mu_0 = 0.5\mu_0^h$  are severely deformed as they are stretched over the triangles upper vertex. Note, the extreme elongated shape of the soft RBC as it breaks contact with the triangular post is expected to cause disruptions to fluid flow between the horizontal gaps in posts. This could explain why softer RBCs move in positive zigzag modes, while the more rigid RBCs with  $\mu_0 = 2\mu_0^h$  move in a neutral zigzag mode because they do not block vertical fluid flow between horizontally adjacent posts. The pictures of the most rigid RBC with  $\mu_0 = 4\mu_0^h$  in the displacement mode shows significantly reduced elongation in flow compared to the softer RBC. The reduction in stretching means that

more rigid RBCs are thicker as they pass over the triangle vertex, resulting in a larger effective size in triangular arrays and a delayed transition to zigzag motion.

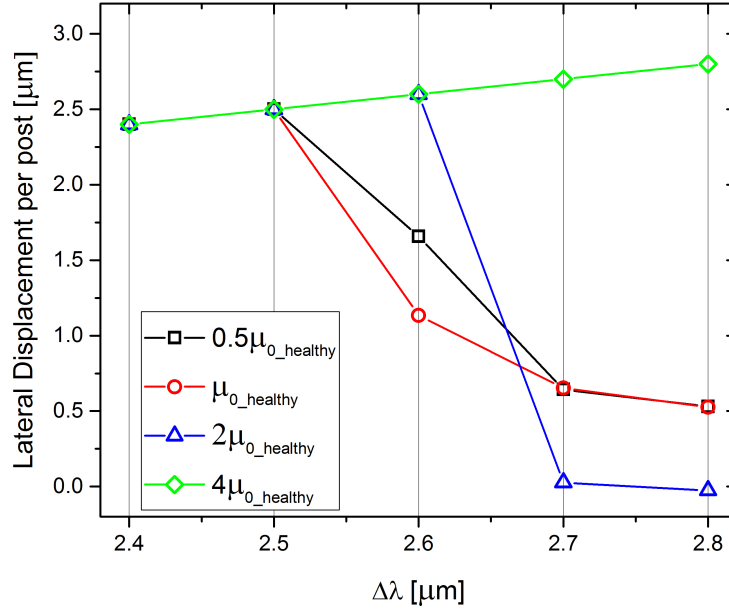


Figure 6.5: The average lateral displacement per post encounter  $l$  of RBCs with different unhealthy shear moduli  $\mu_0$ . The transition from the displacement mode and zigzag mode occurs at different values of  $\Delta\lambda$  for RBCs with different  $\mu_0$  values. RBCs with  $\mu_0 = 0.5\mu_{0\_healthy}$  are found to undergo show roughly the same behaviour as healthy RBCs; transitioning to positiv zigzag modes at a row shift of  $\Delta\lambda = 2.6\mu\text{m}$ . RBCs with  $\mu_0 = 2\mu_{0\_healthy}$  transition to a neutral zigzag mode when  $\Delta\lambda = 2.7\mu\text{m}$  and the most rigid RBCs with  $\mu_0 = 4\mu_{0\_healthy}$  remain in the displacement mode for all  $\Delta\lambda$  values.

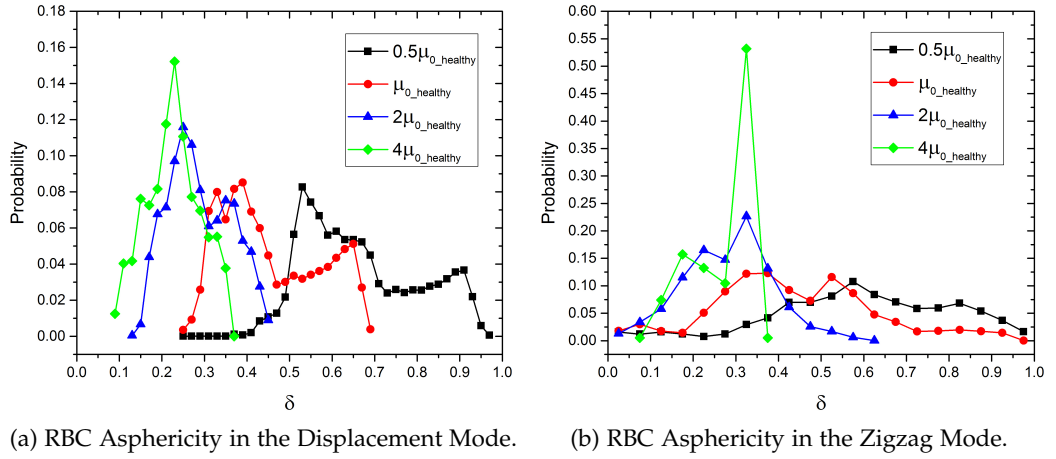


Figure 6.6: The asphericity  $\delta$  probability distributions for RBCs with different shear modulus values travelling in displacement modes and zigzag modes. (a) Shows the asphericity distributions for RBCs moving in the displacement mode in a triangular post array with  $\Delta\lambda = 2.4\mu\text{m}$ . (b) Displays the asphericity distribution for RBCs travelling in zigzag modes within a triangular post array with  $\Delta\lambda = 2.8\mu\text{m}$ .

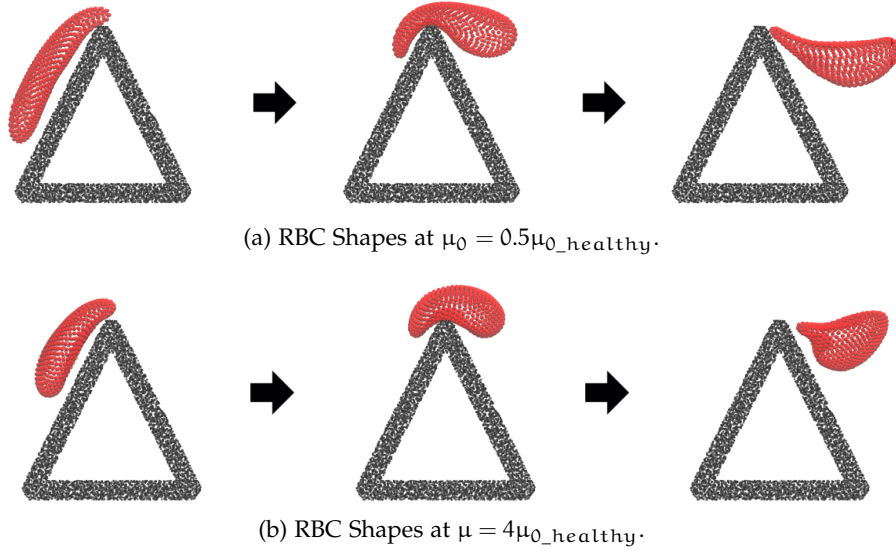


Figure 6.7: The deformed shapes of RBCs with pathological values for  $\mu_0$  in triangular post arrays. Snap shots of RBCs moving in the displacement mode in a post array with  $\Delta\lambda = 2.5\mu\text{m}$  are taken before, during, and immediately after interaction with a triangular post's upper most vertex. (a) Shows three snap shots of an RBC with  $\mu_0 = 0.5\mu_0^h$  as it encounters a single post in a triangular post array. (b) Shows three snap shots of an RBC with  $\mu_0 = 4\mu_0^h$  as it encounters a single post in the same triangular post array.

### *Incorporating Transitions in Dynamics*

The previous two sections investigated sorting RBCs with pathological values for  $k_b$  and  $u_0$  by directly probing their deformability in triangular post arrays. The results show that this sorting approach works in theory, and cells with different shear moduli or bending rigidities transitioned from the displacement transit mode to the zigzag transit mode at different row shifts  $\Delta\lambda$ . However, the differences between the transition row shifts is only 100nm, which is approaching the resolution limit of microfluidic fabrication techniques. Furthermore, the fact that such small changes in row shift are necessary to resolve the different transitions from displacement to zigzag mode indicates that the effective sizes of different pathological RBCs are only slightly different. In fact, it is likely that the inherent variations in RBC size will dominate the RBC trajectories in the triangular array when the dimensionless shear rate is  $\dot{\gamma}^* = 105$ .

This section attempts to demonstrate a more feasible deformability based sorting scheme by exploiting the fact that RBCs with different mechanical properties exhibit different dynamic behaviour for certain flow rates. Hence, the flow rate in the triangular post array is decreased in the following simulations, and is now characterized by a dimensionless shear rate  $\dot{\gamma}^* = 13$ , which is considerably smaller than the previous value of  $\dot{\gamma}^* = 105$ . The value  $\dot{\gamma}^* = 13$  is selected because work by Fedosov *et al.* [103] has demonstrated that RBCs in tube flow at similar confinements and shear rates exhibit different dynamic behaviours depending on their mechanical properties. For instance, a RBC with a higher shear modulus might undergo tumbling while a RBC with a lower shear modulus would exhibit tank treading behaviour. Consequently, it should be possible to sort RBCs with different shear moduli due to differences in their dynamic behaviour. This is the same as the principle explored in chapter 5, however in this case, RBC shear modulus  $\mu_0$  is used to control RBC dynamics instead of viscosity contrast  $C$ .

The lateral displacements per post encounter of RBCs driven by a flow rate characterized by  $\dot{\gamma}^* = 13$  is shown in figure 6.8. Contrary to the results shown in the previous section, RBCs with higher shear moduli transition from the displacement mode to the zigzag mode at lower values of  $\Delta\lambda$  compared to RBCs with lower shear moduli. Furthermore, much larger changes in row shift are able to resolve the transit mode transitions. For example, RBCs with a shear modulus of  $\mu_0 = 2\mu_0^h$  transition to the zigzag mode at a row shift of  $\Delta\lambda = 2.2\mu\text{m}$  and healthy RBCs transition to the zigzag mode at a row shift of  $\Delta\lambda = 2.6\mu\text{m}$ . These two values of row shift used for separation in the previous dimensionless shear rate  $\dot{\gamma}^* = 105$  would be unable to resolve any differences in the transitions between RBC transit modes.

The asphericity distributions of RBCs with different shear moduli are shown in figure 6.9. RBCs with different shear modulus values are seen to have very different asphericity distributions because they are in different dynamic behaviour regimes, which in turn are associated with various RBC shapes. This is to be distinguished from ob-

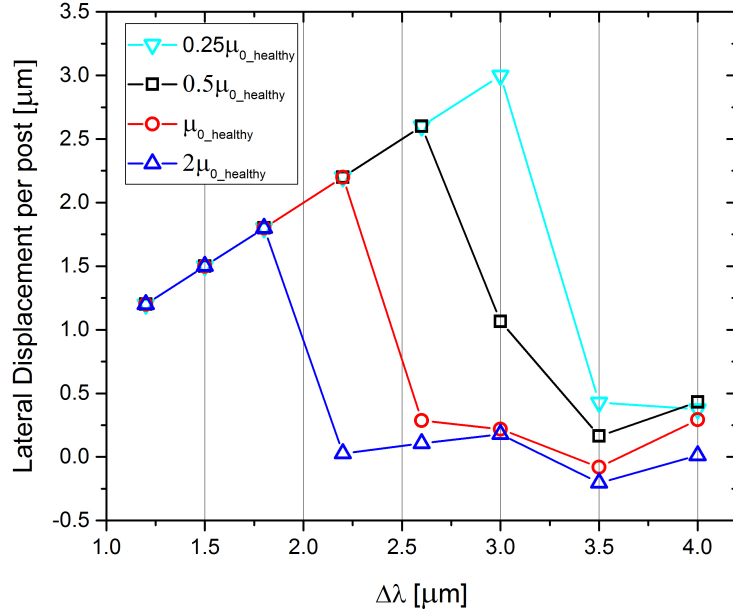


Figure 6.8: The average lateral displacement per post encounter  $l$  of RBCs with different unhealthy shear moduli  $\mu_0$ , transported in flow defined by  $\dot{\gamma}^* = 13$ . The transition from the displacement mode and zigzag mode occurs at different values of  $\Delta\lambda$  for RBCs with different  $\mu_0$  values. The transition from the displacement mode to the zigzag mode occurs at higher values of  $\Delta\lambda$  for RBCs with lower  $\mu_0$ .

servations in the previous section, where differences in asphericity distributions were attributed to the broadening or narrowing of the healthy RBC asphericity profile for more rigid and less rigid RBCs, respectively. The difference between the two cases is reinforced by considering the fact that, for both  $\dot{\gamma}^* = 13$  and  $\dot{\gamma}^* = 105$ , the stiffest and softest RBCs have the lowest and highest average asphericities, respectively. However, at when the shear rate is  $\dot{\gamma}^* = 13$  the stiffer cells transition to zigzagging before the softer cells, in direct contrast to the behaviour observed for the higher shear rate of  $\dot{\gamma}^* = 105$ .

The fact that RBCs with different shear moduli undergo different dynamic behaviours is demonstrated in figure 6.10, which shows the changing asphericities of RBCs as they travel past the triangular posts in the zigzag mode. It is clear that RBCs with shear modulus values of  $\mu_0 = 0.25\mu_0^h$  and  $\mu_0 = 2\mu_0^h$  display markedly different asphericities even when they are in a similar location relative to the triangular post. Furthermore, the RBC shapes observed at different locations around the triangular post are displayed in figure 6.10c. Notice that soft and rigid RBCs have dramatically different shapes when in the same location within the device, suggesting that they have different dynamic behaviours. This is in contrast to the relatively minor changes in RBC shapes seen in the previous section, where the differences in shape are attributed entirely to the degree of deformation caused by direct interaction with the triangular posts.



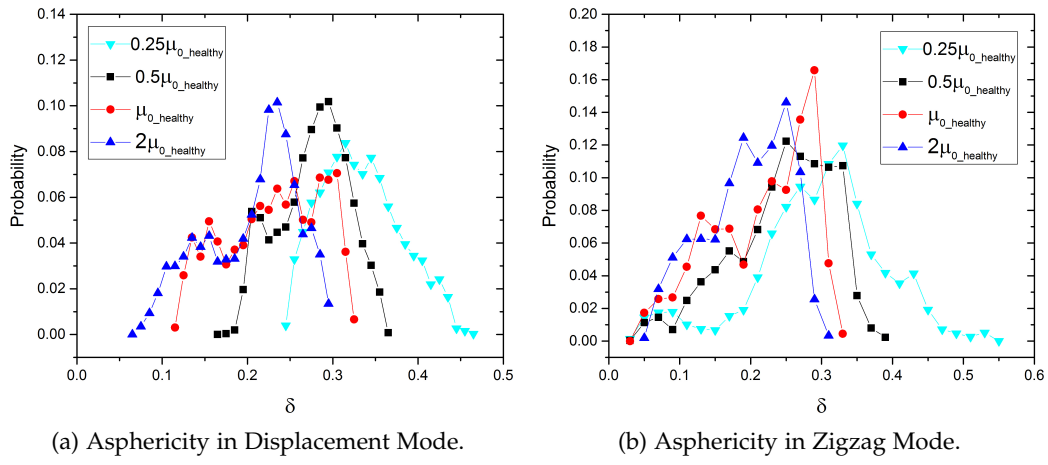
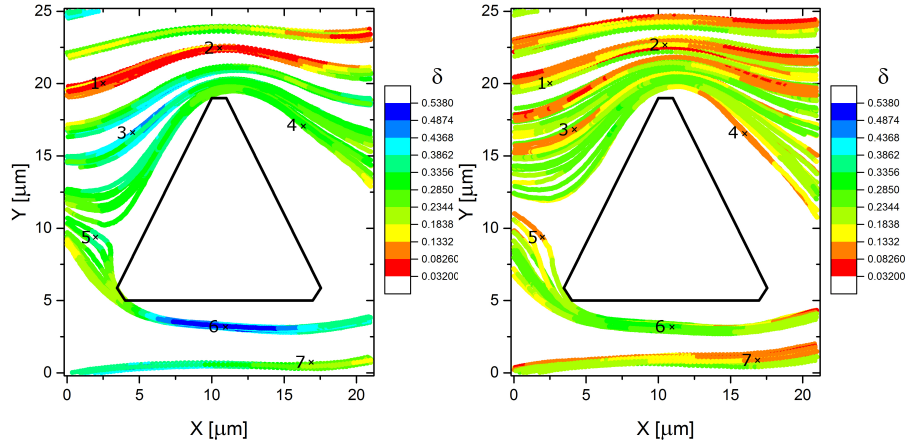
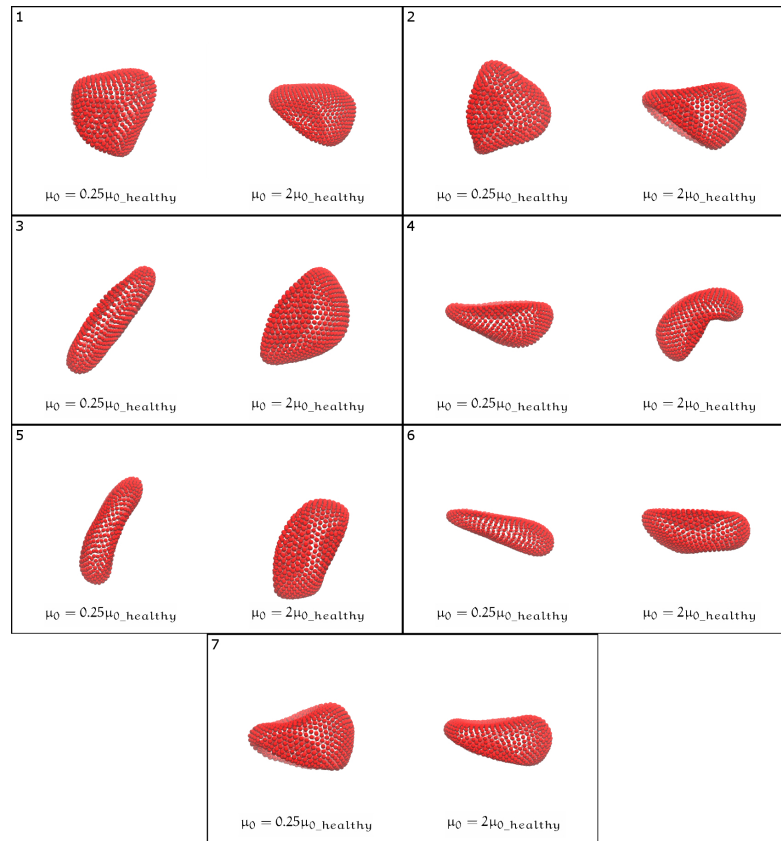


Figure 6.9: The asphericity  $\delta$  probability distributions for RBCs with different shear modulus values travelling in displacement modes and zigzag modes. (a) Shows the asphericity distributions for RBCs moving in the displacement mode in a triangular post array with  $\Delta\lambda = 1.2\mu\text{m}$ . (b) Displays the asphericity distribution for RBCs travelling in zigzag modes within a triangular post array with  $\Delta\lambda = 4.0\mu\text{m}$ .



(a) Asphericity for  $\mu_0 = 0.25\mu_{0\_healthy}$ . (b) Asphericity for  $\mu_0 = 2\mu_{0\_healthy}$



(c) RBC Shapes for Different  $\mu_0$

Figure 6.10: The different shapes and asphericities of RBCs undergoing different dynamic behaviours whilst in the zigzag mode in the triangular post array with row shift  $\Delta\lambda = 4.0$ . Key locations in the device where shape and asphericity are markedly different are identified by labels 1 – 7. (a) The different asphericities of RBCs with  $\mu_0 = 0.25\mu_{0\_healthy}$  in different locations around the triangular post. Where the colour map corresponds to the asphericity of an RBC with it's center of mass at a given point. (b). The different asphericities of RBCs with  $\mu_0 = 2\mu_{0\_healthy}$  in different locations around the triangular post. (c) Shows the different shapes observed for RBCs with  $\mu_0 = 0.25\mu_{0\_healthy}$  and  $\mu_0 = 2\mu_{0\_healthy}$  at seven different locations in the device. Note the locations are marked from 1 to 7 on the top figures.

## 6.4 SUMMARY

This chapter presented a potential DLD device design for sorting RBCs with pathological membrane rigidities and shear moduli. The obstacle array used triangular shaped posts to probe the deformability of cells and a floor-ceiling spacing of  $H = 11\mu\text{m}$  was used to ensure that a full range of RBC dynamic behaviours were possible. The initial simulations investigated the transit behaviour of RBCs with unhealthy values for  $k_b$  and  $\mu_0$  in a high flow rate such that all the RBCs displayed the same dynamic behaviour. This ensured that RBC separation resulted from differing severities of RBC deformation for different pathological cell states, and not because of different dynamic behaviours for pathological cells. Additionally, the simulations were all run at a viscosity contrast of  $C = 1$  to ensure that viscous effects do not dominate RBC transit through the triangular post arrays.

Simulations of RBCs with pathological values of  $k_b$  reveal that stiffer RBCs have slightly larger effective sizes in the triangular post array. Consequently, RBC with higher  $k_b$  values transition from the displacement mode to the zigzag mode at large values of  $\Delta\lambda$  compared the softer RBCs, which switch to the zigzag mode at smaller row shifts. Initially this trend indicates that bending rigidity based sorting is possible for high flow rates. However, the differences in effective size of RBCs with pathological  $k_b$  values are so small that the inherent size variability in RBC populations is expected to dominate the RBC transit behaviour. Simulations of RBCs with pathological values of  $\mu_0$  in the triangular post array display larger variations in shape than for pathological bending rigidities. Furthermore, RBCs with lower  $\mu_0$  values experience strong stretching as they travel over the triangular posts, while stiffer RBCs are stretched far less. However, even though the snap shots of RBCs in the obstacle array suggest that triangular posts are effective for probing RBC membrane shear modulus, ultimately the device does not seem sufficiently sensitive to shear modulus to offset the expected effects of inherent RBC size variations. Therefore, using a high flow rate to ensure uniform cell dynamics in the triangular post array is not an effective strategy for sorting based on changes in RBC membrane bending rigidity or shear modulus.

Considering the poor success of sorting based on explicit deformation of pathological RBCs as they interact with triangular post, the flow rate is reduced such that RBCs with different shear moduli exhibit different dynamic behaviours. Simulations of RBCs with pathological values of  $\mu_0$  in the triangular post array at the lower shear rate reveal that changes in RBC dynamic behaviour strongly effect the transit modes of RBCs in the device. RBCs with higher values of shear modulus are seen to undergo tumbling type behaviour which, as shown in the previous chapter, tend to prefer the zigzag mode. Conversely, RBCs with lower shear modulus values tend towards more tank-treading type behaviours which favour the displacement mode. Consequently, RBCs with higher shear moduli transition from the displacement mode the zigzag mode at higher row shifts  $\Delta\lambda$ . The exploitation of different RBC dynamic behaviours greatly

increases the sensitivity of the triangular array to small variations in RBC membrane shear modulus  $\mu_0$ . Therefore, the triangular post array operated at low flow rates shows promise as a device for diagnosing malaria, as RBC infection by the *plasmodium falciparum* parasite is known to increase the membrane shear modulus by a factor of 2 – 3 (comparable to the values considered in this study).

## CONCLUSION AND OUTLOOK

---

This thesis sets out to examine the sorting of particles in DLD devices using a combined numerical and experimental approach. A key aim is to rationalize the types of motion observed for different particle species as they traverse various configurations of DLD obstacle arrays and, in doing so, identify the preferable conditions for separating specific heterogeneous particle populations. This goal is achieved through 2D and 3D simulation approaches which employ coarse-grained mesoscopic models to represent fluid and a variety of particle types. Furthermore, supplementary experiments are performed throughout the work to corroborate simulation findings and test the feasibility of simulation based microfluidic design practises.

Particle sorting is highly relevant in many fields such as diagnostics, food and chemical processing, chemical and biological analyses, and environmental assessment. Deterministic lateral displacement is one of many of the passive label-free sorting techniques that have garnered interest since the development of microfluidic technologies in recent decades. Passive microfluidic sorting devices pose significant advantages over current industry standards such as FACS and MACS; with reduced costs, simpler operation, and improved portability. Moreover, the passive nature of DLD is especially advantageous, as particles are sorted in accordance with their intrinsic mechanical properties and there is no need for the particle labelling required in FACS or the application of external fields necessary in acoustophoresis and electrophoresis.

Many of the particles that require sorting are non-spherical and/or deformable, and only a small fraction can be thought of as rigid spherical beads. However, many of the current principles used to design DLD devices are rooted in theoretical predictions and experimental data for the behaviour of rigid spherical particles. This is primarily because sorting rigid beads represents the simplest case study for sorting in DLD devices. Indeed, the developed theories work exceedingly well, achieving separation of polystyrene beads of different size with a resolution of up to 10nm [6]. Nevertheless, rigid bead sorting is only directly applicable to a handful of real world applications and DLD devices designed to separate deformable non-spherical particles often rely on confinement to force behaviour comparable to that of rigid beads. This design approach squanders the full potential of passive label-free sorting, as particle size is just one of the many cell properties that could be used as a biomarker for separation.

To help DLD devices reach their full potential for sorting the myriad different particles types, this thesis aims to identify the key differences in motion between rigid spherical particles and deformable non-spherical particles in a range of DLD device configurations. Furthermore, the work identifies the mechanical processes and obsta-

cle array geometries which are responsible for the differences in motion; providing the ground work for informed design of future DLD devices able to separate non-spherical deformable particles via sorting criteria beyond that of size differentiation. Moreover, an example of informed DLD device design is presented, demonstrating a promising DLD configuration for deformability-based sorting of RBCs. Finally, in addition to deepening understanding of particle motion in DLD devices and motivating novel device designs, the work demonstrates the value of accurate simulation techniques within the field of microfluidics.

The main empirical findings are divided between three different chapters, 4, 5, and 6. Each chapter discusses their respective results in detail, in this chapter the main results are briefly summarised before the collective implications of the results are discussed. Chapter 4 presented results for 2D simulations of rigid spherical beads and deformable discocytes in DLD devices using the cell models presented in section 2.2.1 and the DPD fluid model described in section 2.1.1. Quantitative agreement is achieved between the simulations and empirically determined formula for rigid spherical beads in circular post arrays. This motivates the formulation of equivalent empirical formulae for DLD arrays with alternative post shapes using the same simulation method. Hence, new adaptations of equation 3.7 are realised for diamond-, square- and triangular-posts.

Following investigation of rigid beads, the 2D RBC model is used to identify the changes in motion for deformable particles with anisotropic dimensions. The results show that the effective size of RBCs in circular, diamond and square post arrays are found to be  $D_{\text{eff}} = 3.65 \pm 0.07\mu\text{m}$ ,  $2.65 \pm 0.14\mu\text{m}$ , and  $3.50 \pm 0.15\mu\text{m}$ , respectively, values which are in-between the maximum and minimum RBC dimensions of  $D_{\text{RBC}} = 7.5\mu\text{m}$  and  $h_{\text{RBC}} = 2.0\mu\text{m}$ . The fact that the effective size of RBCs changes in different array geometries demonstrates that DLD devices are sensitive to dynamic behaviour and deformations; phenomena which do not occur for rigid spherical beads. Namely, the flipping motion of RBCs and the lift force experienced by vesicles in shear flow are identified as two of the main mechanisms which differentiate RBC motion from rigid sphere motion in DLD devices.

Results for 2D simulations of RBCs are limited to a qualitative description of particle motion as the dynamic motion of particles with anisotropic dimensions is intrinsically 3D. Chapter 5 presented the results of 3D simulations of RBCs in DLD devices using the RBC model described in section 2.2.2 and the SDPD fluid technique explained in section 2.1.3. Furthermore, chapter 5 includes the results of complimentary experiments which show quantitative agreement with simulated predictions. Both experimental and simulation results found additional transit modes available to RBCs that are not seen for rigid spheres. The new transit modes show zigzag motion and are distinguished from the common neutral zigzag mode as they result in net positive or negative lateral displacement. The presence of additional zigzag modes is attributed to the dynamic behaviour of RBC, hydrodynamic interactions and cell deformation in flow. Furthermore, simulations demonstrate that factors such as viscosity contrast and

cell deformability can be used as bases for separation, as the transitions between transit modes depend on cell deformation and dynamic behaviour. For instance, in thick DLD devices with  $H = 11\mu\text{m}$ , changing the viscosity contrast from  $C = 5$  to  $C = 0.25$  or  $C = 1$  results in a transition in cell dynamics from tumbling to tank-treading. Tumbling dynamics are seen to favour the zigzag mode, as cell flipping often accompanies lane-swapping events, and tank-treading cells favour the displacement mode due to the enhanced lift force they experience upon interaction with posts. However, RBC dynamics are constrained in the thin device and transit modes are shifted to a lesser degree by changing the viscosity contrast. The thin device is better suited for sorting based on very small changes in RBC size, as demonstrated by simulations for RBCs with sizes  $D_{\text{RBC}} = 8.0, 7.5, 7.0\mu\text{m}$  and the range in experimental results caused by the inherent RBC size distribution. The weak shift in transit modes for different viscosity contrasts in the thin device can be attributed to cells with larger internal viscosity deforming less in the fluid flow, resulting in a larger effective size and delayed transition to zigzag modes, suggesting that the thin device may also be used for deformability based sorting.

Comparing the results in the chapters 4 and 5, 2D simulations are well suited to DLD device design for rigid spherical particles but are best used in a qualitative capacity when considering non-spherical deformable particles. For quantitative predictions of non-spherical deformable particle behaviour in DLD devices, 3D simulations are necessary. Consequently, it seems a combined 2D and 3D approach is best suited for investigating DLD device designs for sorting non-spherical deformable particles; where 2D simulations span a wide range of possible DLD geometries, flow conditions, and particle conditions to identify promising sorting configurations; and the more computationally costly 3D simulations focus on the most interesting regions of parameters space, providing quantitative predictions which are of more direct use to experimentalists.

Chapter 6 presents 3D simulations of RBCs in a DLD array for deformability-based sorting which has been designed in light of the findings presented in the previous two chapters. The 2D simulations in chapter 4 suggest that certain post shapes will be more sensitive to RBC deformations. Consequently, the DLD array in chapter 6 is composed of triangular post arrays which are intended to effectively probe the mechanical properties of RBC membranes. Additionally, the 3D simulations in chapter 5 demonstrate that RBC transit modes in DLD devices are highly dependent on viscosity contrast. Consequently, viscosity contrast is kept at  $C = 1$  to ensure that RBC transit through the triangular post arrays is not dominated by viscous effects. However, even with these careful considerations, the initial simulations demonstrate that triangular post arrays are not sufficiently sensitive to the deformations seen for RBCs with pathological values for bending rigidity and shear modulus. The 3D simulations in chapter 5 demonstrate the effectiveness of sorting cells undergoing different dynamic motions. Therefore, the flow regime in the triangular post array is altered to induce different RBC dynamic

behaviours for different RBC membrane shear moduli. The more rigid RBCs undergo tumbling-like dynamics and consequently prefer the zigzag transit modes, whereas softer RBCs exhibit tank-treading-like dynamic behaviours and prefer to travel in the displacement modes. The exploitation of the dynamic behaviours which exist for different RBC shear modulus dramatically increases triangular post array's sensitivity to RBC shear modulus. Moreover, the range of pathological values of RBC shear modulus in the simulations are equivalent to those seen for RBCs infected by the *plasmodium falciparum* parasite. Consequently, the triangular post array presented in chapter 6 represents a promising design for malaria diagnosis providing the correct flow rate and viscosity contrast is used.

Thus, the findings of chapter 4 and 5, were used

The current understanding of particle transit in DLD devices is underpinned by the idea of splitting fluid flow into  $N$  discrete laminae corresponding to the obstacle array period  $N = \lambda/\Delta\lambda$ . If a particle traversing the obstacle array is smaller than the width of laminae as they interface with the obstacle array posts, it will remain in a single lamina and travel horizontally with the fluid flow in a neutral zigzag mode. Conversely, particles larger than laminae width are displaced into neighbouring flow laminae when they interact with the obstacle array posts, resulting in successive lateral displacements across flow laminae for every post encounter. Assuming a parabolic flow profile between vertically adjacent posts yields an analytical value for the width of laminae when they interface with obstacle array posts, and hence an estimate of the critical particle size that determines whether particles move in the displacement or neutral zigzag mode. This general picture for particle transit in DLD holds so long as four criteria are met:

i *Particles do not appreciably disturb the flow field.*

The whole idea of flow laminae only considers the flow field which results from the post array geometry. If particles dramatically alter the flow field, predictions based on the discrete lamina picture will include an innate degree of error.

ii *Inter-post flow is approximately parabolic.*

If the flow profile in-between vertically adjacent posts are not parabolic then the analytically calculated width of the lamina will be incorrect, as will the critical particle size.

iii *Constant effective particle size.*

If particles do not have a constant size in the obstacle array, then each individual post encounter will be different and it would be possible for particles to alternate between zigzag and displacement modes.

iv *Steric interactions with posts account for all lamina crossing*

The steric interaction between particles and posts is assumed as the only mechanism able to perturb particles into neighbouring flow laminae. However, if there



were additional mechanisms which facilitated the crossing of flow laminae then the simple picture of a neutral zigzag and a perfect displacement mode would break down.

Condition (i) is generally untrue and there is always an inherent error in the critical particle size predicted by the analytical solution for the lamina width. However, the error is generally minor and consistent for different post shapes, post spacing  $G$ , and array period  $N$ , as seen in the figures for transit modes of rigid particles in circular- and diamond post arrays. The approximate parabolic flow profile between vertically adjacent posts required by condition (ii) is only met for certain post shapes. Generally, the flow profile can be approximated as parabolic if the flow field between vertically adjacent posts is horizontally and vertically symmetric. For instance, in the case of circular and diamond posts, the flow maximum velocity is located at the central point between vertically adjacent posts. Consequently, the prediction for parabolic flow profiles is very close to the empirical results for diamond and circular post arrays. Whilst the flow velocity also peaks in the channel center in the square post array, the key steric interactions between particles and posts occur at the upper right vertices of squares and the flow profile is not horizontally symmetric in this location. In the case of triangular posts, the flow field's vertical symmetry is broken with fluid travelling faster past the triangle's upper vertex than fluid travelling alongside the triangle's base. As such, the empirical equations for particles travelling in triangular and square post arrays are significantly different from the analytically predicted size for parabolic flows.

Criteria (iii) is always met in the case of rigid spherical particles and sometimes met for anisotropic particles if they are sufficiently confined by the device geometry. For instance, RBCs in experiments, and RBCs in 2D and 3D experiments have varying effective size in DLD devices due to their reorientation and deformation as they tumble in flow. Consequently, the transition between DLD transit modes for non-spherical deformable particles depend on the mechanical properties of the particle, the particle shape and the flow properties, as each of these factors effect dynamic behaviour and the magnitude of deformation. Finally, condition (iv) is expected to be untrue for non-spherical deformable particles as hydrodynamic interactions are known to exert a lift force on vesicles in shear flow near a wall, as is the case for RBCs in the square post array seen in 2D simulations and the 3D RBCs with viscosity contrasts of  $C < 3$ , where tank treading cells are known to experience stronger lift forces than tumbling cells. The lift force results in additional means for particles to cross flow laminae, this can inhibit the transition to zigzagging but also cause cells to migrate faster across the main flow channel once they are in well-established zigzag modes. Generally, this work demonstrates that the ideal case imagined for lamina flow streams with parabolic flow profiles between adjacent posts holds true in very specific cases. Even for the case of rigid spherical particles, post shapes which break the flow field's horizontal or vertical symmetry mean that flow profiles are no longer parabolic and the critical size needs to

be found by alternative means. Furthermore, non-spherical and deformable particles experience additional forces due to hydrodynamic interactions and their effective size in DLD devices are highly dependent on flow strength and dynamic motion.

Many of the current DLD device designs appeal to the theory motivated by lamina flow with approximately parabolic flow profiles between posts. However, as demonstrated in this work, the situation is more complicated for separation of non-spherical deformable particles and in devices that use post shapes which break flow field symmetry. As such, additional considerations should be made when designing future DLD devices for sorting non-spherical deformable particles.

Firstly, the critical size of DLD devices for sorting rigid beads with non-circular post arrays can be determined by 2D simulations. The relevant equations have already been determined in this work for diamond, square, and triangular shaped posts, and similar simulations studies can be carried out to arrive at equivalent equations for other posts shapes. Furthermore, certain post shapes might be beneficial for sorting certain particle types. For instance, diamond shaped posts show a sharper transition from the displacement to the zigzag mode compared to circular post arrays.

Secondly, the rationale used in designing DLD devices to sort non-spherical deformable particles should not limit itself to enforcing effective particle sizes via geometric constraints enforced by the posts and channel height. The dynamic behaviour, degree of deformation and resulting effective size of particles can be manipulated via other means, such as changing the flow speed or the viscosity of the suspending medium. This design methodology would open new possibilities for sorting particles based on their intrinsic properties, such as the viscosity contrast based sorting scheme demonstrated in this work.

Finally, with so many additional parameters to consider for the separation of non-spherical deformable particles, a more simulation based design approach should be encouraged to enable more rigorous investigation of parameter space and reveal the best possible sorting schemes for given particle populations. Moreover, simulation methods allow investigation of DLD device designs without the need for device fabrication or a readily available supply of particle samples, which is non-trivial for DLD applications in fields like diagnostics where labs must meet high security and safety criteria for the handling of especially virulent pathogens.

Given the broad range of parameters that govern the motion of non-spherical deformable particles, the scale of study required is extensive and multifaceted even when considering one single cell type such as RBCs. As such, there is need for continued work to realise the full potential of DLD sorting. The following paragraphs suggest outlines for work that; i) form a direct continuation of the research presented in this study, ii) address the limitations of the methodologies used within this study, and iii) represent potential contributions from different scientific fields to complement the current study:

i *Direct continuation of this work.*

The 2D simulations carried out in chapter 4 of this study begin to address the impact of post shape on particle sorting within DLD devices. However, there are a limitless number of shapes from which to choose and certain post shapes may be better suited for sorting particles of particular shape or with specific mechanical properties. The relatively low computational cost of 2D simulations makes them an ideal tool for exploration of such an extensive parameter space. With this said, informed decisions should be made as to which combinations of post shapes and particle types are investigated. For instance, aerofoil shaped posts have been suggested to reduce clogging effects sometimes found in circular shaped post arrays for separation of non-spherical deformable particles [153]. However, simulations of the aerofoil only consider the fluid flow and do not model suspended particle types. As such the 2D model for RBCs used in this work could be simulated in aerofoil post shape DLD device to further investigate their effectiveness.

The 3D work presented in this study primarily investigated the effects of RBC cell dynamics in DLD devices via changes in geometric confinement and the viscosity contrast between intra- and extra-cellular fluid. Furthermore, it is well established that the mechanical properties of cells and the magnitude of shear rate also effect the onset of morphological and dynamic behaviour transitions. The 3D simulation in the final section of this work demonstrated a DLD device design for sorting RBCs via their dynamic behaviour in accordance with different membrane properties such as bending rigidity and shear modulus. Experimental works are needed to corroborate these simulation results and to test the feasibility of the device design. Furthermore, the changes in RBC transit modes for different viscosity contrasts observed in this thesis were attributed to tank-treading and tumbling motions. Recent experimental and simulation works have revealed that additional dynamic behaviours are observed for RBCs, including highly deformed tumbling poly-lobed shapes at high shear rates [99]. These new dynamic regimes are of interest because they occur at high flow velocities which could potentially improve the throughput of DLD devices; reducing the time taken to analyse samples and increasing the likelihood of detecting rare cells.

The work throughout this study uses RBC models to represent non-spherical deformable particles as fluid filled vesicles. However, there are many types of bioparticles which are not adequately described as vesicles. DNA and streptococci chains are both examples of bioparticles which often require sorting; In genome sequencing it is desirable to extract genomic-length DNA which contains the complete set of genes for a given cell, and *Streptococcus pneumoniae* are a bacterial pathogen whose virulence is known to depend on the chain length of the coccus[154, 155]. Both the aforementioned examples are better modelled as semi-flexible or fully flexible rods as opposed to fluid vesicles. As such, simulations which explore the

length dependence of sorting flexible rods in DLD obstacle arrays would be of considerable use for designing DLD devices to sort DNA or streptococci chains.

Finally, many different label sorting techniques were introduced in section 1.3 and this study has looked at just DLD. Other sorting techniques used in tandem with DLD devices could dramatically enhance sorting of specific types of particles. For instance, dielectrophoresis used in conjunction with DLD has been suggested as a means for allowing critical size tunability and allowing for sorting based on particle's electric permeability [125]. Additionally, density based sorting of particles has been demonstrated in DLD devices by using a density gradient in the fluid to particles of differing densities towards different post geometries [156]. Whilst the inclusion of additional sorting techniques to DLD devices poses great promise for developing novel sorting schemes, they also increase the number of parameters that need to be considered in DLD design. This work has demonstrated that simulation provide a valuable tool for device design where a great number of effects contribute towards particle transit in DLD devices. Consequently, similar simulation approach in this study should be revisited and altered to investigate the effects of external forces, such as dielectrophoretic forces and gravitational forces, on particle sorting in DLD devices.

ii *Addressing the limitations of this work.*

An obvious limitation of work presented in this study, is the unrealistic degrees of freedom afforded to RBCs in 2D simulations and the basic assumption that all RBC are adequately described as 2D shapes. Obviously this is untrue, and the intrinsic motion of RBCs in DLD devices is 3D, as demonstrated nicely in figure 5.10a where a RBCs orientation switches from perpendicular, to parallel, and back to perpendicular with the channel floor and ceiling in the course of a lane swapping event. However, the sacrifice in accuracy of 2D simulations is considered a worthwhile trade-off for the decrease in computational load, which allows for the simultaneous testing of many DLD device configurations at the same processing cost of a 3D simulation which probes a much smaller region of parameter space. As such, a sensible combination of 2D simulations and 3D simulations should be employed, where the former investigates large numbers of possible DLD configurations and the latter hones in on the most promising candidates to provide a more quantitative description.

More specific limitations exist in both the experimental and simulation techniques throughout this work. On one hand, in the case of simulations, the accuracy of the predicted particle motions in certain DLD configurations is limited by the success of the particle model itself. For instance, a particle model will only recreate the behaviour observed in experiments if it correctly captures the mechanical properties of the particle. On the other hand, in experimental work, there exists an inherent variability in particle properties which are non-trivial to control. These simulation

and experimental limitations are present throughout the study of RBC motion in DLD devices in this thesis. For instance, the RBC model employed throughout this work does not account for membrane viscosity due the present attempts at its inclusion resulting in stability issues or failure to recreate realist behaviour. Consequently, further work is required to address this issue, as membrane viscosity could play a role in RBC separation in DLD devices. Furthermore, in order to model RBCs in pathogenic states, the model parameters must be altered to mimic dysfunctional RBC behaviour. However, selection of the correct model parameters is limited by the available experimental data on pathogenic RBCs' mechanical properties and there is a need for rigorous study of unhealthy RBC mechanical properties using techniques such as optical tweezers, micropipette aspiration, flow cytometry and video spectroscopy[157–160].

From an experimental point of view, it is important for simulation studies to recognise the inherent variabilities in cell properties. For example, a simulated DLD device might prove incredibly sensitive to small changes in particle deformability. However, it is incredibly easy to fix every parameter apart from those pertaining to particle deformability within simulations. In practice, this device would be of no functional use to experimentalists for deformability based sorting if the DLD array was even more sensitive to inherent variations in particle size, a factor which could easily be overlooked in simulations. Additionally, if simulations are to take a more central role in design of microfluidic devices, an appreciation of the limits of microfluidic fabrication techniques is important. For instance, post shapes with sharp vertices will never be perfectly sharp in practise and there is also bound to be some variation in post shape across an entire microfluidic obstacle array. As such, sorting schemes devised by simulations need to consider the limits of fabrication techniques.

### iii *Complimentary research from additional fields.*

The development and application of microfluidics is highly interdisciplinary and considerable contributions are necessary to bring devices from their inception to real-world application. For example, in the case of using DLD devices to deliver point-of-care diagnosis of diseases, there are many problems which must be addressed unique to each type of disease and the locations in which they are endemic. For instance, malarial infections in south east Asia and the eastern Mediterranean are not exclusively caused by the *plasmodium falciparum* virus, a large percentage of infections are caused by *plasmodium vivax*. Diagnostic devices employed in these regions would need to differentiate between RBCs infected by the two different parasites. As such, detailed analysis of the differences in mechanical properties between RBCs infected by each type of parasite is needed before DLD devices can be developed to sort them. This situation becomes even more complex when taking the remaining malaria species which infect humans into account, *plasmodium*

*ovale* and *malariae*, which would each require a similar analysis to identify the key changes in RBC properties to use as biomarkers for separation.

Affordable and scalable fabrication techniques are also essential to realise point-of-access diagnostics of malaria. Once reliable devices have been designed, manufacturers must develop strategies to achieve large scale production at low costs without sacrificing consistency and precision. Affordability and scalability are essential as malaria is such a wide spread problem and the regions in which the disease is endemic do not have the financial resources to tackle the problem using costly equipment. Furthermore, manufacturing techniques can be used to address issues with device throughput. For example, using stacked DLD chips allows the division of a patient blood sample into small fractions which can be sorted in parallel and collected into a single repository for inspection by light spectroscopy.

In summary, the current methodology used for designing DLD devices is primarily based on experimental results and theory for rigid spherical particles in circular post arrays. In this limited case, particles travel through DLD devices in one of two motions; the zigzag and displacement modes depending on their size relative to the device's critical size. This thesis uses RBC motion in DLD devices to demonstrate that the same description cannot accurately describe the motion of non-spherical and deformable particles in DLD devices. Firstly, the transition between transit modes of non-spherical deformable particles is not only dependant on their size; dynamic behaviour and the degree of deformation in flow are additional key factors. Secondly, additional zigzag modes are available to non-spherical deformable particles, which result in positive or even negative lateral displacement. These additional modes can be attributed to tumbling behaviours and hydrodynamic forces which cause particles to cross flow lamina, phenomena which do not occur for rigid spherical particles. Consequently, additional factors that alter particles' dynamic behaviour, deformation and hydrodynamic interactions can be utilised for sorting deformable non-spherical particles. For instance, different flow speeds, suspending medium viscosities, and post shapes, will result in DLD devices favourable for sorting particles with particular mechanical properties and morphology. Furthermore, the work also demonstrates the promise of simulation techniques used in conjunction with experimental work for understanding key physical mechanisms within microfluidics and should encourage similar studies for applications beyond that of particle sorting.

## APPENDIX





## SIMULATION DETAILS

## 2D SIMULATION PARAMETERS

The DPD parameters introduced in equations 2.2, 2.3, 2.4, 2.5, 2.6, and 2.7 used to simulate fluid in the 2D simulations are summarised in table A.2. Additionally, the parameters which define the mechanical properties of the 2D circle and RBC models used in equations 2.30, 2.31, 2.32, 2.33, and 2.34 are presented in A.1.

	$N_v$	$l_m/l_0$	$\kappa/k_B T l_0$	$YD/k_B T$	$A_0/D^2$	$k_a D^2/k_B T$
Circles	30...60	2.2	500	180000	$1.04\pi/4$	97000
RBCs	50	2.2	50	9000	0.36	37430

Table A.1: The parameters used to model the rigid circles and RBCs in 2D simulations, where  $N_v$  is the number of vertices which make up the membrane,  $l_m$  is the maximum spring length,  $l_0$  is the equilibrium spring length, and  $D$  is the characteristic particle diameter of a circle or RBC. The macroscopic bending rigidity is  $\kappa = k_b l_0$ , where  $k_b$  is the bending constant.  $Y$  is the particles Young's modulus,  $A_0$  is the particle's target area, and  $k_a$  is the area constraint coefficient.

$n r_c^2$	$\alpha r_c/k_B T$	$\gamma r_c/\sqrt{m k_B T}$	$k$	$\eta r_c^2/\sqrt{m k_B T}$
11.25	60	30	0.15	325

Table A.2: The parameters used for fluid modelled using the DPD method. Mass and length for the DPD fluid are measured using units of fluid particles' mass  $m$  and a cut-off radius  $r_c$ . Here,  $n$  is the fluid number density,  $\gamma$  is the dissipative force coefficient,  $\alpha$  is the repulsive force coefficient,  $k$  is the weight function exponent, and  $\eta$  is the dynamic viscosity. For all 2D simulations,  $m = 1$ ,  $r_c = 1.5$ ,  $n = 5$ , and the temperature is set as  $k_B T = 1$ .

## 3D SIMULATION PARAMETERS

The SDPD parameters introduced in equations 2.13, 2.14, 2.15, 2.16, 2.17, and 2.18 used to simulate fluid in the 3D simulations are summarised in table A.3. Additionally, the parameters which define the mechanical properties of the 3D RBC model defined by equations 2.30, 2.36, 2.37, and 2.38 is presented in A.4.

FLUID PARAMETERS	SCALED UNITS	PHYSICAL UNITS
$p_0$	$16 \frac{k_B T}{l_0^3}$	1.07 Pa
$b$	$12.8 \frac{k_B T}{l_0^3}$	0.86 Pa
$\eta_o$	$25.3 \frac{\sqrt{m k_B T}}{l_0^2}$	$1.2 \times 10^{-3} \text{ Pa} \cdot \text{s}$
$\eta_i$	$25.3, 126.6 \frac{\sqrt{m k_B T}}{l_0^2}$	$6 \times 10^{-3} \text{ Pa} \cdot \text{s}$
$k_B T$		$4.282 \times 10^{-21} \text{ J}$

Table A.3: Parameters defining the model values used for the fluid properties and their physical equivalents. Mass and length for SDPD fluid which conserves angular momentum are measured in units of the fluid particle mass  $m$  and the membrane bond length  $l_0$ .  $p_0$  and  $b$  are parameters for the pressure equation, and  $\eta_o$  and  $\eta_i$  are the extra- and intra-cellular fluid dynamic viscosities, respectively. In all simulations, we have set  $m = 1$ ,  $l_0 = 0.4$ , and the thermal energy  $k_B T = 0.4$ .

RBC PARAMETERS	SCALED UNITS	PHYSICAL UNITS
$N_v$	1000	
$A_r$		$133.5 \times 10^{-12} \text{ m}^2$
$D_r$	$\sqrt{A_r/\pi}$	$6.5 \times 10^{-6} \text{ m}$
$l_0$	$0.061 D_r$	$3.91 \times 10^{-7} \text{ m}$
$V_r$	$0.34 D_r^3$	$93.1 \times 10^{-18} \text{ m}^3$
$T$		310 K
$Y_r$	$1.82 \times 10^5 \frac{k_B T}{D_r^2}$	$18.9 \times 10^{-6} \text{ N/m}$
$\kappa_r$	$70 k_B T$	$3 \times 10^{-19} \text{ J}$
$k_d$	$4.2 \times 10^4 \frac{k_B T}{D_r^2}$	$4.3 \times 10^{-6} \text{ N/m}$
$k_a$	$2.1 \times 10^6 \frac{k_B T}{D_r^2}$	$2.1 \times 10^{-4} \text{ N/m}$
$k_v$	$1.4 \times 10^7 \frac{k_B T}{D_r^3}$	$220 \text{ N/m}^2$

Table A.4: Parameters defining the model values used for the RBC properties and their physical equivalents.  $N_v$  is the number of membrane vertices,  $A_r$  is the RBC membrane area,  $l_0$  is the average bond length,  $V_r$  is the RBC volume,  $T$  is the temperature,  $Y_r$  is the membrane Young's modulus,  $\kappa_r$  is the membrane bending rigidity, and  $k_d$ ,  $k_a$ , and  $k_v$  are the local area, global area, and volume constraint coefficients, respectively. In all simulations, we have chosen  $A_r = 133.5$  and  $k_B T = 0.4$ , which implies that  $D_r = 6.5$  and  $l_0 = 0.4$ .

## EXPERIMENTAL DETAIL

---

### DEVICE SET-UP

The DLD devices used in experiments presented in chapter 5 were fabricated by replica molding, using the same method and equipment used in previous work by Beech *et al.* [72]. Prevention of adhesion of blood cells to the inner surface of the devices is ensured by application of a polymer brush on the polydimethylsiloxane (PDMS). This is achieved by filling devices with 0.2% PLL(20)-g[3.5]-PEG(2) (SuSoS AG, Dübendorf, Switzerland) and rinsing for 20 minutes with autoMACS™ immediately after O<sub>2</sub> plasma treatment and bonding.

The experimental device was originally designed by Holm *et al.* [8] to sort particles of different sizes, with successive sections within the device corresponding to different critical radii [8]. The device geometry [8, 72] is defined by the post diameter  $D = 20\ \mu\text{m}$ , lateral shift in successive pillar rows  $\Delta\lambda$ , lateral center-to-center spacing between posts  $\lambda = 32\ \mu\text{m}$ , and the height between the two enclosing floor and ceiling plates  $H$ , as shown in figure B.1. The lateral shift can conveniently be defined as the row fraction  $\epsilon$  of the post spacing  $\Delta\lambda = \epsilon\lambda$ . The experimental devices consist of 13 consecutive sections of post arrays, which are differentiated by their lateral shifts  $\Delta\lambda$  between successive rows as summarized in table B.1. Note that some of the sections have row-shift fractions  $\epsilon$  that are equivalent to  $M/N$ , where  $M$  and  $N$  are integers and  $M \neq 1$ , i.e. we have a "non-integer" row-shift fraction. This is due to limitations in the photomask fabricating process (a manufacturing grid of 200nm), which means that in many cases the desired integer row-shift fractions are not possible, in which case the nearest non-integer row-shift fraction is used. While non-integer row-shift fractions have been shown to give rise to two additional zig-zag modes with accompanying critical sizes [161, 162], in the present study these modes are not observed.

Two versions of the sequential device were used throughout this work, distinguished by the distance between the top and bottom plates covering the post arrays. The first device has a height of  $H = 11\ \mu\text{m}$ , which is larger than a RBC diameter of about  $8\ \mu\text{m}$ , while the second device is thinner with  $H = 4\ \mu\text{m}$ , which is smaller than the RBC diameter but larger than the RBC thickness of about  $2 - 3\ \mu\text{m}$ . The two devices are referred to as the 'thick' and 'thin' DLD devices, respectively.

Several inlets and outlets lead to and from the DLD array channel and were employed to control flow and the sample input/output, as shown in figure B.1. Both devices had one large fluid buffer inlet and one small buffer inlet to reduce wall effects and to ensure a well defined starting position from which total displacement can be

SECTION	$\Delta\lambda/\mu\text{m}$	$\epsilon$	$\frac{1}{\epsilon}$	ROWS	$R_c/\mu\text{m}$
1	0.8	0.025	40	200	1.43
2	1.2	0.0375	80/3	130	1.74
3	1.6	0.05	20	100	2.0
4	2.0	0.0625	16	80	2.22
5	2.6	0.0813	160/13	60	2.52
6	3.2	0.1	10	50	2.78
7	3.8	0.1188	160/19	40	3.02
8	4.4	0.1375	80/11	35	3.24
9	5.2	0.1625	80/13	30	3.51
10	6.0	0.1875	16/3	25	3.76
11	6.8	0.2125	80/17	20	4.0
12	7.8	0.2438	160/39	20	4.27
13	8.8	0.275	40/11	15	4.52

Table B.1: Parameters defining the obstacle array geometry for each section of the DLD device.

$\Delta\lambda$  is the lateral shift between successive rows for each section,  $\epsilon = \Delta\lambda/\lambda$  is the section's shift fraction, and  $R_c$  is the critical particle size [6, 133]. The fourth column in the table specifies the number of rows in each section.

ascertained. The sample inlet channel is placed directly between the two buffer inlets and also included a filter to remove large unwanted particles which would otherwise cause device clogging. Flow is driven by a pressure gradient generated by a pressure drop of 22 mbar between the buffer inlets and outlets, where the outlets were kept at atmospheric pressure and the overpressure at the inlets was maintained using a MFCS-4C pressure controller (Fluigent, Paris, France).

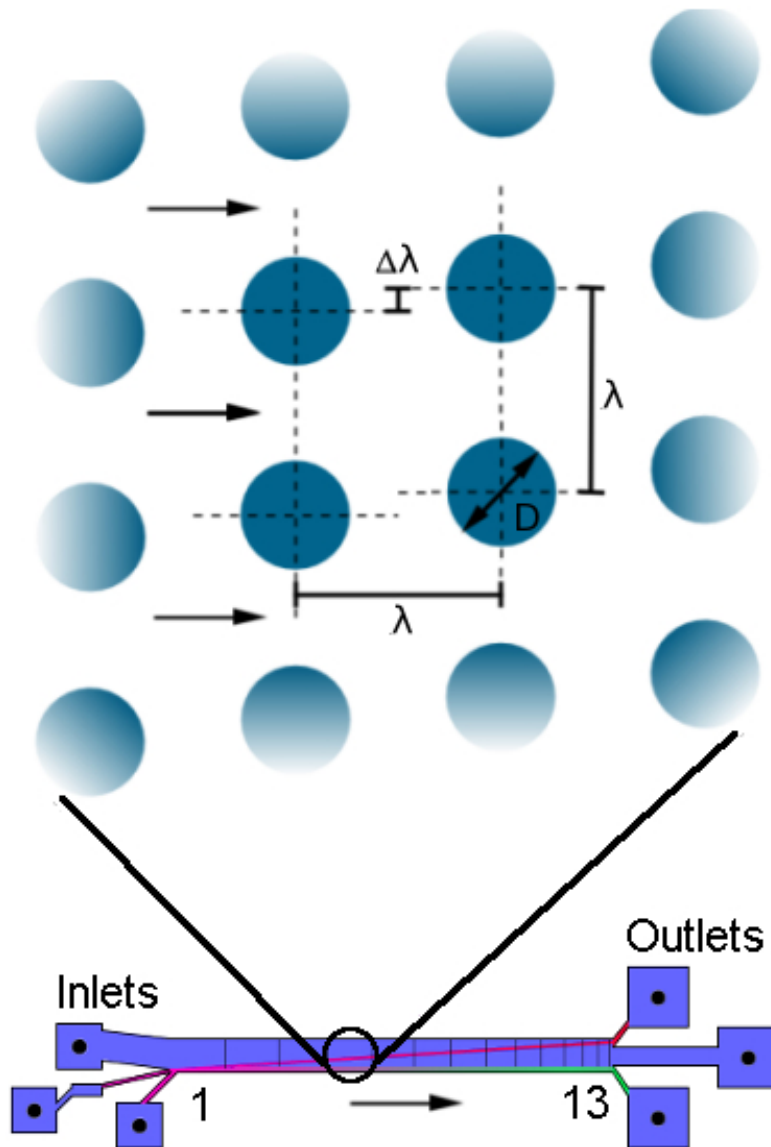


Figure B.1: A close-up bird's eye view of the obstacle array and a schematic of the sequential device with 13 sections, each with different  $\Delta\lambda$ . The flow direction is indicated by the arrows. Solution from the inlets on the left is carried by the flow within DLD to the right, where the particles of different sizes are collected at various outlets.

## SAMPLE PREPARATION

All blood samples used throughout the course of experiments was extracted from healthy volunteers via finger pricking. As mentioned in the main text, experiments were conducted at a viscosity contrasts of 5, 2, 1 and 0.25 between the cytosol and the surrounding buffer. For the higher viscosity contrast conditions, the cells were suspended in autoMACS™ running buffer (Miltenyi Biotech, Auburn, CA). This solution (pH 7.2) contains phosphate buffered saline (PBS) supplemented with 0.5% bovine serum albumin (BSA), 2 mM EDTA, and 0.09% azide, and acts to suppress blood clotting without altering the cell shape due to a changed osmotic pressure because it is isotonic. For lower viscosity contrast measurements the autoMACS™ running buffer was supplemented with Dextran-500 (# 700013-096, VWR International LLC, PA, USA). To measure the viscosities at different Dextran concentrations (see figure B.2), Ubbelohde viscometers were used (UBBEL Visco, Paragon Scientific Ltd, UK.). During the viscosity measurement process, ambient temperatures ranged between 21.8-22.°C, which is similar to the measurements conducted with cells in the DLD device.

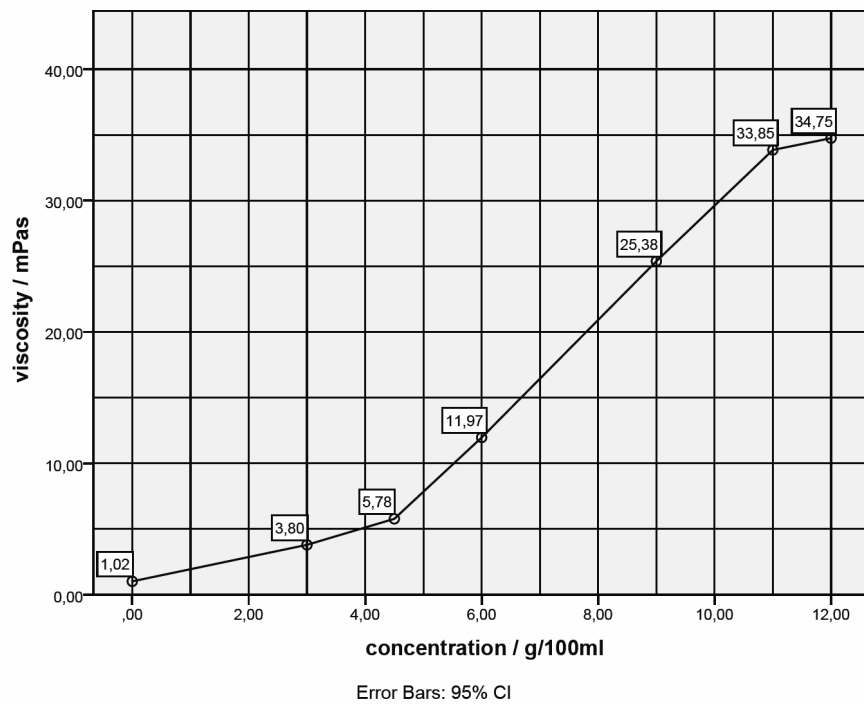


Figure B.2: Viscosity measurement of different dextran-500 concentrations in autoMACS. In order to achieve a viscosity contrasts of  $C = 2, 1$  and  $0.25$  between the medium and the cytosol, the suspending medium viscosity needed to be increased to two, five and twenty five times that of normal autoMACS buffer viscosity.

Dextran is widely used to alter the viscosity of fluid samples. It is often chosen because it is a neutral polysaccharide, i.e. the resulting viscosity does not depend on the pH or salt concentration of the solution. In order to minimize the change to the osmotic

pressure across the RBC membranes, a large Dextran molecule was chosen, with an average molecular weight of 500 kDa. At concentrations of 11% the change in osmotic pressure is 0.22mM and is negligible compared to isotonic blood osmolality of 300mM. Furthermore, microscopic examinations of cell samples at low viscosity contrast and high viscosity contrast did not reveal any visible differences in cell morphology.

#### DATA ANALYSIS AND ACQUISITION

All experimental RBC trajectories were recorded through an inverted Nikon Eclipse TE2000-U microscope (Nikon Corporation, Tokyo, Japan). Additionally, high-speed images of RBCs at high magnification were recorded using an EoSens mini MC-1370 camera (Mikrotron GmbH, Unterschleissheim, Germany). In all other cases an Andor iXon EMCCD camera (Andor Technology, Belfast, Northern Ireland) or Hamamatsu Orca Flash 4.0 (Hamamatsu, Shizuoka Pref., Japan) were used.

The simultaneous transit of many RBCs through each section of the DLD devices were recorded to video using the microscope and camera set-ups previously described. Next, trajectories of individual RBCs were extracted from the recordings using the particle-tracking application MOSAIC in the image processing suite ImageJ [163]. In order to enhance particle detection, a median average of all frames from the entire video is subtracting from each individual frame, thus removing the video background.

All trajectories extracted from the recorded videos went through a pre-screening procedure. In the pre-screening process all trajectories which are too short or which include direct interactions between RBCs were discarded. As a general rule, trajectories were considered too short if the spanned a small fraction of the video domain, corresponding to RBC traversal over only a few posts in the device. The short trajectories tend to be present at the beginning or end of videos and also occur due to detection failure if the video contrast becomes insufficient for tracking in particular frames. The trajectories with direct interactions between RBCs were excluded from further analysis, since RBC collisions were not accounted for in simulations, as they only ever considered a single RBC. Finally, some outlier trajectories were removed manually after visual inspection. The majority of outlier cases were identified as the result of blockages between posts (see figure B.3 or occasional missing posts which are expected from occasional errors in device fabrication. A summary of the RBC trajectory refinement process for the video recordings of RBC transits in the DLD devices is shown in tables B.2, B.3, B.4, and B.5, where the numbers of total, accepted, and rejected trajectories are given for all experiments.

SECTION	TOTAL # OF TRAJ.	REJECTED	ACCEPTED	ACCEPTED FRACTION	AVERAGE # OF POSTS
1	14	0	14	1.0	31
3	12	2	10	0.83	37
4	29	5	24	0.83	25
5	13	2	11	0.85	41
6	13	27	0	1.0	27
7	37	1	36	0.97	37
8	31	7	25	0.78	23
9	96	0	96	1.0	28
11	38	6	32	0.84	21
13	97	8	89	0.92	31

Table B.2: The total number of RBC trajectories recorded in each section of the thick device at  $C = 1$  and the number of excluded and accepted trajectories. The average number of posts describes the average length of all accepted trajectories.

SECTION	TOTAL # OF TRAJ.	REJECTED	ACCEPTED	ACCEPTED FRACTION	AVERAGE # OF POSTS
1	13	1	12	0.92	38
2	16	2	14	0.88	43
3	12	1	11	0.92	31
4	41	6	35	0.85	39
5	17	4	13	0.76	48
9	45	4	41	0.91	22
11	5	1	4	0.8	21

Table B.3: The total number of RBC trajectories recorded in each section of the thick device at  $C = 0.25$  and the number of excluded and accepted trajectories. The average number of posts describes the average length of all accepted trajectories.



SECTION	TOTAL # OF TRAJ.	REJECTED	ACCEPTED	ACCEPTED FRACTION	AVERAGE # OF POSTS
1	8	1	7	0.88	28
2	-	-	-	-	-
3	-	-	-	-	-
4	-	-	-	-	-
5	-	-	-	-	-
6	15	0	15	1.0	23
7	23	4	19	0.83	29
8	39	10	29	0.74	16
9	26	7	19	0.73	15
10	20	5	15	0.75	15
11	40	8	32	0.8	15
12	17	3	14	0.82	16
13	71	1	70	0.99	11

Table B.4: The total number of RBC trajectories recorded in each section of the thin device at  $C = 5$  and the number of excluded and accepted trajectories. The average number of posts corresponds to the average length of all accepted trajectories. Note that values for sections 2-5 are omitted as displacement-mode transit was evident from videos and there was no need for alignment.

SECTION	TOTAL # OF TRAJ.	REJECTED	ACCEPTED	ACCEPTED FRACTION	AVERAGE # OF POSTS
1	14	2	12	0.86	27
3	6	0	6	1.0	45
5	13	0	13	1.0	28
7	11	0	11	1.0	12
9	23	2	21	0.91	9

Table B.5: The total number of RBC trajectories recorded in each section of the thin device at  $C = 2$  and the number of excluded and accepted trajectories. The average number of posts corresponds to the average length of all accepted trajectories.

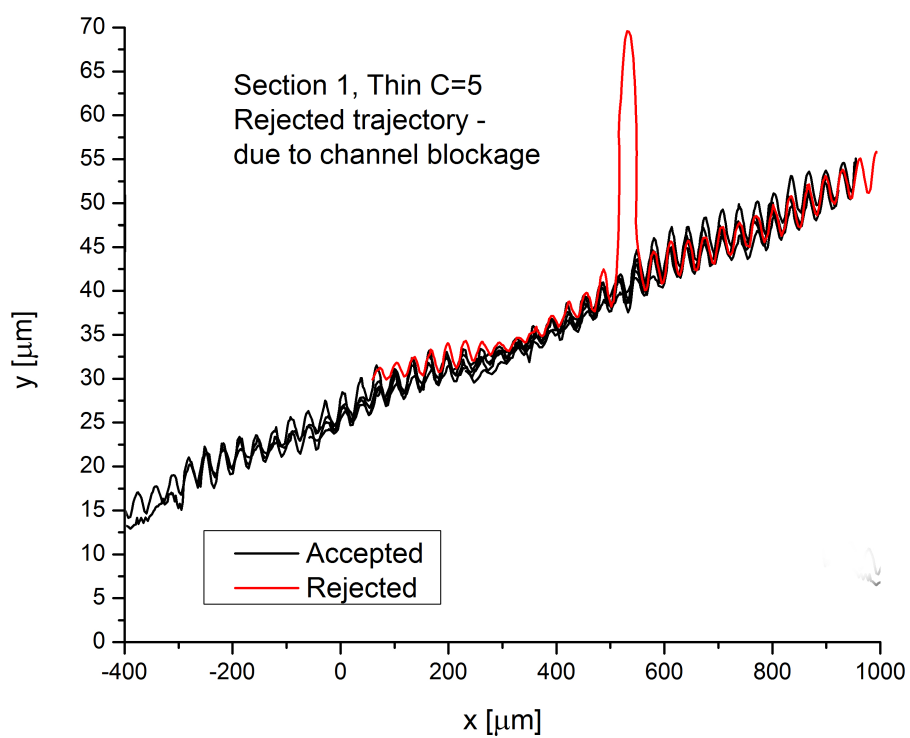


Figure B.3: A rejected RBC trajectory due to blockage between posts.

## BIBLIOGRAPHY

---

- [1] World Health Organization. *Basic Malaria Microscopy, Part I. Leaner's guide*. Geneva, Switzerland: WHO Press, 2010, pp. 74–75.
- [2] Jaoon Young Hwan Kim, Ho Seok Kwak, Young Joon Sung, Hong Il Choi, Min Eui Hong, Hyun Seok Lim, Jae-Hyeok Lee, Sang Yup Lee, and Sang Jun Sim. "Microfluidic high-throughput selection of microalgal strains with superior photosynthetic productivity using competitive phototaxis." In: *Scientific reports* 6 (2016).
- [3] W Dittrich and W Gohde. *Flow-through chamber for photometers to measure and count particles in a dispersion medium*. US Patent 3,761,187. 1973.
- [4] Stefan Miltenyi, Werner Müller, Walter Weichel, and Andreas Radbruch. "High gradient magnetic cell separation with MACS." In: *Cytometry* 11.2 (1990), pp. 231–238.
- [5] Myron K Brakke. "Density gradient centrifugation: a new separation technique." In: *Journal of the American Chemical Society* 73.4 (1951), pp. 1847–1848.
- [6] Lotien Richard Huang, Edward C Cox, Robert H Austin, and James C Sturm. "Continuous particle separation through deterministic lateral displacement." In: *Science* 304.5673 (2004), pp. 987–990.
- [7] David W Inglis, John A Davis, Robert H Austin, and James C Sturm. "Critical particle size for fractionation by deterministic lateral displacement." In: *Lab on a Chip* 6.5 (2006), pp. 655–658.
- [8] Stefan H Holm, Jason P Beech, Michael P Barrett, and Jonas O Tegenfeldt. "Separation of parasites from human blood using deterministic lateral displacement." In: *Lab on a Chip* 11.7 (2011), pp. 1326–1332.
- [9] John A Davis, David W Inglis, Keith J Morton, David A Lawrence, Lotien R Huang, Stephen Y Chou, James C Sturm, and Robert H Austin. "Deterministic hydrodynamics: taking blood apart." In: *Proceedings of the National Academy of Sciences* 103.40 (2006), pp. 14779–14784.
- [10] Kevin Loutharback, Joseph D'Silva, Liyu Liu, Amy Wu, Robert H Austin, and James C Sturm. "Deterministic separation of cancer cells from blood at 10 mL/min." In: *AIP advances* 2.4 (2012), p. 042107.
- [11] Eric P Widmaier, Hershel Raff, and Kevin T Strang. *Vander's human physiology*. McGraw Hill Boston, Mass, USA, 2006.
- [12] Sharmila Sreekumar. *Basic Physiology*. Prentice-Hall Of India Pvt Limited, 2010.

- [13] David E Sadava, David M Hillis, H Craig Heller, and May Berenbaum. *Life: the science of biology*. Vol. 2. Macmillan, 2009.
- [14] Anthea Maton. *Human Biology and Health*. Prentice Hall, 1997.
- [15] Jean-Michel Paulus. "Platelet size in man." In: *Blood* 46.3 (1975), pp. 321–336.
- [16] K.T. Patton. *Anatomy and Physiology*. Elsevier Health Sciences, 2015.
- [17] Mary Louise Turgeon. *Clinical hematology: theory and procedures*. Lippincott Williams & Wilkins, 2005.
- [18] Yuan-cheng Fung. *Biomechanics: mechanical properties of living tissues*. Springer Science & Business Media, 2013.
- [19] DA Jones. "The important of surface area/volume ratio to the rate of oxygen uptake by red cells." In: *The Journal of general physiology* 74.5 (1979), pp. 643–646.
- [20] World Health Organization. *World Malaria Report 2016*. Geneva, Switzerland: WHO Press, 2016.
- [21] World Health Organization. *Guidelines for the treatment of malaria*. Geneva, Switzerland: WHO Press, 2015.
- [22] Global Health Division of Parasitic Diseases and Malaria. *Biology of Malaria*. <https://www.cdc.gov/malaria/about/biology/>. Accessed: 2016-12-10. 2016.
- [23] Kesinee Chotivanich, Rachanee Udomsangpetch, Rose McGready, Stephane Proux, Paul Newton, Sasithon Pukrittayakamee, Sornchai Looareesuwan, and Nicholas J White. "Central role of the spleen in malaria parasite clearance." In: *Journal of Infectious Diseases* 185.10 (2002), pp. 1538–1541.
- [24] Christian F Ockenhouse, T Tegoshi, Y Maeno, C Benjamin, M Ho, Khin Ei Kan, Y Thway, K Win, M Aikawa, and RR Lobb. "Human vascular endothelial cell adhesion receptors for Plasmodium falciparum-infected erythrocytes: roles for endothelial leukocyte adhesion molecule 1 and vascular cell adhesion molecule 1." In: *Journal of Experimental Medicine* 176.4 (1992), pp. 1183–1189.
- [25] S Majid Hosseini and James J Feng. "How malaria parasites reduce the deformability of infected red blood cells." In: *Biophysical journal* 103.1 (2012), pp. 1–10.
- [26] Alireza Karimi, Mahdi Navidbakhsh, Afsaneh Motevalli Haghi, and Shahab Faghihi. "An innovative shape equation to quantify the morphological characteristics of parasitized red blood cells by Plasmodium falciparum and Plasmodium vivax." In: *Proceedings of the Institution of Mechanical Engineers, Part H: Journal of Engineering in Medicine* 227.4 (2013), pp. 428–437.
- [27] Yao Zhang, Changjin Huang, Sangtae Kim, Mahdi Golkaram, Matthew WA Dixon, Leann Tilley, Ju Li, Sulin Zhang, and Subra Suresh. "Multiple stiffening effects of nanoscale knobs on human red blood cells infected with Plasmodium falciparum malaria parasite." In: *Proceedings of the National Academy of Sciences* 112.19 (2015), pp. 6068–6073.

- [28] Lee R Moore, Hisashi Fujioka, P Stephen Williams, Jeffrey J Chalmers, Brian Grimberg, Peter A Zimmerman, and Maciej Zborowski. "Hemoglobin degradation in malaria-infected erythrocytes determined from live cell magnetophoresis." In: *The FASEB journal* 20.6 (2006), pp. 747–749.
- [29] J Patrick Shelby, John White, Karthikeyan Ganesan, Pradipsinh K Rathod, and Daniel T Chiu. "A microfluidic model for single-cell capillary obstruction by *Plasmodium falciparum*-infected erythrocytes." In: *Proceedings of the National Academy of Sciences* 100.25 (2003), pp. 14618–14622.
- [30] Brian M Cooke, Stephen Morris-Jones, Brian M Greenwood, and Gerard B Nash. "Mechanisms of cytoadhesion of flowing, parasitized red blood cells from Gambian children with *falciparum* malaria." In: *The American journal of tropical medicine and hygiene* 53.1 (1995), pp. 29–35.
- [31] Azar Radfar, Darío Méndez, Carlos Moneriz, María Linares, Patricia Marín-García, Antonio Puyet, Amalia Diez, and José M Bautista. "Synchronous culture of *Plasmodium falciparum* at high parasitemia levels." In: *Nature protocols* 4.12 (2009), pp. 1899–1915.
- [32] Carlos F Gonzalez and Vincent T Remcho. "Harnessing dielectric forces for separations of cells, fine particles and macromolecules." In: *Journal of Chromatography A* 1079.1 (2005), pp. 59–68.
- [33] Joel Voldman. "Electrical forces for microscale cell manipulation." In: *Annu. Rev. Biomed. Eng.* 8 (2006), pp. 425–454.
- [34] Kazunori Takahashi, Akihiro Hattori, Ikurou Suzuki, Takanori Ichiki, and Kenji Yasuda. "Non-destructive on-chip cell sorting system with real-time microscopic image processing." In: *Journal of nanobiotechnology* 2.1 (2004), p. 5.
- [35] Feng Guo, Xing-Hu Ji, Kan Liu, Rong-Xiang He, Li-Bo Zhao, Zhi-Xiao Guo, Wei Liu, Shi-Shang Guo, and Xing-Zhong Zhao. "Droplet electric separator microfluidic device for cell sorting." In: *Applied Physics Letters* 96.19 (2010), p. 193701.
- [36] Jean-Christophe Baret, Oliver J Miller, Valerie Taly, Michaël Ryckelynck, Abdelham El-Harrak, Lucas Frenz, Christian Rick, Michael L Samuels, J Brian Hutchison, Jeremy J Agresti, et al. "Fluorescence-activated droplet sorting (FADS): efficient microfluidic cell sorting based on enzymatic activity." In: *Lab on a Chip* 9.13 (2009), pp. 1850–1858.
- [37] Jeremy J Agresti, Eugene Antipov, Adam R Abate, Keunho Ahn, Amy C Rowat, Jean-Christophe Baret, Manuel Marquez, Alexander M Klibanov, Andrew D Griffiths, and David A Weitz. "Ultrahigh-throughput screening in drop-based microfluidics for directed evolution." In: *Proceedings of the National Academy of Sciences* 107.9 (2010), pp. 4004–4009.

- [38] Michael Ward, Patrick Turner, Marc DeJohn, and Gregory Kaduchak. "Fundamentals of acoustic cytometry." In: *Current Protocols in Cytometry* (2009), pp. 1–22.
- [39] Andreas Lenshof and Thomas Laurell. "Continuous separation of cells and particles in microfluidic systems." In: *Chemical Society Reviews* 39.3 (2010), pp. 1203–1217.
- [40] Linda Johansson, Fredrik Nikolajeff, Stefan Johansson, and Sara Thorslund. "On-chip fluorescence-activated cell sorting by an integrated miniaturized ultrasonic transducer." In: *Analytical chemistry* 81.13 (2009), pp. 5188–5196.
- [41] Ola Jakobsson, Carl Grenvall, Maria Nordin, Mikael Evander, and Thomas Laurell. "Acoustic actuated fluorescence activated sorting of microparticles." In: *Lab on a Chip* 14.11 (2014), pp. 1943–1950.
- [42] Jinjie Shi, Hua Huang, Zak Stratton, Yiping Huang, and Tony Jun Huang. "Continuous particle separation in a microfluidic channel via standing surface acoustic waves (SSAW)." In: *Lab on a Chip* 9.23 (2009), pp. 3354–3359.
- [43] Zhuochen Wang and Jiang Zhe. "Recent advances in particle and droplet manipulation for lab-on-a-chip devices based on surface acoustic waves." In: *Lab on a Chip* 11.7 (2011), pp. 1280–1285.
- [44] Xiaole Mao, Sz-Chin Steven Lin, Cheng Dong, and Tony Jun Huang. "Single-layer planar on-chip flow cytometer using microfluidic drifting based three-dimensional (3D) hydrodynamic focusing." In: *Lab on a Chip* 9.11 (2009), pp. 1583–1589.
- [45] Sung Hwan Cho, Chun H Chen, Frank S Tsai, Jessica M Godin, and Yu-Hwa Lo. "Human mammalian cell sorting using a highly integrated micro-fabricated fluorescence-activated cell sorter ( $\mu$ FACS)." In: *Lab on a Chip* 10.12 (2010), pp. 1567–1573.
- [46] Alexandr Jonáš and Pavel Zemanek. "Light at work: The use of optical forces for particle manipulation, sorting, and analysis." In: *Electrophoresis* 29.24 (2008), pp. 4813–4851.
- [47] Keir C Neuman and Attila Nagy. "Single-molecule force spectroscopy: optical tweezers, magnetic tweezers and atomic force microscopy." In: *Nature methods* 5.6 (2008), p. 491.
- [48] Mark M Wang, Eugene Tu, Daniel E Raymond, Joon Mo Yang, Haichuan Zhang, Norbert Hagen, Bob Dees, Elinore M Mercer, Anita H Forster, Ilona Kariv, et al. "Microfluidic sorting of mammalian cells by optical force switching." In: *Nature biotechnology* 23.1 (2005), pp. 83–87.

- [49] Nan Xia, Tom P Hunt, Brian T Mayers, Eben Alsberg, George M Whitesides, Robert M Westervelt, and Donald E Ingber. "Combined microfluidic-micromagnetic separation of living cells in continuous flow." In: *Biomedical microdevices* 8.4 (2006), pp. 299–308.
- [50] James J Lai, Kjell E Nelson, Michael A Nash, Allan S Hoffman, Paul Yager, and Patrick S Stayton. "Dynamic bioprocessing and microfluidic transport control with smart magnetic nanoparticles in laminar-flow devices." In: *Lab on a Chip* 9.14 (2009), pp. 1997–2002.
- [51] Kazunori Hoshino, Yu-Yen Huang, Nancy Lane, Michael Huebschman, Jonathan W Uhr, Eugene P Frenkel, and Xiaojing Zhang. "Microchip-based immuno-magnetic detection of circulating tumor cells." In: *Lab on a Chip* 11.20 (2011), pp. 3449–3457.
- [52] Leah M Johnson, Lu Gao, C Wyatt Shields IV, Margret Smith, Kirill Efimenko, Kevin Cushing, Jan Genzer, and Gabriel P López. "Elastomeric microparticles for acoustic mediated bioseparations." In: *Journal of nanobiotechnology* 11.1 (2013), p. 22.
- [53] Xiaoyuan Hu, Paul H Bessette, Jiangrong Qian, Carl D Meinhart, Patrick S Daugherty, and Hyongsok T Soh. "Marker-specific sorting of rare cells using dielectrophoresis." In: *Proceedings of the National Academy of Sciences of the United States of America* 102.44 (2005), pp. 15757–15761.
- [54] Filip Petersson, Andreas Nilsson, Cecilia Holm, Henrik Jönsson, and Thomas Laurell. "Separation of lipids from blood utilizing ultrasonic standing waves in microfluidic channels." In: *Analyst* 129.10 (2004), pp. 938–943.
- [55] Filip Petersson, Andreas Nilsson, Cecilia Holm, Henrik Jönsson, and Thomas Laurell. "Continuous separation of lipid particles from erythrocytes by means of laminar flow and acoustic standing wave forces." In: *Lab on a Chip* 5.1 (2005), pp. 20–22.
- [56] Ying Huang, Sunghae Joo, Melanie Duhon, Michael Heller, Bruce Wallace, and Xiao Xu. "Dielectrophoretic cell separation and gene expression profiling on microelectronic chip arrays." In: *Analytical chemistry* 74.14 (2002), pp. 3362–3371.
- [57] Eric B Cummings and Anup K Singh. "Dielectrophoresis in microchips containing arrays of insulating posts: theoretical and experimental results." In: *Analytical chemistry* 75.18 (2003), pp. 4724–4731.
- [58] Michael D Vahey and Joel Voldman. "An equilibrium method for continuous-flow cell sorting using dielectrophoresis." In: *Analytical chemistry* 80.9 (2008), pp. 3135–3143.
- [59] Mehmet Toner and Daniel Irimia. "Blood-on-a-chip." In: *Annu. Rev. Biomed. Eng.* 7 (2005), pp. 77–103.

- [60] D Melville, F Paul, and S Roath. "Direct magnetic separation of red cells from whole blood." In: *Nature* 255.5511 (1975), pp. 706–706.
- [61] Taotao Zhu, Rui Cheng, Sarah A Lee, Eashwar Rajaraman, Mark A Eiteman, Troy D Querec, Elizabeth R Unger, and Leidong Mao. "Continuous-flow ferrohydrodynamic sorting of particles and cells in microfluidic devices." In: *Microfluidics and nanofluidics* 13.4 (2012), pp. 645–654.
- [62] Elodie Sollier, Hervé Rostaing, Patrick Pouteau, Yves Fouillet, and Jean-Luc Achard. "Passive microfluidic devices for plasma extraction from whole human blood." In: *Sensors and Actuators B: Chemical* 141.2 (2009), pp. 617–624.
- [63] Dino Di Carlo. "Inertial microfluidics." In: *Lab on a Chip* 9.21 (2009), pp. 3038–3046.
- [64] Dino Di Carlo, Daniel Irimia, Ronald G Tompkins, and Mehmet Toner. "Continuous inertial focusing, ordering, and separation of particles in microchannels." In: *Proceedings of the National Academy of Sciences* 104.48 (2007), pp. 18892–18897.
- [65] Han Wei Hou, Majid Ebrahimi Warkiani, Bee Luan Khoo, Zi Rui Li, Ross A Soo, Daniel Shao-Weng Tan, Wan-Teck Lim, Jongyoon Han, Ali Asgar S Bhagat, and Chwee Teck Lim. "Isolation and retrieval of circulating tumor cells using centrifugal forces." In: *Scientific reports* 3 (2013), p. 1259.
- [66] G Segre. "Radial particle displacements in Poiseuille flow of suspensions." In: *Nature* 189 (1961), pp. 209–210.
- [67] Emre Ozkumur, Ajay M Shah, Jordan C Ciciliano, Benjamin L Emmink, David T Miyamoto, Elena Brachtel, Min Yu, Pin-i Chen, Bailey Morgan, Julie Trautwein, et al. "Inertial focusing for tumor antigen-dependent and-independent sorting of rare circulating tumor cells." In: *Science translational medicine* 5.179 (2013), 179ra47–179ra47.
- [68] Sungyoung Choi and Je-Kyun Park. "Continuous hydrophoretic separation and sizing of microparticles using slanted obstacles in a microchannel." In: *Lab on a Chip* 7.7 (2007), pp. 890–897.
- [69] Hisham Mohamed, Megan Murray, James N Turner, and Michele Caggana. "Isolation of tumor cells using size and deformation." In: *Journal of Chromatography A* 1216.47 (2009), pp. 8289–8295.
- [70] Hong Miao Ji, Victor Samper, Yu Chen, Chew Kiat Heng, Tit Meng Lim, and Levent Yobas. "Silicon-based microfilters for whole blood cell separation." In: *Biomedical microdevices* 10.2 (2008), pp. 251–257.
- [71] Zongbin Liu, Fei Huang, Jinghui Du, Weiliang Shu, Hongtao Feng, Xiaoping Xu, and Yan Chen. "Rapid isolation of cancer cells using microfluidic deterministic lateral displacement structure." In: *Biomicrofluidics* 7.1 (2013), p. 011801.



- [72] Jason P Beech, Stefan H Holm, Karl Adolfsson, and Jonas O Tegenfeldt. "Sorting cells by size, shape and deformability." In: *Lab on a Chip* 12.6 (2012), pp. 1048–1051.
- [73] Robert W Fox, Alan T McDonald, and Philip J Pritchard. *Introduction to fluid mechanics*. Vol. 7. John Wiley & Sons New York, 1985.
- [74] John David Anderson and J Wendt. *Computational fluid dynamics*. Vol. 206. Springer, 1995.
- [75] Richard AL Jones. *Soft condensed matter*. Vol. 6. Oxford University Press, 2002.
- [76] JP Mills, L Qie, M Dao, CT Lim, S Suresh, et al. "Nonlinear elastic and viscoelastic deformation of the human red blood cell with optical tweezers." In: *MCB-TECH SCIENCE PRESS*- 1 (2004), pp. 169–180.
- [77] Randall J LeVeque. *Finite difference methods for ordinary and partial differential equations: steady-state and time-dependent problems*. SIAM, 2007.
- [78] Susanne Brenner and Ridgway Scott. *The mathematical theory of finite element methods*. Vol. 15. Springer Science & Business Media, 2007.
- [79] R Eymard, Th Gallouët, and R Herbin. "Finite volume methods, in hand book of numerical analysis, Vol. VII, 713-1020." In: *Handb. Numer. Anal., VII, North-Holland, Amsterdam* (2000).
- [80] Ann S Almgren, John B Bell, and William G Szymczak. "A numerical method for the incompressible Navier-Stokes equations based on an approximate projection." In: *SIAM Journal on Scientific Computing* 17.2 (1996), pp. 358–369.
- [81] Martin R Maxey and James J Riley. "Equation of motion for a small rigid sphere in a nonuniform flow." In: *The Physics of Fluids* 26.4 (1983), pp. 883–889.
- [82] Enrico Fermi, J Pasta, and S Ulam. "Studies of nonlinear problems." In: *Los Alamos Report LA-1940* 978 (1955).
- [83] Berni J Alder and T E Wainwright. "Studies in molecular dynamics. I. General method." In: *The Journal of Chemical Physics* 31.2 (1959), pp. 459–466.
- [84] Don S Lemons and Anthony Gythiel. "Paul Langevin's 1908 paper "on the theory of Brownian motion"["Sur la théorie du mouvement brownien," CR Acad. Sci.(Paris) 146, 530–533 (1908)]." In: *American Journal of Physics* 65.11 (1997), pp. 1079–1081.
- [85] Eligiusz Wajnryb, Krzysztof A Mizerski, Pawel J Zuk, and Piotr Szymczak. "Generalization of the Rotne–Prager–Yamakawa mobility and shear disturbance tensors." In: *Journal of Fluid Mechanics* 731 (2013), R3.
- [86] Shiyi Chen and Gary D Doolen. "Lattice Boltzmann method for fluid flows." In: *Annual review of fluid mechanics* 30.1 (1998), pp. 329–364.

- [87] Xiaoyi He, Shiyi Chen, and Gary D Doolen. "A novel thermal model for the lattice Boltzmann method in incompressible limit." In: *Journal of Computational Physics* 146.1 (1998), pp. 282–300.
- [88] G Gompper, T Ihle, DM Kroll, and RG Winkler. "Multi-particle collision dynamics: a particle-based mesoscale simulation approach to the hydrodynamics of complex fluids." In: *Advanced computer simulation approaches for soft matter sciences III*. Springer, 2009, pp. 1–87.
- [89] PJ Hoogerbrugge and JMVA Koelman. "Simulating microscopic hydrodynamic phenomena with dissipative particle dynamics." In: *EPL (Europhysics Letters)* 19.3 (1992), p. 155.
- [90] Pep Espanol and Patrick Warren. "Statistical mechanics of dissipative particle dynamics." In: *EPL (Europhysics Letters)* 30.4 (1995), p. 191.
- [91] Colin Marsh. "Theoretical aspects of dissipative particle dynamics." In: (1998).
- [92] Kun Yan, Yu-Zong Chen, Jongyoon Han, Gui-Rong Liu, Jian-Sheng Wang, and Nicolas G Hadjiconstantinou. "Dissipative particle dynamics simulation of field-dependent DNA mobility in nanoslits." In: *Microfluidics and nanofluidics* 12.1-4 (2012), pp. 157–163.
- [93] Duc Duong-Hong, Jian-Sheng Wang, GR Liu, Yu Zong Chen, Jongyoon Han, and Nicolas G Hadjiconstantinou. "Dissipative particle dynamics simulations of electroosmotic flow in nano-fluidic devices." In: *Microfluidics and Nanofluidics* 4.3 (2008), pp. 219–225.
- [94] Pep Espanol and Mariano Revenga. "Smoothed dissipative particle dynamics." In: *Physical Review E* 67.2 (2003), p. 026705.
- [95] Joe J Monaghan. "Smoothed particle hydrodynamics." In: *Annual review of astronomy and astrophysics* 30.1 (1992), pp. 543–574.
- [96] Kathrin Müller, Dmitry A Fedosov, and Gerhard Gompper. "Smoothed dissipative particle dynamics with angular momentum conservation." In: *Journal of computational physics* 281 (2015), pp. 301–315.
- [97] Rohan Vernekar and Timm Krüger. "Breakdown of deterministic lateral displacement efficiency for non-dilute suspensions: a numerical study." In: *Medical engineering & physics* 37.9 (2015), pp. 845–854.
- [98] Aleksander S Popel and Paul C Johnson. "Microcirculation and hemorheology." In: *Annu. Rev. Fluid Mech.* 37 (2005), pp. 43–69.
- [99] Luca Lanotte, Johannes Mauer, Simon Mendez, Dmitry A Fedosov, Jean-Marc Fromental, Viviana Claveria, Franck Nicoud, Gerhard Gompper, and Manouk Abkarian. "Red cells' dynamic morphologies govern blood shear thinning under microcirculatory flow conditions." In: *Proceedings of the National Academy of Sciences* (2016), p. 201608074.

- [100] Toshihiro Omori, Yohsuke Imai, Takami Yamaguchi, and Takuji Ishikawa. "Re-orientation of a nonspherical capsule in creeping shear flow." In: *Physical review letters* 108.13 (2012), p. 138102.
- [101] R Skalak and PI Branemark. "Deformation of red blood cells in capillaries." In: *Science* 164.3880 (1969), pp. 717–719.
- [102] Manouk Abkarian, Magalie Faivre, Renita Horton, Kristian Smistrup, Catherine A Best-Popescu, and Howard A Stone. "Cellular-scale hydrodynamics." In: *Biomedical materials* 3.3 (2008), p. 034011.
- [103] Dmitry A Fedosov, Matti Peltomäki, and Gerhard Gompper. "Deformation and dynamics of red blood cells in flow through cylindrical microchannels." In: *Soft matter* 10.24 (2014), pp. 4258–4267.
- [104] Badr Kaoui, GH Ristow, Isabelle Cantat, Chaouqi Misbah, and Walter Zimmermann. "Lateral migration of a two-dimensional vesicle in unbounded Poiseuille flow." In: *Physical Review E* 77.2 (2008), p. 021903.
- [105] Dmitry A Fedosov, Bruce Caswell, Aleksander S Popel, and George Em Karniadakis. "Blood Flow and Cell-Free Layer in Microvessels." In: *Microcirculation* 17.8 (2010), pp. 615–628.
- [106] B Lorz, R Simson, J Nardi, and E Sackmann. "Weakly adhering vesicles in shear flow: Tanktreading and anomalous lift force." In: *EPL (Europhysics Letters)* 51.4 (2000), p. 468.
- [107] Piero Olla. "The role of tank-treading motions in the transverse migration of a spheroidal vesicle in a shear flow." In: *Journal of Physics A: Mathematical and General* 30.1 (1997), p. 317.
- [108] Sebastian Meßlinger, Benjamin Schmidt, Hiroshi Noguchi, and Gerhard Gompper. "Dynamical regimes and hydrodynamic lift of viscous vesicles under shear." In: *Physical Review E* 80.1 (2009), p. 011901.
- [109] Daniel A Reasor, Marmar Mehrabadi, David N Ku, and Cyrus K Aidun. "Determination of critical parameters in platelet margination." In: *Annals of biomedical engineering* 41.2 (2013), pp. 238–249.
- [110] Kathrin Müller, Dmitry A Fedosov, and Gerhard Gompper. "Understanding particle margination in blood flow—A step toward optimized drug delivery systems." In: *Medical engineering & physics* 38.1 (2016), pp. 2–10.
- [111] H Baumler, B Neu, E Donath, and H Kieseewetter. "Basic phenomena of red blood cell rouleaux formation." In: *Biorheology* 36.5-6 (1999), pp. 439–442.
- [112] Yoji Izumida, Akitoshi Seiyama, and Nobuji Maeda. "Erythrocyte aggregation: bridging by macromolecules and electrostatic repulsion by sialic acid." In: *Biochimica et Biophysica Acta (BBA)-Biomembranes* 1067.2 (1991), pp. 221–226.

- [113] Björn Neu and Herbert J Meiselman. "Depletion-mediated red blood cell aggregation in polymer solutions." In: *Biophysical journal* 83.5 (2002), pp. 2482–2490.
- [114] Shu Chien, S Usami, Robert J Dellenback, and MI Gregersen. "Shear-dependent interaction of plasma proteins with erythrocytes in blood rheology." In: *American Journal of Physiology–Legacy Content* 219.1 (1970), pp. 143–153.
- [115] J Liam McWhirter, Hiroshi Noguchi, and Gerhard Gompper. "Flow-induced clustering and alignment of vesicles and red blood cells in microcapillaries." In: *Proceedings of the National Academy of Sciences* 106.15 (2009), pp. 6039–6043.
- [116] Robert D Groot and Patrick B Warren. "Dissipative particle dynamics: Bridging the gap between atomistic and mesoscopic simulation." In: *The Journal of chemical physics* 107.11 (1997), pp. 4423–4435.
- [117] Ingo O Götze, Hiroshi Noguchi, and Gerhard Gompper. "Relevance of angular momentum conservation in mesoscale hydrodynamics simulations." In: *Physical Review E* 76.4 (2007), p. 046705.
- [118] G. Gompper and D. M. Kroll. "Network models of fluid, hexatic and polymerized membranes." In: *J. Phys.: Condens. Matter* 9 (1997), pp. 8795–8834.
- [119] D. E. Discher, D. H. Boal, and S. K. Boey. "Simulations of the erythrocyte cytoskeleton at large deformation. II. Micropipette aspiration." In: *Biophys. J.* 75 (1998), pp. 1584–1597.
- [120] H. Noguchi and G. Gompper. "Shape transitions of fluid vesicles and red blood cells in capillary flows." In: *Proc. Natl. Acad. Sci. USA* 102 (2005), pp. 14159–14164.
- [121] D. A. Fedosov, B. Caswell, and G. E. Karniadakis. "A multiscale red blood cell model with accurate mechanics, rheology, and dynamics." In: *Biophys. J.* 98 (2010), pp. 2215–2225.
- [122] D. A. Fedosov, B. Caswell, and G. E. Karniadakis. "Systematic coarse-graining of spectrin-level red blood cell models." In: *Comput. Meth. Appl. Mech. Eng.* 199 (2010), pp. 1937–1948.
- [123] W. Helfrich. "Elastic properties of lipid bilayers: theory and possible experiments." In: *Z. Naturforschung C* 28 (1973), pp. 693–703.
- [124] Jason P Beech and Jonas O Tegenfeldt. "Tuneable separation in elastomeric microfluidics devices." In: *Lab on a Chip* 8.5 (2008), pp. 657–659.
- [125] Jason P Beech, Peter Jönsson, and Jonas O Tegenfeldt. "Tipping the balance of deterministic lateral displacement devices using dielectrophoresis." In: *Lab on a Chip* 9.18 (2009), pp. 2698–2706.
- [126] John Alan Davis. "Microfluidic separation of blood components through deterministic lateral displacement." PhD thesis. Princeton University, 2008.

- [127] Daniel P. Huttenlocher, Gregory A. Klanderman, and William J Rucklidge. "Comparing images using the Hausdorff distance." In: *IEEE Transactions on pattern analysis and machine intelligence* 15.9 (1993), pp. 850–863.
- [128] B Kaoui, N Tahiri, T Biben, H Ez-Zahraouy, A Benyoussef, G Biros, and C Misbah. "Complexity of vesicle microcirculation." In: *Physical Review E* 84.4 (2011), p. 041906.
- [129] Jonathan B Freund. "Leukocyte margination in a model microvessel." In: *Physics of Fluids* 19.2 (2007), p. 023301.
- [130] T Kulrattanakarak, RGM Van der Sman, YS Lubbersen, CGPH Schroën, HTM Pham, PM Sarro, and RM Boom. "Mixed motion in deterministic ratchets due to anisotropic permeability." In: *Journal of colloid and interface science* 354.1 (2011), pp. 7–14.
- [131] T Kulrattanakarak, RGM Van Der Sman, CGPH Schroën, and RM Boom. "Analysis of mixed motion in deterministic ratchets via experiment and particle simulation." In: *Microfluidics and Nanofluidics* 10.4 (2011), pp. 843–853.
- [132] Shashi Ranjan, Kerwin Kwek Zeming, Roland Jureen, Dale Fisher, and Yong Zhang. "DLD pillar shape design for efficient separation of spherical and non-spherical bioparticles." In: *Lab on a Chip* 14.21 (2014), pp. 4250–4262.
- [133] J. A. Davis. "Microfluidic separation of blood components through deterministic lateral displacement." PhD thesis. Princeton University, USA, 2008.
- [134] Zunmin Zhang, Ewan Henry, Gerhard Gompper, and Dmitry A Fedosov. "Behavior of rigid and deformable particles in deterministic lateral displacement devices with different post shapes." In: *The Journal of chemical physics* 143.24 (2015), p. 243145.
- [135] Kevin Louthierback, Jason Puchalla, Robert H Austin, and James C Sturm. "Deterministic microfluidic ratchet." In: *Physical review letters* 102.4 (2009), p. 045301.
- [136] Kerwin Kwek Zeming, Shashi Ranjan, and Yong Zhang. "Rotational separation of non-spherical bioparticles using I-shaped pillar arrays in a microfluidic device." In: *Nature communications* 4 (2013), p. 1625.
- [137] Jianhui Wei, Hui Song, Zaiyi Shen, Ying He, Xianzhi Xu, Yong Zhang, and Bing Nan Li. "Numerical Study of Pillar Shapes in Deterministic Lateral Displacement Microfluidic Arrays for Spherical Particle Separation." In: *IEEE transactions on nanobioscience* 14.6 (2015), pp. 660–667.
- [138] Isabelle Cantat and Chaouqi Misbah. "Lift force and dynamical unbinding of adhering vesicles under shear flow." In: *Physical review letters* 83.4 (1999), p. 880.
- [139] Manouk Abkarian, Colette Lartigue, and Annie Viallat. "Tank treading and unbinding of deformable vesicles in shear flow: determination of the lift force." In: *Physical review letters* 88.6 (2002), p. 068103.

- [140] Ewan Henry, Stefan H Holm, Zunmin Zhang, Jason P Beech, Jonas O Tegenfeldt, Dmitry A Fedosov, and Gerhard Gompper. "Sorting cells by their dynamical properties." In: *Scientific Reports* 6 (2016).
- [141] M. Abkarian, M. Faivre, and A. Viallat. "Swinging of red blood cells under shear flow." In: *Phys. Rev. Lett.* 98 (2007), p. 188302.
- [142] J. Dupire, M. Socol, and A. Viallat. "Full dynamics of a red blood cell in shear flow." In: *Proc. Natl. Acad. Sci. USA* 109 (2012), pp. 20808–20813.
- [143] V. Vitkova, M.-A. Mader, B. Polack, C. Misbah, and T. Podgorski. "Micro-macro link in rheology of erythrocyte and vesicle suspensions." In: *Biophys. J.* 95 (2008), pp. L33–L35.
- [144] A. Z. K. Yazdani and P. Bagchi. "Phase diagram and breathing dynamics of a single red blood cell and a biconcave capsule in dilute shear flow." In: *Phys. Rev. E* 84 (2011), p. 026314.
- [145] R. Tran-Son-Tay, S. P. Sutera, and P. R. Rao. "Determination of red blood cell membrane viscosity from rheoscopic observations of tank-treading motion." In: *Biophys. J.* 46 (1984), pp. 65–72.
- [146] T. M. Fischer. "Shape memory of human red blood cells." In: *Biophys. J.* 86 (2004), pp. 3304–3313.
- [147] I. Cantat and C. Misbah. "Lift force and dynamical unbinding of adhering vesicles under shear flow." In: *Phys. Rev. Lett.* 83 (1999), pp. 880–883.
- [148] Timm Krüger, David Holmes, and Peter V Coveney. "Deformability-based red blood cell separation in deterministic lateral displacement devices—a simulation study." In: *Biomicrofluidics* 8.5 (2014), p. 054114.
- [149] Z. Zhang, E. Henry, G. Gompper, and D. A. Fedosov. "Behavior of rigid and deformable particles in deterministic lateral displacement devices with different post shapes." In: *J. Chem. Phys.* 143 (2015), p. 243145.
- [150] John Philip Mills. "Deformability of Plasmodium falciparum parasitized red blood cells." PhD thesis. Massachusetts Institute of Technology, 2007.
- [151] GB Nash, E O'Brien, EC Gordon-Smith, and JA Dormandy. "Abnormalities in the mechanical properties of red blood cells caused by Plasmodium falciparum." In: *Blood* 74.2 (1989), pp. 855–861.
- [152] Kerwin Kwek Zeming, Thoriq Salafi, Chia-Hung Chen, and Yong Zhang. "Asymmetrical deterministic lateral displacement gaps for dual functions of enhanced separation and throughput of red blood cells." In: *Scientific reports* 6 (2016).
- [153] Ji-chul Hyun, Jaeyub Hyun, Semyung Wang, and Sung Yang. "Improved pillar shape for deterministic lateral displacement separation method to maintain separation efficiency over a long period of time." In: *Separation and Purification Technology* 172 (2017), pp. 258–267.

- [154] Yu Chen, Ezra S Abrams, T Christian Boles, Jonas N Pedersen, Henrik Flyvbjerg, Robert H Austin, and James C Sturm. "Concentrating genomic length DNA in a microfabricated array." In: *Physical review letters* 114.19 (2015), p. 198303.
- [155] Jesse L Rodriguez, Ankur B Dalia, and Jeffrey N Weiser. "Increased chain length promotes pneumococcal adherence and colonization." In: *Infection and immunity* 80.10 (2012), pp. 3454–3459.
- [156] Stefan H Holm, Jason P Beech, and Jonas O Tegenfeldt. "Combined density and size-based sorting in deterministic lateral displacement devices." In: *Presented at the 17th International Conference on Miniaturized Systems for Chemistry and Life Sciences, 17th International Conference on Miniaturized Systems for Chemistry and Life Sciences*. 2013.
- [157] Sylvie Hénon, Guillaume Lenormand, Alain Richert, and François Gallet. "A new determination of the shear modulus of the human erythrocyte membrane using optical tweezers." In: *Biophysical journal* 76.2 (1999), pp. 1145–1151.
- [158] R Waugh and EA Evans. "Thermoelasticity of red blood cell membrane." In: *Biophysical journal* 26.1 (1979), pp. 115–131.
- [159] Alexander Mietke, Oliver Otto, Salvatore Girardo, Philipp Rosendahl, Anna Taubenberger, Stefan Golfier, Elke Ulbricht, Sebastian Aland, Jochen Guck, and Elisabeth Fischer-Friedrich. "Extracting cell stiffness from real-time deformability cytometry: theory and experiment." In: *Biophysical journal* 109.10 (2015), pp. 2023–2036.
- [160] H Strey, M Peterson, and E Sackmann. "Measurement of erythrocyte membrane elasticity by flicker eigenmode decomposition." In: *Biophysical journal* 69.2 (1995), pp. 478–488.
- [161] B. R. Long, M. Heller, J. P. Beech, H. Linke, H. Bruus, and J. O. Tegenfeldt. "Multidirectional sorting modes in deterministic lateral displacement devices." In: *Phys. Rev. E* 78 (2008), p. 046304.
- [162] J. Frechette and G. Drazer. "Directional locking and deterministic separation in periodic arrays." In: *J. Fluid Mech.* 627 (2009), pp. 379–401.
- [163] C. A. Schneider, W. S. Rasband, and K. W. Eliceiri. "Real-time deformability cytometry: on-the-fly cell mechanical phenotyping." In: *Nat. Methods* 9 (2012), pp. 671–675.





## ERKLÄRUNG

---

Ich versichere, dass ich die von mir vorgelegte Dissertation selbstständig angefertigt, die benutzten Quellen und Hilfsmittel vollständig angegeben und die Stellen der Arbeit – einschließlich Tabellen, Karten und Abbildungen –, die anderen Werken im Wortlaut oder dem Sinn nach entnommen sind, in jedem Einzelfall als Entlehnung kenntlich gemacht habe; dass diese Dissertation noch keiner anderen Fakultät oder Universität zur Prüfung vorgelegen hat; dass sie abgesehen von unten angegebenen Teilpublikationen noch nicht veröffentlicht worden ist, sowie, dass ich eine solche Veröffentlichung vor Abschluss des Promotionsverfahrens nicht vornehmen werde. Die Bestimmungen der Promotionsordnung sind mir bekannt. Die von mir vorgelegte Dissertation ist von Prof. Dr. Gerhard Gompper betreut worden.

*Jülich , 6<sup>th</sup> March 2017*

---

Ewan Henry



## CURRICULUM VITAE

---

### PERSÖNLICHE ANGABEN

<i>Name</i>	Henry
<i>Vorname</i>	Ewan
<i>Geburtsdatum</i>	31.07.1991
<i>Geburstort</i>	Middlesex, England
<i>Staatsangehörigkeit</i>	Britisch

### AUSBILDUNG

**Promotionsstudent****2016-2017***Universität zu Köln***Doktorand im Fach Physik****2013-2017***Forschungszentrum Jülich GmbH***MPhys und BSc im Physik****2009-2013***University of Leeds, England*1<sup>st</sup> Hon.**A-Levels,****2008-2009***Richmond upon Thames College, England, Twickenham*

Mathe (A), Physik (B), Musik (B)

**AS-Levels,****2007-2008***British School Muscat, Oman*

Erdkunde (A), Rechnen(B)